Atomistic and Micromagnetic Study of Ultra-low-power Spintronics devices

Junlin Wang

Doctor of Philosophy

University of York

Electronics Engineering

September 2019

Abstract

In this thesis, I used atomistic and micromagnetic model to study the dynamics behaviour of the domain wall and skyrmion in confined nanostructures driven by applied magnetic field, spin polarized current and voltage control magnetic anisotropy gradient. I also studied the thermal behaviour of the magnetic skyrmion in magnetic ultra-thin film. I study the domain structure and the magnetic switching in the Permalloy ($Fe_{20}Ni_{80}$) nanoscale magnetic junctions with different thicknesses by using micromagnetic simulations. My work shows that the nanoscale magnetic junction has the potential to be used as a building block for future spin-based data storage or logic computing technologies. The current-driven skyrmion motion in a narrow ferromagnetic nano-track with voltage-controlled magnetic anisotropy (VCMA) is studied numerically. The skyrmionium dynamics in a nano-track with voltage-controlled perpendicular magnetic anisotropy (VCMA) also has been reported. The results provide guidelines for practical realization of the skyrmion-based information channel, diode, and skyrmion-based electronic devices such as racetrack memory. The thermal-induced phase transition to a skyrmion state in IrCoPt has been demonstrated by the atomistic simulations parametrised from ab-initio calculations which include long-range exchange interactions. The simulation results give a clear vision of the thermal-induced behaviour in a chiral magnetic thin film.

Contents:

List of Figures:

Acknowledgements:

During the four year study at the University of York, I think I was supported and helped by many people in many ways. At the beginning of this Ph.D. thesis, I want to thank all of them.

First, I would like to sincerely thank my supervisors Prof. Yongbing Xu and Prof. Roy Chantrell, for giving me the chance to join their research groups at York. When I was an undergraduate student in Macau, Prof. Xu gave me the chance to study in his group in the Department of electronics and help me start the journey in the world of magnetism and spintronics. Then during the study in York, it is so lucky that I can study the atomistic simulation under the supervising of Prof. Chantrell and join his group in the Department of Physics. I have learnt a lot from them and the kindly people in their research groups.

I would also like the sincerely thank my co-supervisors Dr. Xichao Zhang, Dr. Jing Wu, Prof. Yan Zhou, Miss Jing Xia. I was helped and supported by Prof. Zhou and Dr. Zhang when I started to learn the micromagnetic simulation. Prof. Zhou, Dr. Zhang and Miss Jing Xia always gave me helpful advice and guidance. Dr. Wu always gives me valuable knowledge about spin dynamics.

I want to thanks the colleagues in Prof. Xu and Dr. Jing's group. I want to thank Dr. Xianyang Lu, Dr. Yichuan Wang, Dr. Yu Yan, Mr. Hua Ling, Mr. Guanqi Li, Mr. Kunpeng Zhang, Mr. Xiangyu Zheng, Mr. Wenjia Li, for their cooperation in the experiment works.

I want to thanks the colleague in Prof. Chantrell's group. I want to thank Dr. Richard FL Evans, for his help on atomistic simulation. I would like to thank Dr. Sergiu Ruta, Miss. Mara Strungaru, Dr. Andrea Meo for their useful discussions and kindly help about the atomistic simulation of magnetic skyrmion.

Most importantly, I would like to give my endless gratitude to my beloved family, for their selfless dedication and encouragement, they are the reason that keeps me motivated throughout all the difficulties.

Declaration of Authorship:

I declare that this thesis titled, “Atomistic and Micromagnetic study of ultra-low power spintronics device”, and the work presented in it are my own.

I confirm that: This work was done wholly or mainly while in candidature for a research degree at this university and has not been submitted previously for a degree at this or any other university.

Where I have quoted from the work of others, the source is always given. Except for such quotations, this thesis is entirely my own work. I have acknowledged all main sources of help.

Where the thesis is based on work done by myself jointly with others, I have made clear exactly what was done by others and what I have contributed myself.

Much of the data has been publicly presented by the author and the results in Chapter 4 are published in the following article: **Junlin Wang**, et al. "Magnetic domain wall engineering in a nanoscale permalloy junction." Applied Physics Letters 111, no. 7 (2017): 072401. The results in Chapter 5 are published in the following article: **Junlin Wang**, et al. "Controllable transport of a skyrmion in a ferromagnetic narrow channel with voltage-controlled magnetic anisotropy." Journal of Physics D: Applied Physics 51, no. 20 (2018): 205002. The simulation parameters from ab-initio calculation in Chapter 7 is calculated by Prof. László Szunyogh.

Publication List:

1. **Junlin Wang**, Xichao Zhang, Xianyang Lu, Jason Zhang, Yu Yan, Hua Ling, Jing Wu, Yan Zhou, and Yongbing Xu. "Magnetic domain wall engineering in a nanoscale permalloy junction." Applied Physics Letters 111, no. 7 (2017): 072401.

2. **Junlin Wang**, Jing Xia, Xichao Zhang, G. P. Zhao, Lei Ye, Jing Wu, Yongbing Xu, Weisheng Zhao, Zhigang Zou, and Yan Zhou. "Controllable transport of a skyrmion in a ferromagnetic narrow channel with voltage-controlled magnetic anisotropy." Journal of Physics D: Applied Physics 51, no. 20 (2018): 205002.

3. Yu Yan, Cong Lu, Hongqing Tu, Xianyang Lu, Wenqing Liu, **Junlin Wang**, Lei Ye, Iain Will, Balati Kuerbanjiang, Vlado K. Lazarov, Jing Wu, Johnny Wong, Biao You, Jun Du, Rong Zhang, and Yongbing Xu. "Element specific spin and orbital moments of nanoscale CoFeB amorphous thin films on GaAs (100)." AIP Advances 6, no. 9 (2016): 095011.

4. Bolin Lai, Xiaoqian Zhang, Xianyang Lu, Long Yang, **Junlin Wang**, Yequan Chen, Yafei Zhao et al. "Magnetic anisotropy of half-metallic Co2FeAl ultra-thin films epitaxially grown on GaAs (001)." AIP Advances 9, no. 6 (2019): 065002.

5. Xianyang Lu, Lewis J. Atkinson, Balati Kuerbanjiang, Bo Liu, Guanqi Li, Yichuan Wang, **Junlin Wang** et al. "Enhancement of intrinsic magnetic damping in defect-free epitaxial Fe3O4 thin films." Applied Physics Letters 114, no. 19 (2019)

Chapter.1 Introduction

1. 1 Background

Magnetism is one of the most important and oldest research topics. The first magnetic material known to men is magnetite (Fe_3O_4) which starts the story of magnetism [1]. The magnetic properties of the material arise from charge and angular momentum-bearing particles inside the material. The magnetic field will be produced by the magnetic moment which is generated by the charged particle with angular momentum. The magnetic field will interact with other magnetic moments. The phenomenon is called the dipole-dipole interaction which is a long-range interaction.

The magnetic material has wide usage in our daily life, such as permanent magnets and bio-magnetism. An essential aspect of magnetic materials is for building the information storage device. The information storage devices are widely used in our lives, such as the computer, smartphone and other electronic devices. The driving force for the development of magnetism based information storage devices is the requirement for higher memory density and lower power consumption [2]. The first application of magnetism based storage medium, termed magnetic wire recording was invented by Oberlin Smith in 1888. After that, magnetic recording tape was invented by Fritz Pfleumer in 1928. The magnetic recording tape was applied as audio information storage. More recently, Abert Fert and Peter Grunberg were awarded the 2007 Nobel Prize because of their discovery of the giant magnetoresistance (GMR) effect in 1988 [3, 4]. GMR system is a tri-layer structure where two ferromagnetic layers are separated by a metallic conductor. The relative orientation of the ferromagnetic layer magnetisation can be changed by an applied magnetic field. This magnetisation orientation change will cause changes in conductance of the structure. When the two ferromagnetic layers have the same magnetisation direction, electrons of a single spin type can move easily through the system. While, if the magnetisation of the two

ferromagnetic layers is opposed, electrons of both spin types are strongly scattered, causing higher electrical resistance. These experiments provide a new outlook on the modern spintronics memory devices. The best-known application of GMR is the Read-head in hard-disk drives which enhance the performance of the hard-disk drives. Moreover, the discovery of GMR created a new research field called Spintronics (Spin Electronics).

The spintronics (Spin electronics) involves many studies which play an important role in the modern electronics device industry [5, 6]. Research in the spintronic area are in diverse areas of solid-state-physics, such as magnetism, semiconductor physics, superconductivity, optics and mesoscopic physics [7, 8]. Spintronics main studies are about the active control and manipulation of spin degrees of freedom in the solid-state system. One of the goals of spintronics is to understand and use the interaction between electron spins and magnetic materials to fabricate useful devices. The performance of the spintronics devices usually depends on the solid-state environments of the materials. The advantage of the spintronics device is low power, high speed, infinitely reversible and large capacity. Spintronics devices has been seen as the technology of the next generation.

1. 2 Spintronics devices

After the GMR effect was discovered by Abert Fert and Peter Grunberg, there are a lot of novel spintronics devices which have been proposed. One of the most promising candidates, spintronics devices is the magnetoresistive random access memory (MRAM). The MRAM based on tunneling magnetic resistance (TMR) effect. TMR has the potential to replace all the existing memory devices in a computer or other hard disk drives as it could provide a high read/write operation speed and is also non-volatile [9-12]. Compared with the MRAM device, the Spin transfer torque magnetoresistive random access memory (STT-MRAM) device has a simpler structure and is controlled

by spin polarized currents. The MRAM device needs an applied field to control the magnetisation in the device, where the STT-RAM only needs to inject a current which means the STT-RAM has a much faster speed. Spin transfer torque was proposed by J. Slonczewski and L. Berger independently in 1996 [13, 14]. Moreover, Berger's research found that the domain wall motion can be induced by the spin polarized current. In further work, Berger's group researched the domain wall motion in the thin film under large current pulse. The Spin transfer drives magnetic precession and changes the spin configuration in the magnetic device. This has been reported in many articles from 1998 to 2000 [15, 16]. Different from the traditional MRAM, the STT-RAM display a more convenient way to switch the data state. The information in the STT-RAM can be modified by the spin polarized current which is more convenient than using the applied magnetic field.

Magnetic domains are a basic magnetic structure of the magnetic materials. The small regions in the ferromagnetic material are called domains. The different domain has a different direction of magnetisation. The magnetic domain wall plays an important role in the modern spintronics device. The information in the magnetism device has been represented by the direction of magnetisation. One such device called a magnetic logic gate, which has been realised by the domain wall technology. The device can display the function of the digital logic gate without transistors in it [17-19]. The domain wall based logic gate is a sub-micrometric planar which is made from a soft magnetic material such as Permalloy ($Ni_{80}Fe_{20}$) which has been shown to form an excellent conduit for domain walls. Moreover, the high shape anisotropy can make the magnetisation in the device can align with the long axis of the wire.

There have been many articles reporting that the domain wall motion can be induced by a spin polarized current [20, 21]. The recent development in the application of spin polarized current device gives a promise of a non-volatile memory device with the high capacity and reliability of conventional solid-state memory, but at the low cost of conventional magnetic disk drive storage. The racetrack memory has been proposed in 2008 and gives a new vision of the future memory industry [22]. Different from the

traditional hard disk drives which display storage in a 2D arrays of transistors and magnetic bits, the racetrack memory is a genuine 3D device. Domain walls are used to store information in the tall columns fabricated from magnetic material. Magnetic domain walls are formed at the boundaries between magnetic domains magnetized in opposite directions (up or down) along a racetrack. The spin-polarized current drives the domain walls motion in the racetrack which can be detected by the reading head.

The magnetic skyrmion is nanometer-scale magnetic domain wall structure which exhibits quasiparticle-like property [23]. The name skyrmion derives from the British field theorist Tony Skyrme, who considered topologically protected defects in continuous nonlinear field models as having properties of single particles. Skyrmions are localized in space and have a non-singular internal structure and finite energy, exhibit mutual attractive or repulsive interactions, and can condense into ordered phases (skyrmion lattices) [23, 24]. Skyrmions are characterized by a quantized topological charge, or topological skyrmion number, which is related to the topological properties of the field configuration. Similar to the magnetic domain, skyrmion has potential usage in building skyrmion based racetrack memory, skyrmion logical device. Comparing with the magnetic domain based devices, skyrmion has a smaller size, faster speed and lower power [25-27].

1. 3 Aims of this PhD Work

For the development of hardware devices, this work is to provide the theoretical understanding of the spintronics devices, such as the MRAM, STT-MRAM, domain wall, and skyrmion based logical device. One method is to use the micromagnetic simulation method to do the simulations of these devices. By varying the parameters or shape of the devices, I can simulate the behaviour of the device and improve device performance and find the new applications of them. On the other hand, I use atomistic simulation to study the skyrmion dynamics in the perpendicular magnetic anisotropy materials. The thermal effect is included in the model, which can demonstrate the skyrmion behaviour under thermal effect.

1. 4 Thesis Overview

Fundamental physics research is highly demanded by the development of future spintronics devices. In this thesis, I present the studies about domain wall/skyrmion dynamics in nanoscale devices and thin film. Atomistic simulation and micromagnetic simulation has been used to study the domain wall/skyrmion behaviour in this thesis. The results in all of the chapters can provide useful guidelines for the designing and fabrication of the novel spintronics device.

In chapter. 1, I introduce the background of spintronics and the development of spintronics devices. A brief review for the STT-MRAM, domain wall based devices and skyrmion based device was given in this chapter. In chapter. 2, the theoretical background of magnetism is given. I discuss the exchange interaction in Ferromagnetic material, magnetic anisotropy and magnetostatic energy. I introduce the magnetic domain wall and skyrmion, which can be used to build novel information storage devices. In chapter. 3, the micromagnetic model and atomistic model are introduced. In this chapter, the energy terms in the Landau-Lifshitz equation has been discussed. In chapter. 4, I propose the domain wall engineering in a submicron permalloy junction. The domain structure in the cross-part of the device can display different states which can be used to build single layer storage device. In addition, I study the thickness-dependent switching field of the device. In chapter. 5, I study the skyrmion dynamics in a nano-track with voltage-controlled magnetic anisotropy (VCMA). Magnetic skyrmions are nanoscale particle-like topological configurations, which have been found in certain magnetic bulk materials, films and nanowire. The skyrmion is stabilized by delicate competitions among the ferromagnetic exchange coupling, perpendicular magnetic anisotropy (PMA) and Dzyaloshinskii–Moriya interaction (DMI) in magnetic system. Due to the different profile of the VCMA gate, the nano-track can display different properties. In the first part, I demonstrate the skyrmion based VCMA diode. Moreover, in the second part, I designed a skyrmion based information

channel. My results provide guidelines for practical realisation of the skyrmion-based information channel, diode, and skyrmion-based electronic devices such as racetrack memory. In chapter. 6, I study the skyrmionium dynamics in a nano-track with VCMA gate and anisotropy gradient induce skyrmionium motion in nano-track. Skyrmionium is a topological structure which can be seen as a combination of two skyrmion with a different quantum number. The skyrmionium is free from the skyrmion Hall effect and can be driven by current. In this chapter, I first use current to drive skyrmionium motion in a nanowire with VCMA gate. In the second part, I study the skyrmionium driven by an anisotropy gradient in nanowire which can avoids joule heating. The results provide guidelines for novel skyrmionium based devices. In chapter. 7, the skyrmion behaviour under high thermal effect in IrCoPt thin film has been studied. In this chapter, I use the atomistic simulation to demonstrate the thermal-induced phase transition in the system. The different phase in the system can be controlled by the different temperature effects. The result in this chapter can provide information for designing the skyrmion based devices which can work in high thermal environment. In chapter. 8, I give a summary of my PhD thesis and proposed future research directions. The future work is based on the result in this thesis and focuses on the novel spintronics devices.

Chapter.2 Magnetism

2. 1 Magnetisation

The magnetic moment, one of the most important quantities in magnetism. In the classical electromagnetism, the magnetic moment in a current loop can be explained as:

$$\mu = I \int_A \, dA, \tag{2.1}$$

Where μ is the magnetic moment, I is the electric current in the closed-loop, and the dA is the surface element of the closed-loop with a direction as the loop plane. The direction of the orbital magnetic moment is dependent on the direction of the current. There is an additional contribution to the moment from the intrinsic spin of the electron:

$$\mu = \gamma S, \tag{2.2}$$

Where the γ is the gyromagnetic ratio and S is the spin angular momentum of the electron. The total magnetic moment is the sum of spin and orbital contributions. In many cases, the orbital moment is quenched and the moment arises predominantly from the electron spin. In Micromagnetic study, the magnetisation M has been considered as the volume density of the magnetic moment which M can be explained as:

$$M = \frac{\sum \mu_i}{V}, \tag{2,3}$$

The magnetisation M is determined by the sum magnetic moment of the atoms in the defined volume. In micromagnetics, the magnetisation is assumed to change

continuously in the space. The saturation magnetisation M_S is a constant which is equal to $|M|$, the magnitude of the magnetisation.

2. 2 Weiss Mean Field Theory

The ferromagnetism is a specific material which has a basic mechanism leading to long-range magnetic order. The permanent magnets display ferromagnetic behaviour. The Weiss mean field theory which is a hypothesis on ferromagnetic material was the first proposed explanation of ferromagnetism.

The main characteristic of ferromagnetic material is a decrease of the magnetisation with temperature. The first model to explain this was the Weiss mean-field model. In the Weiss mean field theory, the magnetic moment μ in the magnetic material interact with each other. Every magnetic moment will try to align the other moment to its own direction. The magnetic domains in the system are consistently reorienting which can be affected by an external magnetic field. Each spin vector in the system is assumed to respond to an external field.

The M_S is the spontaneous magnetisation within the domain which is equal to the saturation magnetisation at 0K. The spontaneous magnetisation decreasing as the temperature increasing and equal to zero at Curie point. With the temperatures well below the Curie temperature, the M_S is almost to M_0 (M_0 is the magnetisation when material is incompletely saturated which means each of magnetic moment in it are aligned parallel) consequently [28]

$$H_m = \alpha M_s \tag{2.4}$$

Where α is the mean field constant, H_m is the mean (molecular field). The effective magnetic field of a magnetic domain can be explained as:

$$H_{eff} = H_{external} + H_m \tag{2.5}$$

The theoretically calculated value of the molecular field in iron can reach 10^3 T. The value is much larger than any manufactured field. The magnetic moments in the ferromagnetic solid within domains are oriented by the Weiss field but the magnetisation decreases with increasing temperature and disappears at the Curie temperature. Above the Curie temperature the material becomes paramagnetic. From the mean-field theory, the susceptibility in the paramagnetic state (magnerucally disordered) is.

$$\chi = \frac{M}{H} = \frac{C}{T-\theta} \tag{2.6}$$

Where C is the Curie constant and θ is the Curie temperature.

2. 3 Energy in the magnetic material

The magnetic system can be studied from the energetic point of view. In this section, I will discuss the four important energy contributions in magnetic systems: exchange energies, magnetostatic energy, anisotropy energy and Zeeman energy. These energy are also included in the atomistic spin dynamics model and micromagnetic model.

2. 3. 1 Exchange Interaction

In the Weiss mean field theory, the spontaneous magnetisation and interaction between magnetic moments in ferromagnetic materials has been explained. However, the Weiss theory gives no insight into the origin of the mean field.

However, there is a new theory which can describe the magnetisation of a ferromagnetic material proposed by Heisenberg. In his theory, the spontaneous magnetisation was explained as the result of the interaction between magnetic moments

in the ferromagnetic structure. The exchange force is a direct consequence of the Pauli exclusion principle. This states that two electrons can have the same energy only if they have opposite spins. Consequently, I might expect that as atoms are forced closer together the most stable configuration will be with the spins on neighbouring atoms antiparallel, i.e. non-ferromagnetic order should result. However, the exchange force arises in a very subtle way. Because of the indistinguishability of electrons I have to take into account the possibility that two electrons on neighbouring atoms simply exchange places. It is this which leads to the exchange energy between two neighbouring atoms. The exchange interaction of the spin angular moment S_i and S_j of two particles can be explained as:

$$E_{exc} = -2\ J_{ex}\ S_i \cdot S_j \tag{2.7}$$

In equation 2.7, the J_{ex} is the exchange integral. The sign of J_{ex} can help us to classify the system state. When the $J_{ex} > 0$, the system has the minimised exchange energy when two adjacent spins are parallel and displays ferromagnetic behaviour. When the $J_{ex} < 0$, the system has the minimised exchange energy when two adjacent spins are antiparallel and displays antiferromagnetic behaviour. Antiferromagnetic materials show no net magnetic moment. The exchange interactions of two spin in antiferromagnetic material and ferromagnetic material are illustrated in Figure 2. 1.

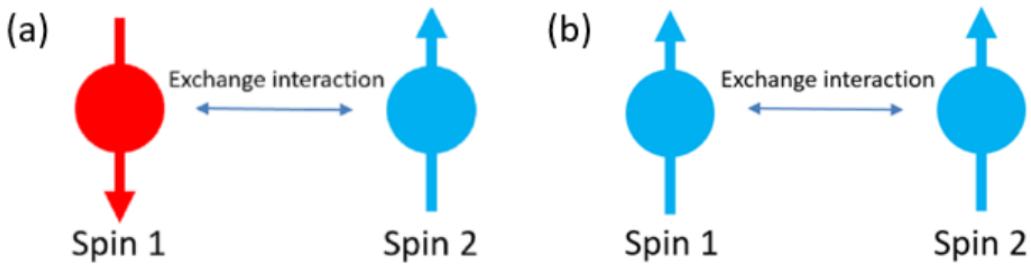

Figure 2.1 The exchange interaction between two spins. (a) Exchange interaction in an antiferromagnetic material. (b) Exchange interaction in a ferromagnetic material.

The Bethe-Slater curve, which shows the variation of exchange integral versus the ratio between the radio of the atom *a* and the radius of its 3d shell *r* is given in Figure 2.2.

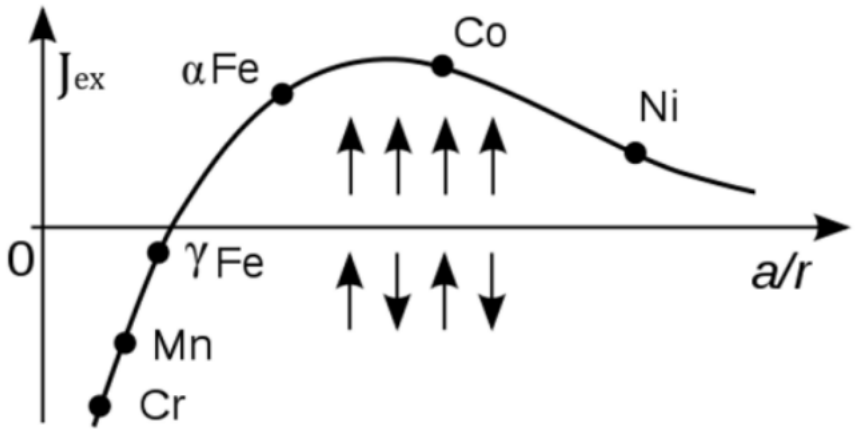

Figure 2.2 The Bethe-Slater curve, the arrow representative the spin direction. [29]

The Weiss mean field theory describes the ferromagnetic state in magnetic material in terms of a strong molecular field. But Heisenberg's theory is better to describe the physical process via the exchange interaction which induces the spins in the material to align parallel with each other. The total exchange interaction for a material with dominant nearest neighbour interaction is given as:

$$E_{exc} = -2\sum_{i,j} J_{ex} S_i \cdot S_j \tag{2.8}$$

2. 3. 2 Magnetic anisotropy

The directional dependence of a material's magnetic properties is called magnetic anisotropy. The easy axis is the preferred direction for the magnetisation. For a material

with uniaxial anisotropy the actual direction of magnetisation can be along either of two opposite directions which are along an easy axis. The magnetically isotropic material has no preferential direction for its magnetic moment without a magnetic field applied to it. The magnetic anisotropy includes magnetocrystalline anisotropy, shape anisotropy, magnetoelastic anisotropy and exchange anisotropy. According to the magnetocrystalline anisotropy, the atomic structure in a crystal can affect the preferred direction of magnetisation. Consequently, the demagnetising field in an oblate particle is not equal for all directions. Then one or more easy axis will be created by the shape anisotropy. The tension may change the behaviour of magnetisation which called as magnetic shape anisotropy.

In the micromagnetic simulation, the magnetic anisotropy usually will be considered as uniaxial magnetic anisotropy or cubic magnetic anisotropy.[30] In a single domain model, the magnetisation can be written as

$$\boldsymbol{M}=\frac{\mu}{V}=Ms(\alpha,\beta,\gamma) \tag{2.9}$$

The M_s is the saturation magnetisation and α,β,γ are direction cosines which can be combined as a unit vector. The α,β,γ can be written as $\alpha^2+\beta^2+\gamma^2=1$. The magnetic anisotropy energy is dependent on the direction cosines. For uniaxial anisotropy the angular dependence is as follows.

$$E=KV(1-\gamma^2)=KVsin^2\theta \tag{2.10}$$

There is one easy axis in a uniaxial anisotropy magnetic particle. The V is the volume, K the anisotropy constant, and θ the angle between the easy axis and the particle's magnetisation.

2. 3. 3 Shape anisotropy

The origin of the shape anisotropy is from the dipole interaction of the magnetised material. The diploe interaction also known as the stray field energy and demagnetisation energy. The magnetised material can be considered as the aggregation of many macroscopic dipole magnets. Because of the exchange energy the system prefers the dipole magnets aligning the same direction which displays a low energy configuration. However, in a ferromagnetic material, the magnetic dipoles generate the demagnetisation field H_d. The demagnetisation field coms from the poles at the surface of the material which display an opposite direction as the magnetisation field. The internal field in the magnetic material can be expressed as the combination of applied magnetic field and demagnetisation field.

In pattern to micro size/nanoscale structure, the demagnetisation field will induce a shape anisotropy in the structure. The single domain particle has been demonstrated in Figure 2. 3.

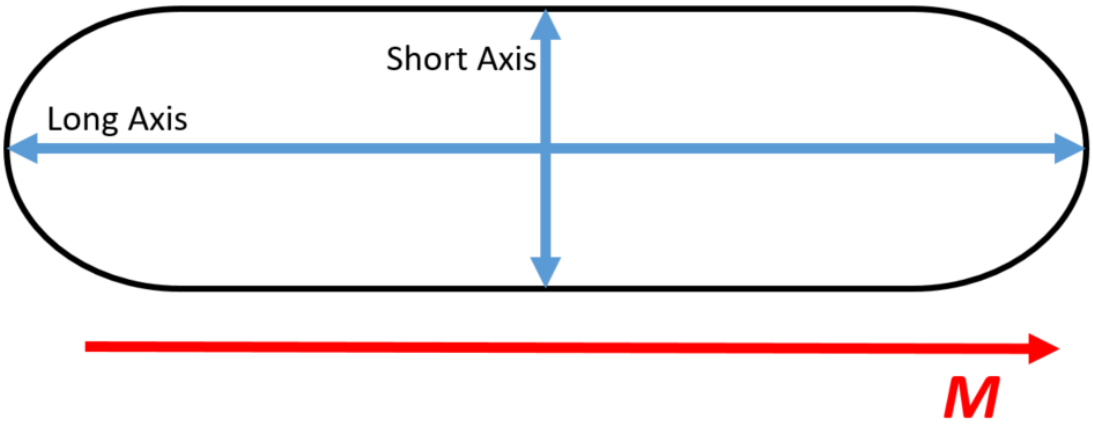

Figure 2.3 Illustration of single domain particle, the short axis and long axis have been marked in the Figure

The elliptical shape single domain particle displays short axis and long axis in a different direction. The shape anisotropy result from the diploe interaction in the single

domain particle. The shape anisotropy energy is related to the demagnetisation field which can be expressed as:

$$E_{Shape} = \frac{1}{2}(N_{long}cos^2\theta - N_{short}sin^2\theta)M^2 \quad (2.11)$$

The N_{long} and N_{short} are the demagnetisation factor which represents the long-axis demagnetisation factor short-axis demagnetisation factor in the elliptical sample. The shape anisotropy depends on the angle θ between the easy axis and magnetisation. When the sample is spherical, the shape anisotropy in all the direction is the same which means the shape anisotropy is zero. The shape anisotropy can be used to design nanostructures, such as the domain wall and magnetic skyrmion based device. The shape anisotropy can modulate the domain wall and skyrmion behaviour in the nanoscale device.

2. 3. 4 Zeeman Energy

The Zeeman energy represents the external field energy. The origin of the Zeeman energy is from the interaction between the magnetisation and the external field. The size of the Zeeman energy is dependent on the angle between the field and the magnetisation vector in the material. The energy density of the Zeeman energy can be explained as:

$$\mathrm{E}_{zeem} = -\mu_0 H \cdot \boldsymbol{M} \quad (2.12)$$

The Zeeman energy has a minimum energy state when the spins in the material align in the same direction as the external field.

2. 4 Magnetoresistance

Magnetoresistance effect means that the resistance of the device can be controlled by changing the applied magnetic field. The Magnetoresistance effect plays an important role in the modern magnetic based electronics device. The magnetic resistivity can be determined as:

$$\mathrm{MR} = \frac{\mathrm{p(H)-p(0)}}{\mathrm{p(H))}} \times 100\% \tag{2.13}$$

The $p(0)$ is the resistance of the device when the applied magnetic field is 0, and the p(H) is the resistance when the magnetic field is H.

The change of magnetoresistance depends on many parameters, and many kinds of magnetic resistance have been discovered, such as the anisotropic magnetoresistance effect and the giant magnetoresistance effect. The anisotropy magnetoresistance is governed by the angle between the direction of current and the direction of the magnetisation of the device [31, 32]. It is a relatively weak phenomenon, as in general electrical resistance variations of such system can be only a few percent at most.

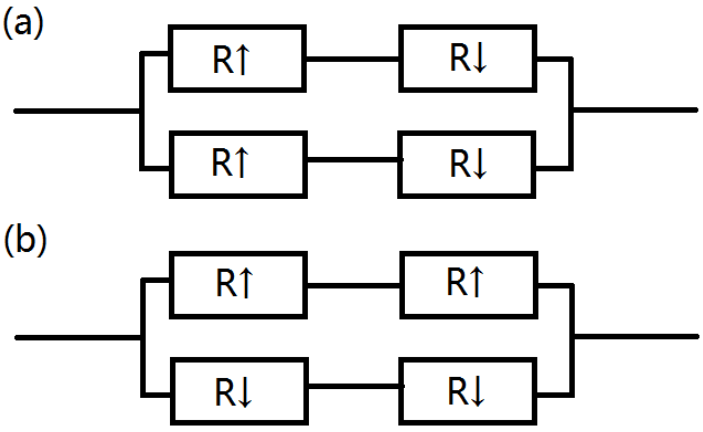

Figure 2.4 The Mott current modelling, R↑ means the magneto-resistance of with a spin up direction and R↓ means the magneto-resistance with a spin down direction. (a) The high resistance mode. (b) The low resistance mode.

Abert Fert and Peter Grunberg were awarded the 2007 Nobel Prize because of their discovery of the giant magnetoresistance (GMR) effect in 1988 [3, 4]. GMR system is a tri-layer structure where a metallic conductor separates two ferromagnetic layers. The relative orientation of the ferromagnetic layer magnetisation can be changed by an applied magnetic field. This magnetisation orientation change will cause changes in conductance of the structure. When the two ferromagnetic layers have the same magnetisation direction, electrons of a single spin type can move easily through the system. While the magnetisation of the two ferromagnetic layers is opposed, however, electrons of both spin types are strongly scattered, causing higher electrical resistance.

From the Mott current model, the high resistance mode and low resistance mode can be determined. In Figure 2. 4(a), the high resistance mode is two resistance connected in parallel. Comparing with the low resistance mode in Figure 2. 4(b), the resistance of the device of the model in Figure 2. 4(a) is much larger.

2. 5 Domain and domain wall

The atomic magnetic moments in the magnetic domain are aligned parallel which is developed and suggested by Weiss [33]. The reason for the spontaneous alignment of atomic moments within a ferromagnetic material has been explained by Weiss who came up with the so-called Weiss mean field. The Weiss mean field assumed that there are many magnetic moment regions in the bulk magnetic material. The magnetic moment in the magnetic moment regions are parallel. Also for the exchange interaction in ferromagnetic material, the system has minimised exchange energy when the spins are parallel. Moreover, the directions of the magnetic moments in different region are different. A region of saturated magnetisation is called a magnetic domain. The total dipole moment from all domains is equal to 0 when the ferromagnetic material is fully demagnetized. The total dipole moment will be changed by an external field [34].

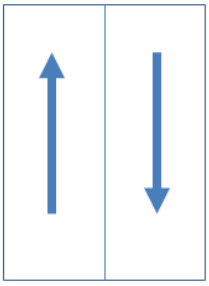

Figure 2.5 Magnetic domain wall is a varying direction of magnetisation usually with an angle as 90 degree or 180 degree.

According to the atomic lattice structure, the ferromagnetic material has an easy crystallographic orientation along which in combination with the applied field determines the magnetisation direction. Also, for the hard orientation clearly a larger field is required for the same magnetisation. Moreover, the magneto crystalline energy is the difference between the magnetisations along the hard axis and easy axis. The magneto crystalline energy can be minimised by forming domains along the easy direction. The boundaries of the domain are called domain walls. The domain wall is a varying direction of magnetisation usually with an angle as 90 degree or 180 degree. The width of the domain wall is determined by the exchange energy and the magneto crystalline energy. By increasing the size of the domain and decreasing the width of the domain wall, the magneto crystalline energy will decrease. The elastic strain energy required for deformation is called magnetostrictive energy. The magnetostrictive energy can be minimised by reducing the size of the domain and increasing the width of the domain wall.

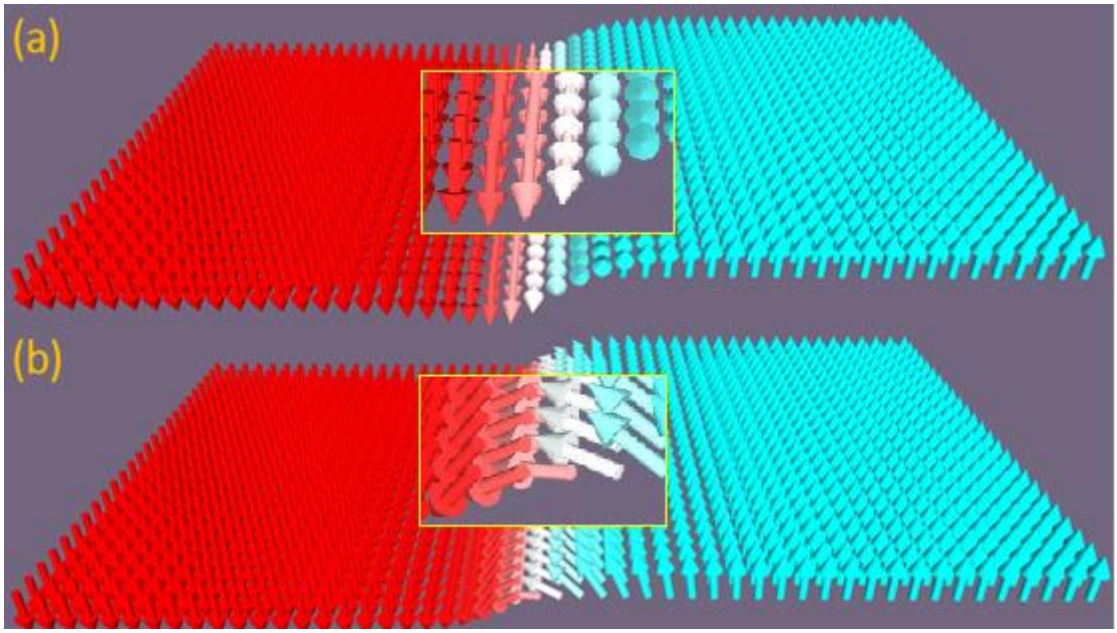

Figure 2.6 According to the direction of magnetisation in magnetic material, the domain has divided to (a) Bloch wall (b) Neel wall

According to Figure 2.6, two types of wall can be defined. The Neel wall is a domain wall with an in-plane direction which given in Figure 2.6 (a), and the Bloch wall is a domain wall with an out-of-plane direction which has been given in Figure 2.6(b). The domain walls have been proposed for advanced spintronics devices, such as the domain wall logical device, domain wall oscillator and racetrack memory [17-19, 22, 35, 36]. The domain wall based racetrack memory device is given in Figure 2.7. The racetrack memory is a ferromagnetic nanowire and can display two states: have a magnetic domain wall/without a magnetic domain wall. The domain wall in the nanowire can be driven by the spin current and past the read and write elements.

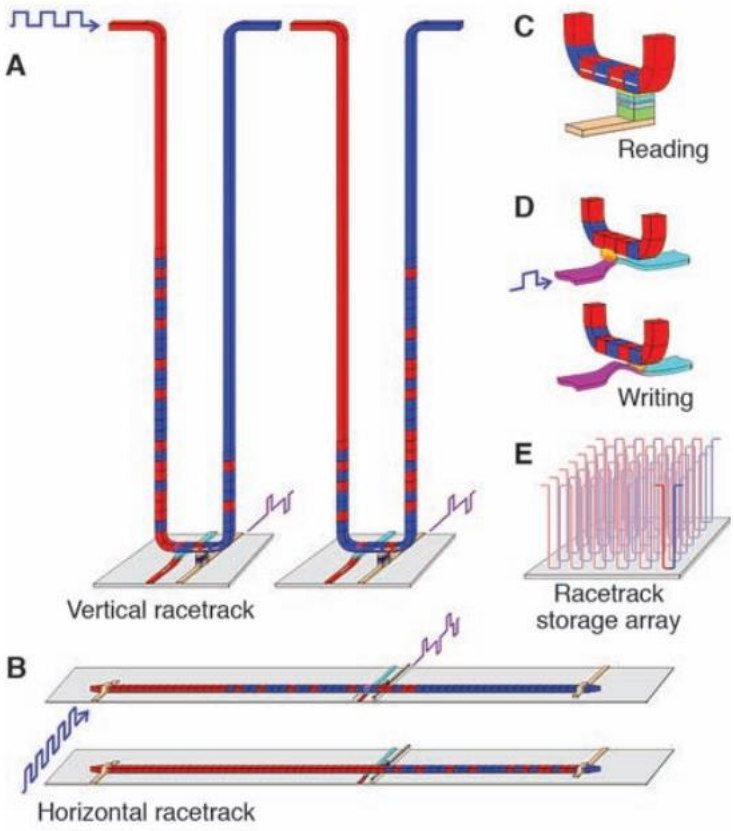

Figure 2.7(a) The domain wall driven by spin polarized current in the vertical racetrack memory. (b) The domain wall driven by spin polarized current in the horizontal racetrack memory. (c) Reading process in the racetrack memory. (d) Writing process in the racetrack memory. (e) Arrays of racetracks are built on a chip to enable high-density storage. Ref.[22]

2. 6 Magnetic skyrmions and Skyrmion Hall effect

Magnetic skyrmion can be expressed as a topological soliton or a topological defect in condensed matter system [37-41]. The skyrmion was proposed by Tony Skyrme, a nuclear physicist in 1960's. Magnetic skyrmions can be seen as quasi-particle-like topological excitation in certain field theories for the description of the interaction of points [42]. Then in 1990's, the existence of topologically protected skyrmion in magnetic material have been suggested by Bogdanov et al. in theoretically.[43] A.

Bogdanov and U. Rößler theoretically studied the skyrmion in magnetic thin film in 2001 [37]. Then S. Mühlbauer et al, demonstrated the skyrmion exit in B20-type bulk chiral magnetic MnSi which include broken inversion symmetry effect.

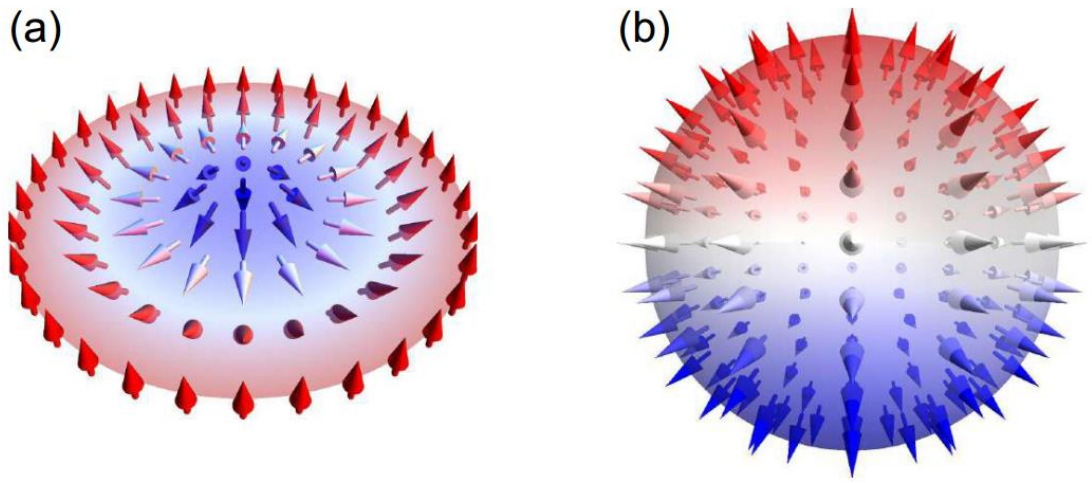

Figure 2.8 (a) Illustration of 2D magnetic skyrmion. The cone denote the spin direction and the spin component in the out of plane direction is represented by the color of the cone. (Red for spin direction which is out-of-plane, white for in-plane spin configuration and blue for into-plane spin configuration) (b) 2D skyrmion mapped to unit 3D spherical surface and point the spins in all direction. Ref.[44]

Recently, the creation and manipulation of magnetic skyrmion in different material systems have been reported [45-49]. Magnetic skyrmion displays high topologically protected stability and can be driven by external force. Due to the advantage of Magnetic skyrmion, they have potential usage in further information storage device and information processing devices [40, 41, 50]. Furthermore, skyrmion based logical device, spin-wave/magnon device and transistor-like functional devices have been reported recently [27, 49, 51]. The magnetic skyrmion based logical device is given in Figure 2.9, which is one of the most important applications of magnetic skyrmion. The skyrmion based logical device has much lower power and driving current than the domain wall based logical device. This kinds of device have the potential for use in novel magnetic sensors and spin logic

device. In the device, the magnetic skyrmions can be merging and duplication by the shape of the device which can display different logical states.

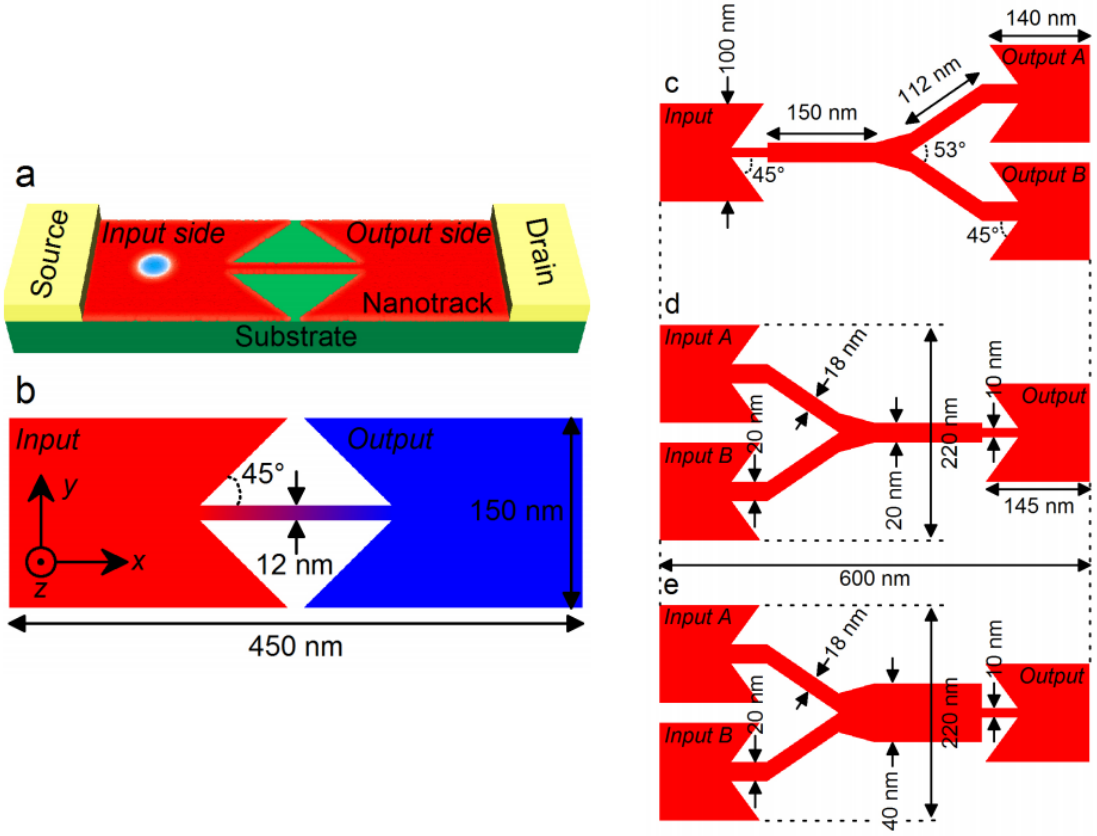

Figure 2.9 The basic design of the magnetic skyrmion logic gate system. Ref.[27] (a), Sketch of the simulated model. (b) The top-view of the design of the 1-nm-thick skyrmion conversion geometry. (c) The top-view of the design of the 1-nm-thick geometry for the skyrmion duplication. (d) The top-view of the design of the 1-nm-thick geometry for the skyrmion merging and the logical OR gate. (e) The top-view of the design of the 1-nm-thick geometry for the logical AND gate.

There exists a Skyrmion Hall Effect (SkHE), which is similar to the well-known ordinary Hall effect. The ordinary Hall effect is about the Lorentz force induced charged particle transverse deflection which reported by Edwin Hall in 1879 [52].

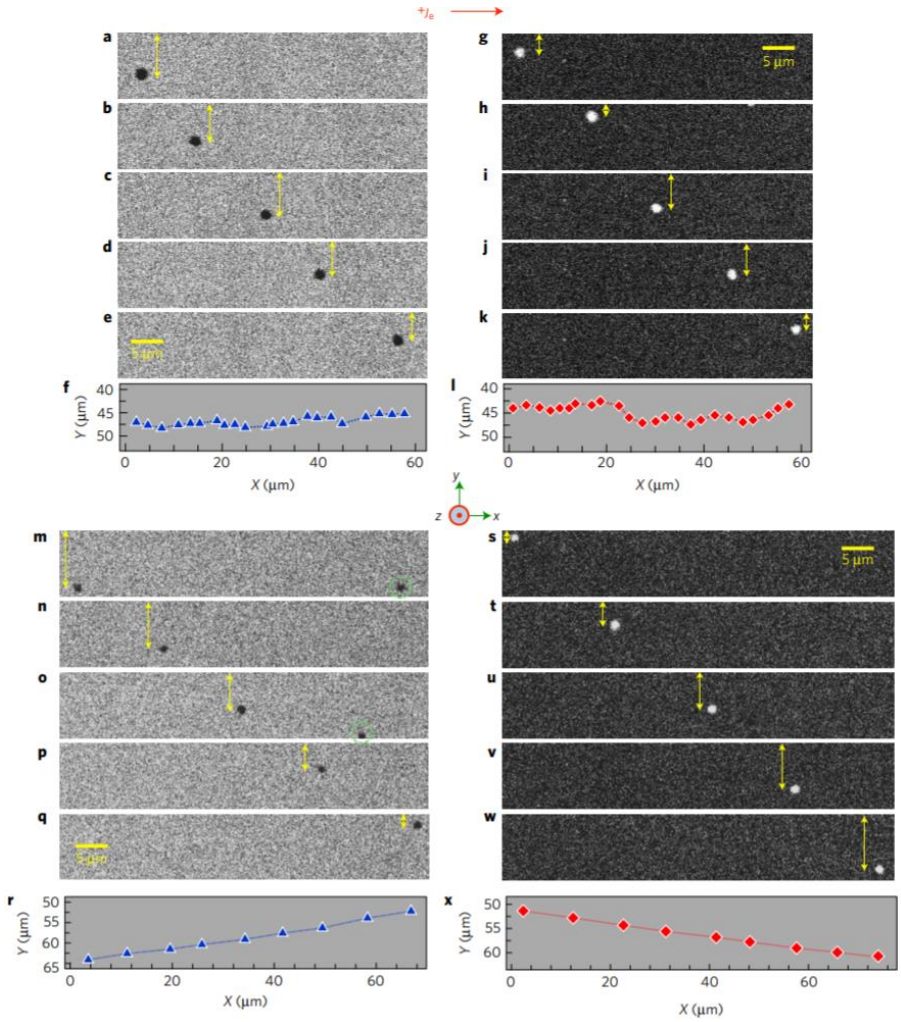

Figure 2.10 The MOKE microscopy images of pulse current-driven skyrmion motion Ref. [53]. (a-e) Snapshots of (Q= −1) skyrmion motion driven by a current along +*x* direction. (f) Summary of the skyrmion trajectory from (a–e).

The magnetic skyrmion can be driven by an external driving force, such as the magnon force, spin orbit torque and field gradient [51, 54-56]. Due to the Magnus force, the trajectory of the magnetic skyrmion motion will be affected. The phenomenon is known as the SkHE, which has been theoretically studied by Zang et.al. [57] and recently been directly observed by experiment by Jiang et al. and Litzius et al [53, 58]. The MOKE microscopy images of pulse current-driven skyrmion motion is given in Figure 2.9. The experiment result shows the trajectory of skyrmion in the nano-track is affected by the SkHE which induce a motion in *y* direction. When the magnetic skyrmion motion in the thin film or nano-track, the SkHE will induce the skyrmion moves at an angle with respect to the direction of the driving force [59].

2. 7 Magnetic skyrmion number

The skyrmion in magnetic materials can be characterised by a skyrmion number, which follows from the topological invariant. The skyrmion number can be written as:

$$Q = \frac{1}{4\pi}\int d^2 r S \cdot (\partial_x S \times \partial_y S) \tag{2.14}$$

The equation is only valid under the continuum condition, in which the spins in the system are almost parallel with their neighbours. There is also a method which can work under any dynamic processing [60]. The lattice version of the topological charge can provide a clear version of the spin evolution. This type of topological charge Q is first introduced in Ref.[61], which defined in a square lattice mesh illustrated in Figure 2. 11.

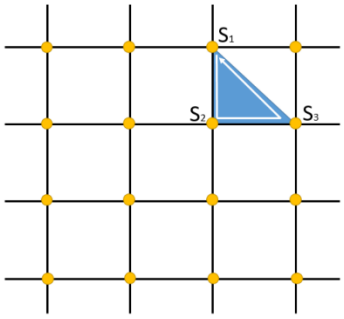

Figure 2.11 Triangulated square lattice. S1, S2 and S3 follow a counter-clockwise order on each triangle grid.

The solid angle of each triangle structure in Figure 2.11 is determined by

$$\exp\left(\mathrm{i}\frac{\Omega_\Delta}{2}\right) = p^{-1}[1 + S_1 \cdot S_2 + S_2 \cdot S_3 + S_3 \cdot S_1 + iS_1 \cdot (S_2 \times S_3)] \tag{2.15}$$

Where - $2\pi < \Omega < 2\pi$ and $p = [2(1 + S_1 \cdot S_2)(1 + S_2 \cdot S_3)(1 + S_3 \cdot S_1)]^{1/2}$ is the

normalization factor [61]. The topological charge Q in the lattice version can be calculated by

$$Q = \frac{1}{4\pi}\sum_{\Delta}\Omega_{\Delta} \tag{2.16}$$

And in the simulation works in this thesis, I use an equivalent expression in [62] which is easier to implement:

$$tan(\frac{\Omega_{\Delta}}{2}) = \frac{S_1\cdot(S_2\times S_3)}{1+S_1\cdot S_2+S_1\cdot S_3+S_2\cdot S_3} \tag{2.17}$$

Chapter.3 Magnetic modelling

3. 1 Micromagnetic simulation

The micromagnetic simulation can be used to simulate the magnetisation in the device and is an indispensable tool in the field of magnetism research. There are many open access micromagnetic simulation software such as the Object Oriented Micromagnetic Framework (OOMMF) and Mumax.[63, 64] The micromagnetic simulation can improve the performance of the spintronics device as well as design new type of the spintronics device. The tools calculate the simulation result by solving the Landau-Lifshitz equation which is given by:

$$\frac{dM}{dt} = -\gamma \boldsymbol{M} \times H_{eff} + \frac{\alpha}{Ms}(\boldsymbol{M} \times \frac{dM}{dt}) \tag{3.1}$$

Where $\boldsymbol{M}$ is the magnetisation of the magnetic layer, Ms is the saturation magnetisation, γ is the Gilbert gyromagnetic ratio and α is the damping constant. H_{eff} is the effective field, which is derived from the magnetic energy density,

$$H_{eff} = -\mu_0^{-1} \frac{\delta \varepsilon}{\delta M} \tag{3.2}$$

Where ε contains the Heisenberg exchange, anisotropy, applied magnetic field, and demagnetisation energy terms.

For micromagnetic simulations, the sample is usually divided into a finite size which can make the simulation much faster. The magnetisation can be expressed by a continuous field M(r), the r is a position vector. The magnetisation can be written as:

$$\boldsymbol{M}(r) = Ms \cdot m(r);\ \boldsymbol{m} \cdot \boldsymbol{m} = 1 \tag{3.3}$$

The *Ms* is the saturation magnetisation of the material and the ***m*** is the normalised vector of the magnetisation. The fundamental approximation of the micromagnetics is the continuous magnetisation vector to build the energy items. Usually, the Zeeman Energy, Exchange Energy, Anisotropic Energy and Demagnetizing Energy should be considered.

$$Heff = -\mu_0^{-1}\frac{\delta\varepsilon}{\delta M} = H_{exch} + H_{anis} + H_{demag} + H_{zeem} \tag{3.4}$$

The exchange coupling in micromagnetics is a short-range interaction in nature and typical exchange energy for the dipole pair can be expressed with terms of the relative angular orientation of the coupled spins. The exchange energy between two neighbouring atoms can be expressed by the Heisenberg model as.

$$e_x = -2J_{ij}S_i \cdot S_j \tag{3.5}$$

The S_i and S_j are the vectors of the spin, and the J is the exchange constant of these two atoms. Usually, the exchange constant of the ferromagnetic material is larger than 0. According to the formula (3.5), when the S_i and S_j are in the parallel, the exchange energy is the lowest and has ferromagnetism. In the micromagnetic approximation of long-wavelength magnetization changes, the exchange can be written as

$$H_{exch,x} = \frac{2A}{\mu_0 M_s^2}\nabla^2 M_x \tag{3.6}$$

$$H_{exch,y} = \frac{2A}{\mu_0 M_s^2}\nabla^2 M_y \tag{3.7}$$

$$H_{exch,z} = \frac{2A}{\mu_0 M_s^2}\nabla^2 M_z \tag{3.8}$$

$$H_{exch} = H_{exch,x}+H_{exch,y}+H_{exch,z} \tag{3.9}$$

In the calculation of the exchange field, the M_x is the magnetisation vector in the x-direction. The A is the material exchange constant, μ_0 is the vacuum permeability.

Furthermore, the anisotropic energy is considered by the micromagnetic simulation. The material displays the magnetocrystalline anisotropy, which arises from the electronics spin orbit coupling. The energy of the magnetocrystalline uniaxial anisotropy can be written as:

$$\varepsilon_K = \int (K_u sin^2\alpha) dV \tag{3.10}$$

α is the angle between the easy axis and the magnetisation unit vector $\boldsymbol{m}$. K_u is the constant of the magnetocrystalline uniaxial anisotropy.

The demagnetising energy can be calculated from the Maxwell equation group:

$$\nabla \cdot \vec{D} = p \tag{3.11}$$

$$\nabla \cdot \vec{B} = 0 \tag{3.12}$$

$$\nabla \times \vec{E} = -\frac{\partial \vec{B}}{\partial t} \tag{3.13}$$

$$\nabla \times \vec{H} = \vec{J} + \frac{\partial \vec{D}}{\partial t} \tag{3.14}$$

But if the device is in a situation without electric field E and current J, the equation (3.12) and (3.13) can be written as:

$$\nabla \cdot \vec{B} = 0 \tag{3.15}$$

$$\nabla \cdot \vec{H} = 0 \tag{3.16}$$

The magnetic induction intensity $\vec{B}$ can be written as $\vec{B} = \mu_0(\vec{H} + \vec{M})$, thus:

$$\nabla \cdot \overrightarrow{Hd} = -\nabla \cdot \vec{M} \tag{3.17}$$

$$\nabla \cdot \overrightarrow{Hd} = 0 \tag{3.18}$$

When a magnetic field is applied to the system, the Zeeman interaction will turn the magnetisation in the system to the same direction as the applied magnetic field. The Zeeman density ε_{zeem} can be expressed as:

$$\varepsilon_{Zeeman} = -\mu_0(M \cdot \mathrm{H}_{Applied}) \tag{3.19}$$

Where $H_{Applied}$ is the applied magnetic field and μ_0 is the vacuum permeability constant.

3. 2 Atomistic spin model

The atomistic simulation is focused on simulating the atomistic spin dynamics in the magnetic material system. The atomistic modelling is similar to the molecular dynamics approach but in the atomistic model the atomic displacement is usually not considered. The Hamiltonian in atomistic modelling is similar to the micromagnetic simulation which includes the exchange energy, anisotropy energy, magnetostatic energy and external field energy. Importantly, however, the exchange is calculated exactly using the Heisenberg formalism rather than the micromagnetic approximation. This allows the atomistic model to be used at high temperatures where short wavelength fluctuations invalidate the micromagnetic approximation. The dynamics of atomic spin moment is described by the Landau–Lifshitz–Gilbert (LLG) equation. The parameters

for the atomistic simulation can be measured from the experiment or calculated by *ab initio* density function theory calculations. The exchange coupling constant used in the atomistic modelling is related to the Curie temperature Tc via $J_{ij} = 3k_B T_c/(\varepsilon z)$. The J_{ij} is the exchange constant, and the ε is dependent on the crystal structure and coordination number. This allows J_{ij} to be calculated from the measurements of T_C.

The energy of the system is described by the following Hamiltonian, which includes all the energy contribution to the magnetic behaviour of the system, including the Heisenberg form of exchange:

$$\mathrm{H} = -\sum_{i<j} J_{ij}\overrightarrow{S_i}\cdot\overrightarrow{S_j} - \sum_i k_u^i\left(\overrightarrow{S_i}\cdot\hat{e}\right) - \mu_0\sum_i \mu_S^i\overrightarrow{S_i}\cdot\overrightarrow{H_{app}} + H_{demag},$$

Where the J_{ij} is the exchange interaction between the spins on site i and j, K_u is the uniaxial anisotropy energy on site i along the axis $\hat{e}$, μ_S^i is the atomic spin moment on the atomic site i in unit of μ_B and μ_0 is the permeability constant. The parameter in this equation can be measured by the experiment or calculated by ab initio density functional theory (DFT) calculations.

3. 3 Landau-Lifshitz equation and spin torque

The spins in the non-ferromagnetic material device usually are randomly oriented and not display a role in the function of the device. However, when the ferromagnetic material is incorporated to the device, the spins can become partially spin polarized and these spins can play an important role in device function. After the spin transfer torque effect, has been determined, the spins configuration in the device can be changed by a spin polarized current. Spin transfer torque was proposed by J. Slonczewski and L.

Berger independently in 1996 [13, 14].

In the magnetic simulation, the simulation tools calculate the simulation result by solving the Landau-Lifshitz -Gilbert(LLG) equation which is given by

$$\frac{dM}{dt} = -\gamma M \times H_{eff} + \frac{\alpha}{M_S}(M \times \frac{dM}{dt}) \tag{3.20}$$

Where M is the unit vector magnetisation of the magnetic layer, M_s is the saturation magnetisation, γ is the gyromagnetic ratio and α is the damping constant which also represents the coupling between the spin and the heat bath (thermal effect). H_{eff} is the effective field, which is derived from the magnetic energy density.

The figure of the Landau-Lifshitz equation and Landau-Lifshitz Gilbert equation is given in Figure 3.1 [65]. The magnetisation precession for undamped motion and motion with damping are included in Figure 3. 1. To take into account the spin torque the format of magnetisation of the equation 3.20 can be written as

$$\frac{\mathrm{d}\boldsymbol{M}}{\mathrm{dt}} = -\gamma \boldsymbol{M} \times \mathrm{H}_{eff} + \frac{\alpha}{\mathrm{Ms}}\left(\boldsymbol{M} \times \frac{\mathrm{d}\boldsymbol{M}}{\mathrm{dt}}\right) + \tau_{STT} \tag{3.21}$$

Where the Ms is the saturation magnetisation. The quantity τ_{STT} in equation 3.21 is the combination of the Slonczewski spin-transfer torque(STT) adiabatic and non-adiabatic STT term[66]

$$\begin{aligned} \tau_{STT} &= \tau_{adiab} + \tau_{nonadiab} \\ \tau_{adiab} &= -um \times \left(m \times \frac{\partial m}{\partial x}\right) \\ \tau_{nonadiab} &= -\beta um \times \frac{\partial m}{\partial x} \end{aligned} \tag{3.22}$$

Where $\mathrm{u} = \left|\frac{\gamma h}{\mu_0 e}\right| \frac{jP}{2M_S}$ is the STT coefficient. h is the reduced Plank constant, e is the

electron charge, j is the applied current density, and P is the spin polarization rate. For the non-adiabatic STT term $\tau_{nonadiab}$, the β is the non-adiabatic coefficient.

.

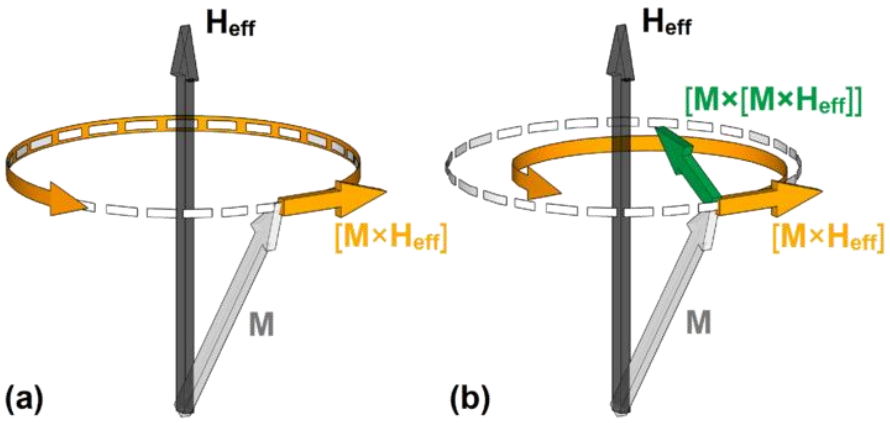

Figure 3.1 Illustration of the magnetisation precession for (a) undamped motion and (b) motion with damping. Ref. [65]

The phenomenological description of spin transfer torque developed by Stiles is given in the following [67]. In the free-electron model, the origin of the spin torque can be ascribed to three distinct processes that contribute to the spin angular momentum transfer through a perfect interface. There is a discontinuity in the transverse spin current induced by the spin-dependent reflection and transmission. Because the reflection probabilities are spin-dependent, the resulting spin-filtering effect will lead to the discontinuity of the spin components and one part of the transverse spin current is adsorbed at the interface. Rotation of the scattered spins from the interface will lead to another component of the spin torque, which is perpendicular to the plane formed by free layer magnetisation and fixed layer magnetisation. First principle electronic calculations based on the free-electron model show that the transverse component of the itinerant spins will be nearly zero after averaging over the whole Fermi surface. Comparing with the applied field, use of the spin polarized current to control the spin configuration in the device is more convenient. The capacity of the MRAM technology has increased to a new level because the spin transfer torque effect was used.

When the current goes through a heavy metal layer with a strong spin orbit coupling, the charge current will be transferred to a spin current due to the spin Hall effect (SHE). Then the spin current induces spin accumulation at the surfaces of the heavy metal layer. If the structure includes a ferromagnetic layer and a heavy metal layer, the spin current will go through the FM layer and excite spin orbit torques (SOTs) on the FM layer. The SOT term can be written as:

$$\tau_{IP} = -\frac{u}{b} m \times (m \times p) \tag{3.23}$$

$$\tau_{OOP} = -\beta u m \times \frac{\partial m}{\partial x}$$

3. 4 Dzyaloshinskii-Moriya interaction

The Dzyaloshinskii-Moriya interaction (DMI) is induced by antisymmetric exchange interaction caused by the spin orbit coupling in the material system [68, 69]. The DMI effect can be found at the interface between the magnetic layer and heavy metal layer with strong spin orbit coupling. On the other hand, DMI can also be found in bulk materials with inversion symmetry.

For the DMI at the interface between magnetic layer and heavy metal layer with strong spin orbit coupling. The DMI can be expressed as:

$$H_{iDM} = d_{iDM} \sum_{<i,j>} (u_{ij} \times \hat{z}) \cdot (S_i \cdot S_j) \tag{3.24}$$

Where d_{iDM} is the interface DMI coupling energy, $<i,j>$ is the NN exchange sites, S_i and S_j is the unit spin vector at sites i and j. The u_{ij} is unit vector between S_i and S_j and

$\hat{z}$ is the normal to the interface. In the micromagnetic modelling, the interface DMI has been consider as the average energy density ε_{iDM}:

$$\begin{aligned}\varepsilon_{iDM} &= D_{iDM}[m_z(m\cdot\nabla)-(\nabla\cdot m)m_z] \\ &= D_{iDM}\left(m_z\frac{\partial m_x}{\partial x}- m_x\frac{\partial m_z}{\partial x}+ m_z\frac{\partial m_y}{\partial y}- m_y\frac{\partial m_z}{\partial y}\right)\end{aligned} \quad (3.25)$$

The D_{iDM} is the continuous effective interface-induce DMI constant (in Jm^{-2}), m_x, m_y and m_z are the *xyz* components of the reduced magnetisation *m*. The relationship between the D_{iDM} and d_{iDM} is depended on the crystal structure and scales as the $\frac{1}{at}$. (*a* is the lattice constant and the *t* is the thickness of the thin film.) The 1/t scaling of the interface induced DMI is based on assumption. For the simple cubic lattice, the D_{iDM} is obtains as $d_{iDM}/ab = d_{iDM}/Na^2$ which is along the (001) direction. Moreover, for face-centered-cubic lattice oriented, the D_{iDM} is obtains as $d_{iDM}\sqrt{3}/ab = 3d_{iDM}/Na^2$ and along the (111) direction. (*N* is the number of atomic planes in the film)

For the atomistic scale, the bulk DMI induced by the symmetry broken in bulk materials, such as the MnSi, $Fe_{1-x}Co_xSi$ and FeGe [39, 45]. The equation of this uniform interaction H_{bDM} can be expressed as:

$$H_{bDM} = d_{bDM}\sum_{<i,j>} uij\cdot\left(S_i\times S_j\right) \quad (3.26)$$

In the micromagnetic modelling, the bulk DMI has been considered as the average energy density ε_{bDM}:

$$\begin{aligned}\varepsilon_{bDM} &= D_{bDM}[m_z(m\cdot\nabla)-(\nabla\cdot m)m_z] \\ &= D_{bDM}\left(m_z\frac{\partial m_x}{\partial y}- m_x\frac{\partial m_z}{\partial y}+ m_z\frac{\partial m_y}{\partial x}- m_y\frac{\partial m_z}{\partial x}\right)\end{aligned} \quad (3.27)$$

The D_{bDM} is the bulk DMI constant (in $J\ m^{-2}$)

Chapter.4 Magnetic domain wall engineering in a nanoscale permalloy junction

Nanoscale magnetic junctions provide a useful approach to act as building blocks for magnetoresistive random access memories (MRAM), where one of the key issues is to control the magnetic domain configuration. Here, I study the domain structure and the magnetic switching in the Permalloy ($Fe_{20}Ni_{80}$) nanoscale magnetic junctions with different thicknesses by using micromagnetic simulations. It is found that both the 90-° and 45-° domain walls can be formed between the junctions and the wire arms depending on the thickness of the device. The magnetic switching fields show distinct thickness dependencies with a broad peak varying from 7 nm to 22 nm depending on the junction sizes, and the large magnetic switching fields favour the stability of the MRAM operation.

4. 1 Magnetisation based spintronics device

The magnetoresistive random access memory (MRAM) based on the tunnelling magnetic resistance (TMR) effect has the potential to replace all existing memory devices in a computer or other hard disk drives as it could provide a high read/write operation speed and is also non-volatile [70-76]. On the other hand, the magnetic domain wall gives a flexible approach in the data storage and the logic circuit [18, 22, 77]. The magnetic logic gate demonstrates a high speed and low power. Compared with the TMR-based MRAM devices, a domain wall motion-based magnetic junction could have a single layer structure, which might have great advantages in terms of fabrication and application [78-80]. The magnetic junction shows several types of the

magnetoresistance effect by applying the magnetic field [81, 82].

4. 2 Magnetic domain in the junction structure device

The magnetic switching in the junction structure can be controlled by either the external magnetic field or the applied electrical current [32, 83]. Recently, it has been reported that the magnetic switching induced by the spin-transfer torque (STT) can enable the junction to work as a STT-MRAM device [84, 85]. There are also reports about the spin-polarized current that can induce the junction to generate spin waves [86-88]. It is found that the Permalloy junction has several metastable magnetisation states, which can be used to store the information [32]. Thus, the reliable control of the magnetic domain configuration in the magnetic junction is an important task. Here, I present a micromagnetic study of the domain structures and the magnetic switching in the nanoscale Permalloy junctions within magnetic cross structures with different thicknesses. The SEM micrograph of the junction structure device has been given in Figure 4.1. The junction structure device has two long arms which are cross to each other. The long arms provide a very strong shape anisotropy which make the spin configuration in the arms parallel to the long axis arms. The spin configuration in the cross structure is dependent on the long axis arms which can be modulated by the external field.

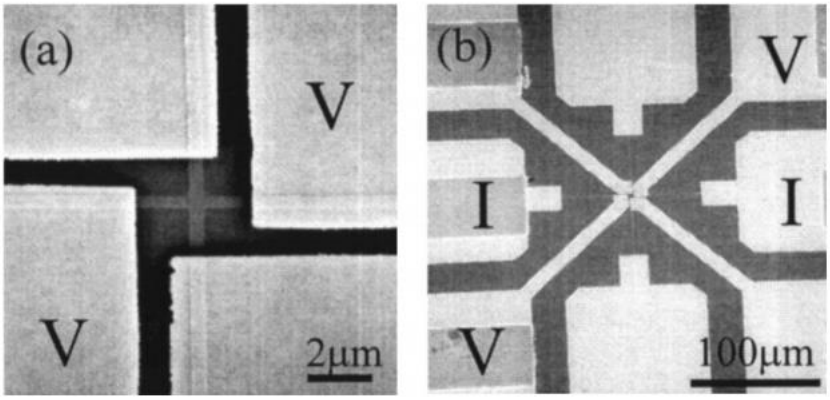

Figure 4.1 (a) SEM micrograph around the junction area of a 0.5mm width cross, and (b)

large-scale micrograph showing the electrical contact geometry. Ref.[32] The junction device has two long axis arms which provide strong shape anisotropy. The spin configuration in the cross structure is determined by the spin configuration in the long axis arms.

The initial state for the device is relaxed from random magnetisation, which shows different angle of the domain wall in the cross structure. All the initial magnetic switching and the coercivity show nonlinear dependences on the thickness, indicating the importance of controlling the thickness for the writing process when the nanoscale Permalloy junction works as a building block for information storage devices.

4. 3 Micromagnetic modelling

The numerical simulations are carried out by using the Object Oriented Micro Magnetic Framework (OOMMF) software [63]. The OOMMF is based on the LLG equation which has been introduced in Chapter 3.3. The magnetic material used for the micromagnetic simulation is Permalloy, i.e., $Fe_{20}Ni_{80}$, which has a low coercivity and a high permeability. The cross structure of the nanoscale junction is defined as 10 nm × 10 nm with varying thickness from 2.5 nm to 25 nm, and the length of all the wire arms is fixed at 200 nm, in order to provide a strong shape anisotropy. The illustration of the junction structure device is given in Figure 4.2. The saturation magnetisation is equal to 8.6×10^5 A/m. The exchange stiffness and the crystalline anisotropy constant are set at 13×10^{-12} J/m and 0 J/m^3, respectively. The simulation cell size is set as 2.5 nm × 2.5 nm × 2.5 nm, which is compared with the exchange length (5.3 nm) of Permalloy.

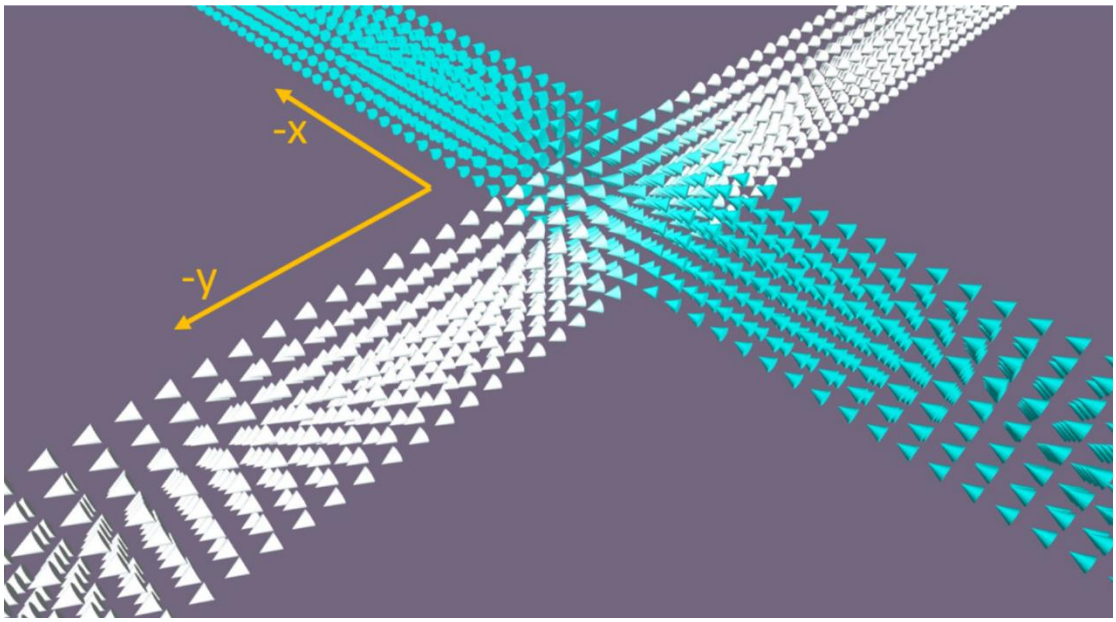

Figure 4.2 The illustration of the junction structure device. The spin configuration in the cross structure is depend on the spin configuration in long axis arms. The spin configuration in blue means the spin configuration is along –x direction, and the white means the spin configuration toward y direction which means the x-component spin configuration is zero.

4. 4 Initial state for the junction structure device

When the whole system relaxes from the random magnetisation, the spin configuration in the cross structure will display different state. The long arm can be explain as the x arm which is parallel to the *x*-direction and y arm which is parallel to the *y*-direction. The simulation starts with a different random seed, I will get different initial state in the system for each value of the seed. The initial spin configuration for different random seeds is given in Figure 4. 3. The size of the simulation 200 nm * 200 nm * 2.5 nm and the cross structure is 10 nm * 10 m, the cell size for the simulation is 2.5 nm * 2.5 nm * 2.5nm. According to the initial state in Figure 4.3, the initial spin configuration can be concluded as having three possible states, the 90 degree state in Figure 4.3(a), the 45 degree state in Figure 4.3(b) and the 0 degree state in Figure 4.3(c).

The state of the cross structure is dependent on the magnetisation direction in the long arms. For the 90 degree state in Figure 4. 3 (a), the magnetisation in each part of the x arm and y arm is not the same, and there has appeared a domain wall near the cross structure. Then for the 45 degree state in Figure 4. 3, this state is the most stable state for the device (According to the shape anisotropy of this device), the magnetisation in x arm and y arm is along the same direction. The 45 degree state can also been seen as the coherent state which displays during the device working. The cross structure displays an intermediate state between 90 degree and 45 degree. For the 0 degree state in Figure 4. 3(c), the magnetisation direction in *y*-arm is not uniform and in *x* arm is along the same direction which makes the magnetisation direction in the cross structure along the x-direction.

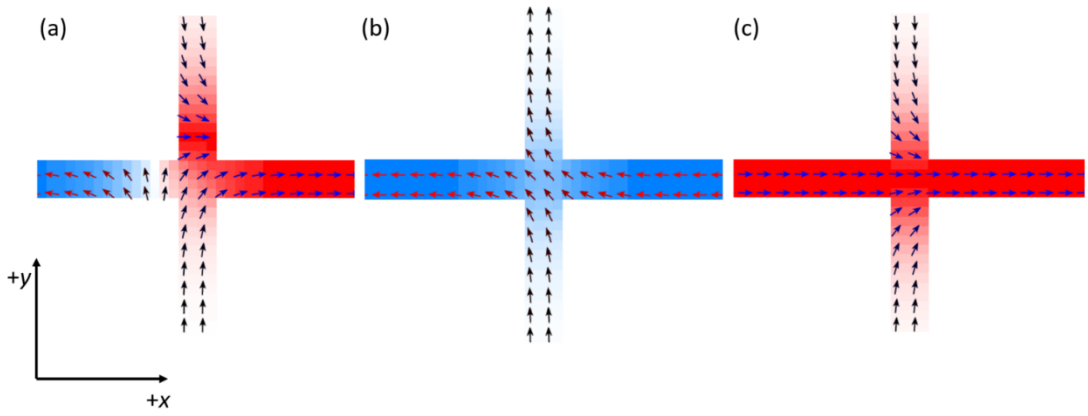

Figure 4. 3 The initial state of the junction structure device which is relaxed from the random magnetisation. (a) 90 degree domain wall state (b) 45 degree domain wall state (c) 0 degree domain wall state. The red is the magnetisation in +*x* direction and blue is magnetisation in –*x* direction.

4. 5 Transfer the initial state to the coherent state

During the magnetisation changing in the cross structure due to the external field, the initial state will be transformed to the coherent which can be observed in Figure 4.3, the 45 degree state. The 45 degree state shows high stability and can display four types

of the magnetisation state in the cross structure. The state transitions through an external magnetic field for the 90 degree and 0 degree state are given in Figure 4. 4 as below.

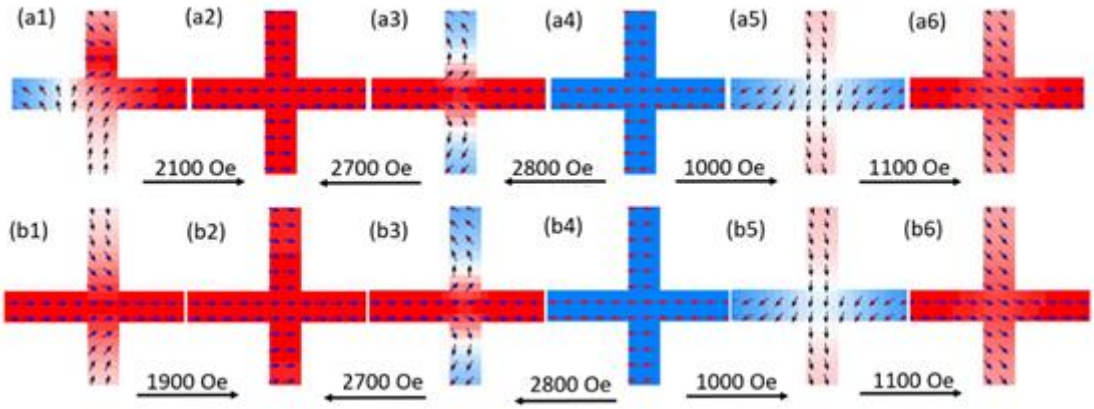

Figure 4. 4 The state transition from initial state to coherent state. (a1) - (a6) The state transition for the 90 degree state. (b1) – (b6) The state transition for the 0 degree state. The red is the magnetisation in +*x* direction and blue is magnetisation in –x-direction. The external field is along the x-direction.

According to the state transition in Figure 4.4 (a1-a6), the 90 degree state has transferred to a coherent state due to the external field along *x*-direction. The initial state is in Figure4.3 (a1) then an external H_x has been added into the system. The H_x increase from 0 Oe to 4000 Oe, the whole device is saturated when the H_x is larger than 2100 Oe. For the saturation state, the magnetisation in the device along the +*x* direction. Then the H_x reduce from 4000 Oe to -4000 Oe, the magnetisation switch to –x-direction when H_x larger than -2800 Oe. The magnetisation configuration for the device before switching is given in Figure 4.4 (a3) and the magnetisation saturate along –*x*-direction is given in Figure 4.4 (a4). When the H_x reduce to +*x* direction and larger than 1100 Oe the system switches to a coherent state. For the 0 degree state, the switching mechanism is similar to the 90 degree state. But the critical external field for the device switching to +*x* direction is smaller than the field in 90 degree case which has been given in Figure 4.4 (b1) – (b2). The smaller critical external field is because of the magnetisation in x arm. For the 90 degree state, the magnetisation in half of the x arm is along the –*x*-direction and another one is along the +*x*-direction. This kind of state needs a larger

external field to switch it than the 0 degree case.

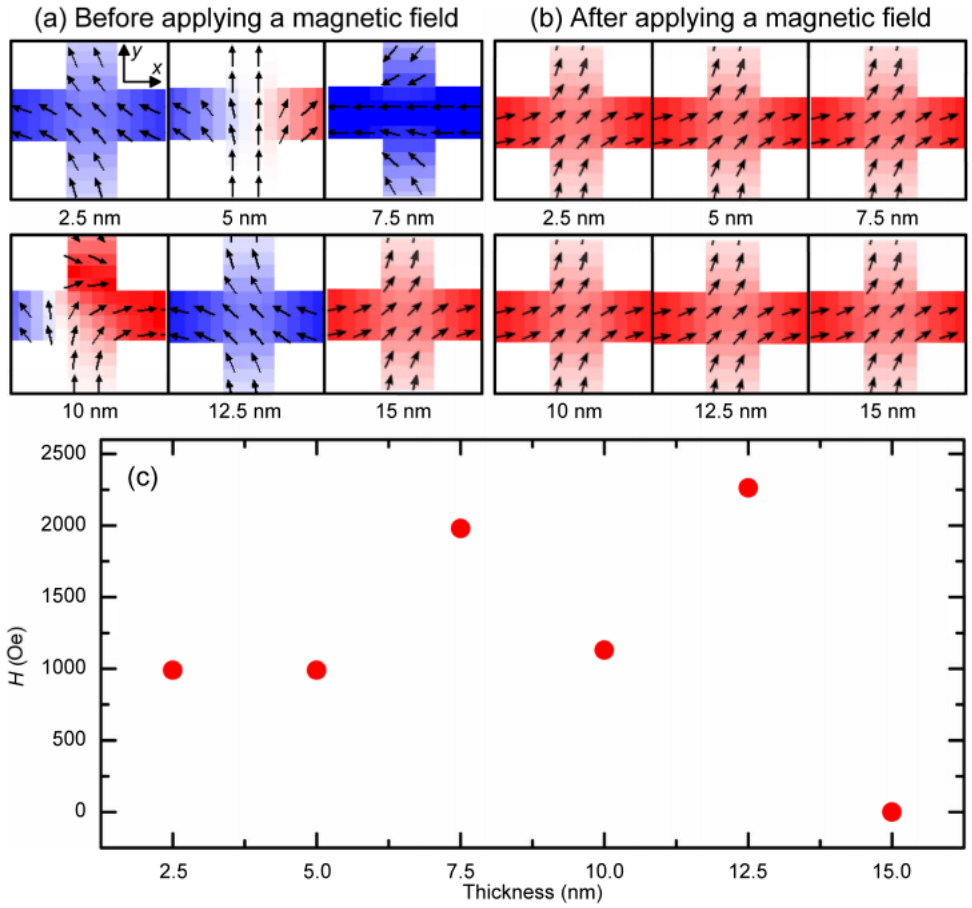

Figure 4.5 (a) The magnetic domain configurations in the cross structure relaxed from random magnetisation distributions for different thicknesses. (b) The magnetic domain configurations obtained by applying a magnetic field. (c) The amplitude of the magnetic field which changes the domain configurations shown in (a) to those shown in (b).

The initial state in different thickness device can also be transfer to the coherent state. The initially relaxed magnetisation distributions around the junctions of the cross structures with different thicknesses are shown in Figure 4.5(a), which are obtained by relaxing the cross structures with random magnetisation distributions(with 5 different random seed). Selected results are shown in Figure.4.5(a). The magnetisation in different layers of the device has the same direction which means the domain structure relax from the random magnetisaiton distribution is not related to the thickness of the

device.(Only depend on the random seed of the calculation) The spins in the wire arms are all aligned in parallel along with the wire directions due to the strong shape anisotropy. There are three types of domain configurations around the junctions. For the junctions with the thicknesses of 2.5 nm, 7.5 nm, and 12.5 nm, the spins in the junction are aligned in parallel with the spins in one of the wires, and the 90 domain walls form between other wires. For the cases with the thicknesses of 5 nm and 15 nm, the spins in the junctions are aligned largely in parallel, which can be described as a single magnetic domain or a coherent spin block (CSB), and the spin direction of these CSBs is in 45 with those in both wires. For the cases with a thickness of 10 nm, the spins in the junction form a 90 domain wall within the junction. Indeed, the initial magnetisation distribution in the cross structure can also be controlled by applying an external magnetic field. As shown in Figure 4.5(b), the initial magnetisation distribution in the cross structure can be modified to be a 45 domain by applying a magnetic field pointing at an angle of 45 to the x-direction. The required amplitude of the magnetic field corresponding to different thickness is given in Figure 4. 5(c). The applied magnetic field changes the domain structure to the coherent switching mode from the initially relaxed states, where the required magnetic field is different for samples with different initially relaxed magnetisation distribution and thickness.

4. 6 Magnetisation configuration in different layer

The magnetisation configuration in the junction device was studied. According to the shape of the device, the thickness of the device is much smaller than the length of each arm. Furthermore, the Permalloy is an in-plane material which makes all the magnetisation in the system is in-plane. Because of the exchange interaction in the ferromagnetic material, the magnetisation in each layer of the device is along the same

direction which has been given in Figure 4.6(a)-(f).

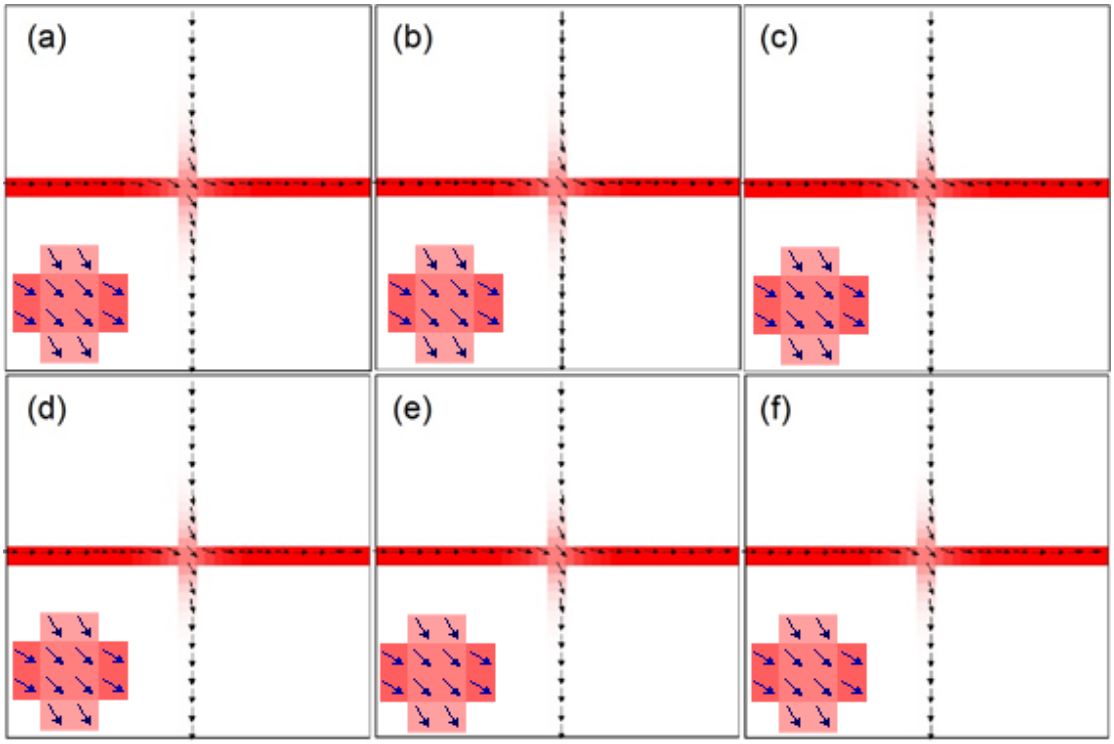

Figure 4. 6 Top views of the magnetisation distribution of the 100 nm × 100 nm × 7.5 nm junction at the (a) top, (b) middle, and (c) bottom layers. Top views of the magnetisation distribution of the 100 nm × 100 nm × 15 nm junction at the (d) top, (e) middle, and (f) bottom layers. The magnetisation distribution is uniform in the thickness direction of the device.

4. 7 Magnetisation switching in the cross structure

I studied the magnetisation switching process driven by an external magnetic field for the junctions with different thicknesses. The simulated hysteresis loops are the same in different layers of the device. Figure 4. 7 shows the result for the 2.5-nm-thick junction. The magnetic field is first applied along the + x-direction, of which the amplitude first increases from 0 Oe to 2000 Oe and reduces to 0 Oe. Then, the magnetic field changes in the same manner but along the –x-direction. The simulated hysteresis loop is given in Figure 4.7, and the magnetisation configurations illustrated in Figure .4.8 are corresponding to the marked states in the hysteresis loop given in Figure

4.7, which represent the magnetic switching process in the nanoscale junction. The initial magnetisation configuration in the nanoscale junction is given in Figure 4.8. The magnetic field of the first magnetic switching from the initially relaxed state to the state with a 45 domain wall is defined as the initial magnetisation switching field (H_i), which is indicated in Figure 4.7 (a). As the applied magnetic field increases from 0 Oe to 2000 Oe, the direction of the magnetisation in the junction is switched where the amplitude of the critical switching field, i.e., the coercivity (H_c) of the junction as indicated in Figure 4.7 (b), is equal to 1050 Oe.

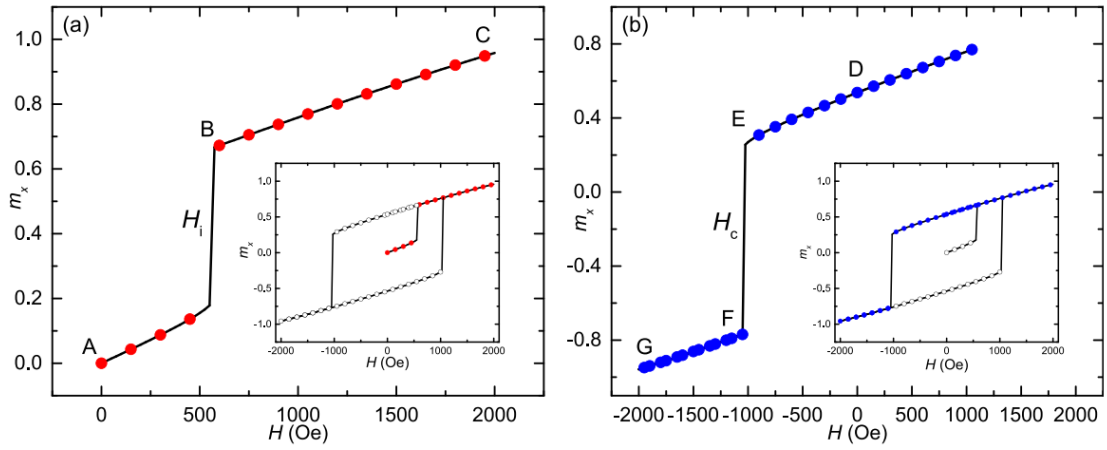

Figure 4.7 The hysteresis loop for the cross structure with the thickness of 2.5 nm. The initial switching magnetic field (H_i) and the coherence switching magnetic field (H_c) are indicated in (a) and (b), respectively.

The snapshots of the switching process given in Figure 4 .8 further show that the switching of the magnetisation in the junction is coherent. The angle between the x-axis and the spins at the junction is defined as θ. Before applying the magnetic field, the spins in the junction are in parallel with the y-axis, and the θ is equal to – 90 degree. By increasing the applied magnetic field above 2000 Oe, θ increases and then reaches 0. When the applied magnetic field is reduced to 0 Oe, θ decreases to – 45 degree. That means in the remanence state, the spins in the junction are aligned 45 degree away from the wire direction, and 45 degree domain walls are formed between the junction and the wires. When the applied magnetic field decreases from 0 Oe to –2000 Oe in the

x-direction, the spins change to be paralleled with the x-direction, and the θ increases from – 45 degree to 0. It is found that the whole magnetisation switching process in the junction is coherent and reversible.

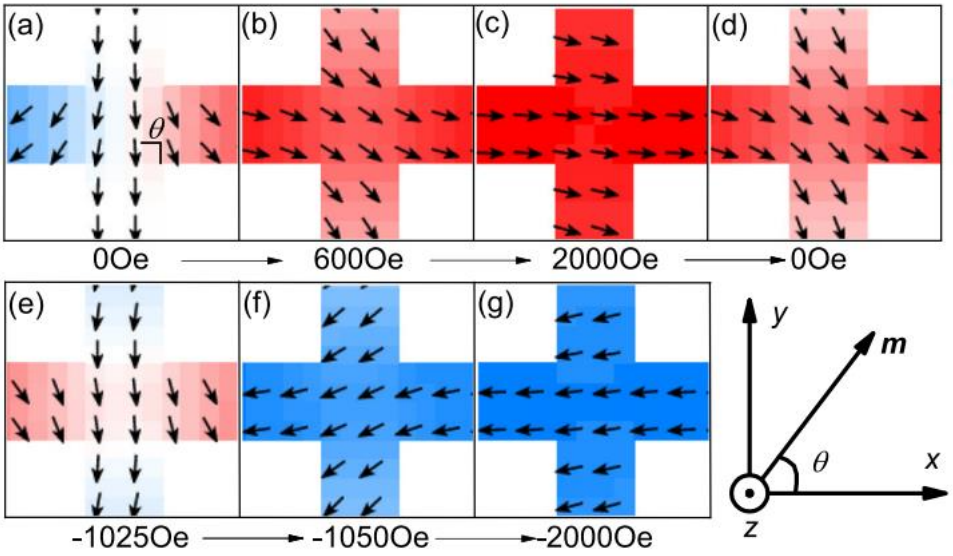

Figure. 4.8 The magnetic domain configurations of the 2.5-nm-thick junction at different applied magnetic fields. The magnetic field is applied along the x-direction. The labels correspond to the states indicated in Figure 2, i.e., (a) H = 0 Oe, (b) H = 600 Oe (before switching), (c) H = 2000 Oe (after switching), (d) H = 0 Oe, (e) H = – 1025 Oe (before switching), (f) H = – 1050 Oe (after switching), and (g) H = – 2000 Oe.

The typical spin configurations during the magnetic switching process of the junctions with different thicknesses are shown in Figure 4. 9. From Figure 4. 9 (a), I found that the junction with a different thickness usually has a different relaxed state. Before using the magnetic field to achieve reversible magnetic switching in the cross structure, the spins in the cross structure have to be tuned to the coherent switching mode. The coherent switching mode is defined as the states in Figure 4.8 (b) which shows 45 degree domain walls. The magnetization always displays a coherent state after applying the external field. The processes to enable the coherence switching modes are shown in Figure 4. 5. Unlike the magnetic switching processes shown in Figure 4.8, the relaxed magnetisation configuration at 0 Oe is different from the junctions with the

thicknesses of 5 nm, 7.5 nm, 10 nm, 12.5 nm, and 15 nm with the same random seed in OOMMF. The magnetisation switching in junction device with different initial state and thickness is shown in Figure 4. 9.

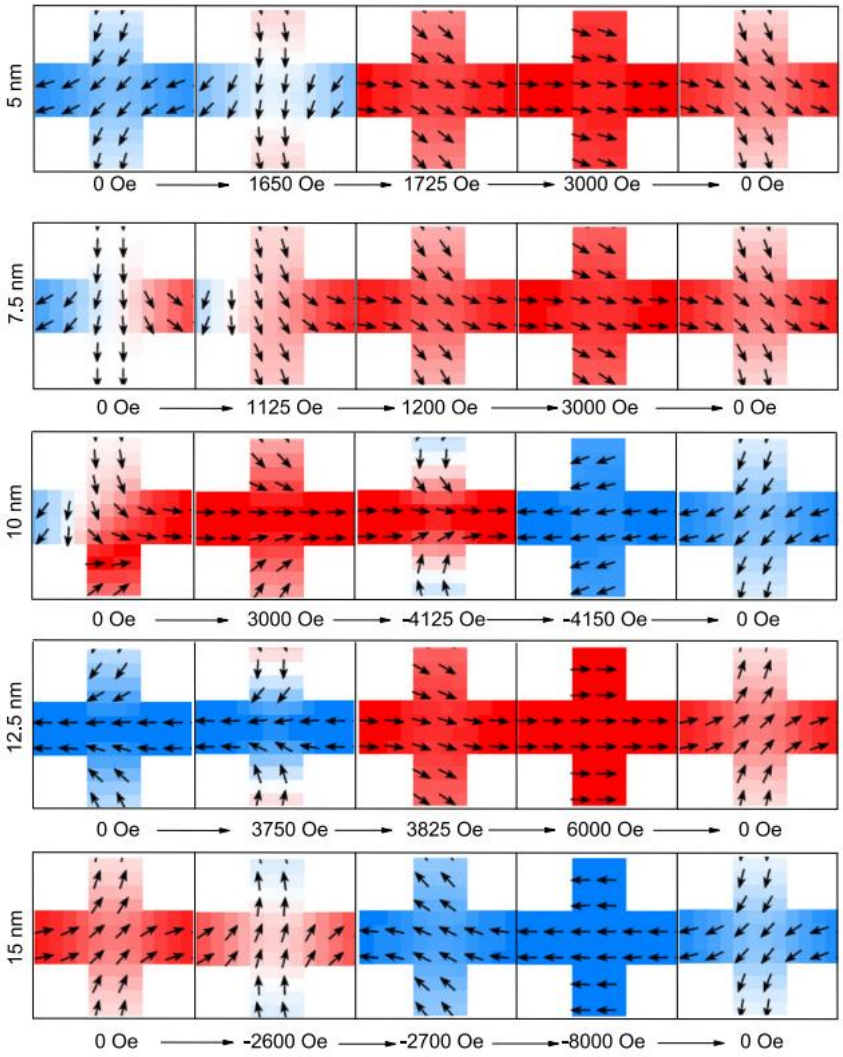

Figure 4. 9 The magnetic domain configurations of the junctions at different applied magnetic fields for different thicknesses. The magnetic field is applied along the x-direction.

The spin configurations of the junctions with the thicknesses of 5 nm and 15 nm are similar to the spin configurations in Figure 4.8 (d) which are in the coherent switching mode. The junction with a thickness of 7.5 nm has the parallel spins in the cross structure with a θ as –90 between the x-direction. As the magnetic field increases to

3000 Oe, θ decreases to 0 in the junction. When the magnetic field reduces back to 0 Oe, θ increases to 45, and the CSB is formed. From the junction with a thickness of 10 nm, the initial 90 DW within the junction can be eliminated, and the CSB can be formed by controlling the magnetisation process. When the thickness of the junction is 12.5 nm, the spins in the cross structure requires a large magnetic field up to 3825 Oe to reverse the magnetisation direction. For the whole cross structures with the thicknesses of 5 nm, 7.5 nm, and 10 nm, the spin configurations in the y-arms have not been changed, and the spin configuration in the x-arms can be switched. However, for the cross structures with thicknesses of 12.5 nm and 15 nm, the spin directions rotate along the y-axis as well. For the 45 degree domain wall, the AMR can be calculated as $R = \frac{1}{2} R_{max.}$ The AMR in the device can be changed by the external field which means the device can work as a memory device.

4. 8 Coercivity (H_c) of the junction device with different thickness and size

The magnetic switching field of the junction can be affected by the thickness of the junction. Figure 4. 10 shows H_c as a function of the thickness for the junctions with different lateral sizes. The size of the device is varying from 100 nm × 100 nm to 400 nm × 400 nm, i.e., the length of the cross structure is varying from 5 nm to 20 nm. H_c increases first with increasing thickness and then decreases, showing a broad peak from 7 nm to 22 nm depending on the junction sizes. The reason is that for the junction with a certain cross section size, the magnetisation switching is coherent. Thus, H_c is proportional to the total magnetisation, which also means H_c increases with the thickness as the total magnetisation is proportional to the thickness. However, when the thickness is larger than a certain critical value, multiple domains can be formed during the magnetisation switching, leading to incoherent magnetisation switching. In such a case, H_c decreases with the thickness, as the thicker junction is more likely to form

multiple domains, due to the demagnetisation effect. Besides, the critical value of the thickness increases with increasing lateral dimensions of the junction. The reason is that the amplitude of the demagnetisation effect resulting in the incoherent switching is proportional to thickness and is inversely proportional to the lateral dimensions of the junction. I note that there are large magnetic switching fields of around 2500 Oe, which favor the stability of the MRAM operation. The large magnetic switching fields, however, may lead to large current needed for the switching of the junction. From the simulation result, it is useful for exploring the spin torque transfer or thermal assistant switching for future applications.

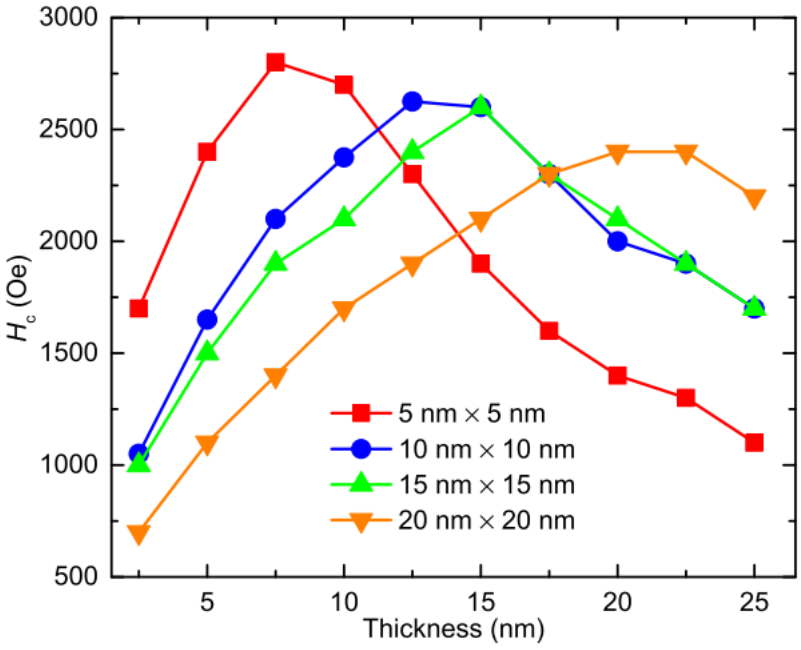

Figure 4. 10 The coercivity H_c, i.e., the switching field, as a function of the thickness for the junctions with different cross section sizes.

The side view in the y-direction of the junction device has been given in Figure 4.11-4. 13. The side view of different size of the junction device displays a same behaviour. As shown in Figure 4.6, the magnetisation in the different layer is almost the same.

From Figure 4.11 - 4. 13, the magnetisation in the x arm part is along to the x direction. The magnetisation in the cross part depends on the direction of x arm and y arm. In the other way, during the thickness of the device has increased, the perpendicular shape anisotropy also increases which will affect the H_c of the device.

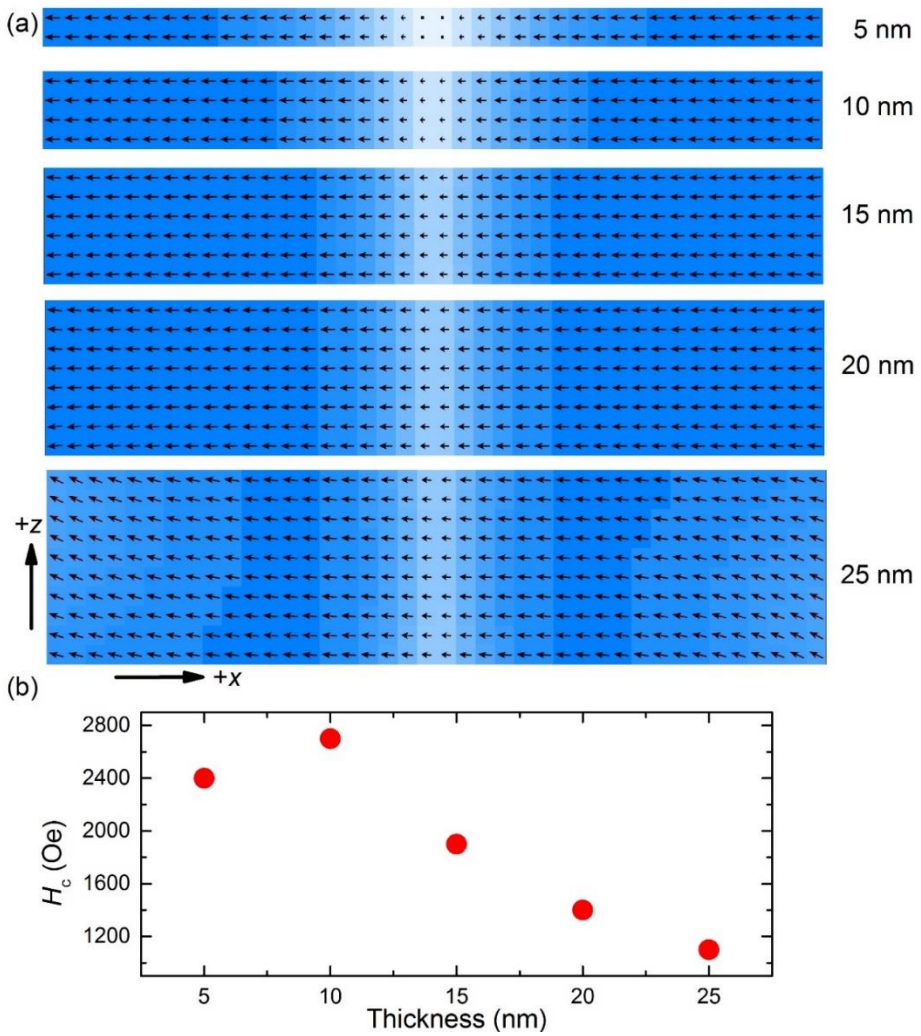

Figure 4.11 Side views of the magnetisation distribution of the 100 nm × 100 nm (arm length is 100 nm) junctions in the +*y* direction. (a) The thickness of the device is from 5 nm to 25 nm. (b) The coherence switching magnetic field as a function of the device thickness.

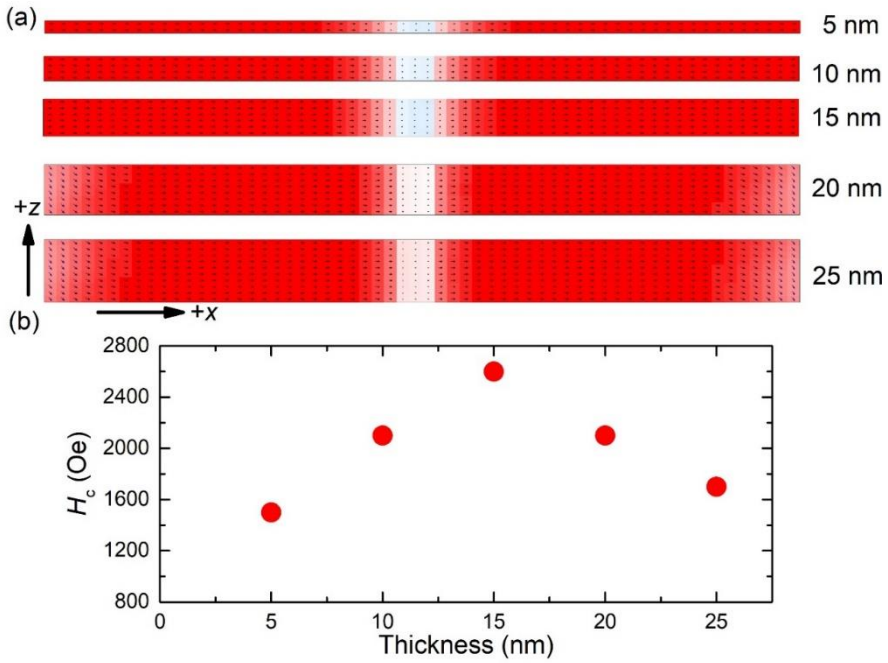

Figure 4.12 Side views of the magnetisation distribution of the 300 nm × 300 nm (arm length is 300 nm) junctions. (a) The thickness of the device is from 5 nm to 25 nm. (b) The coherence switching magnetic field as a function of the device thickness.

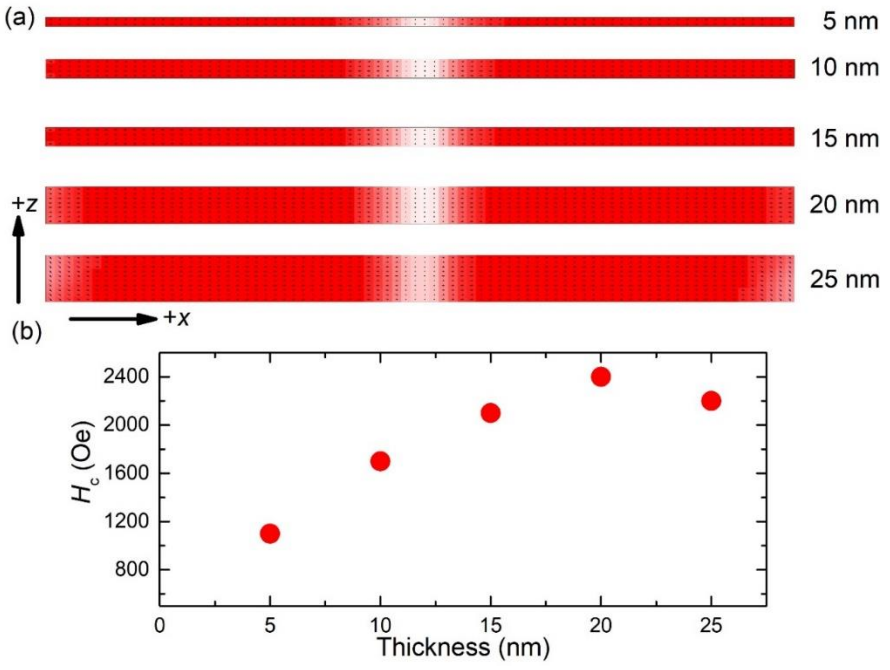

Figure 4.13 Side views of the magnetisation distribution of the 400 nm × 400 nm (arm length is 400 nm) junctions. (a) The thickness of the device is from 5 nm to 25 nm. (b) The coherence switching magnetic field as a function of the device thickness.

4. 9 Conclusion

In conclusion, I have carried out a full micromagnetic study on the magnetisation configuration and the magnetic switching process in a nanoscale Permalloy junction. The relationship between the magnetic switching fields and the thickness of the nanoscale junction has been investigated. While different types of domain walls can be formed in the initially relaxed states depending on the specific thicknesses, the junction acts as a single CSB where the spins are aligned in parallel during the magnetisation process. The magnetisation direction can be controlled and switched coherently by applying an external magnetic field. Both the initial magnetisation field and the coercivity are found to depend on the thickness, and the large coercivity could enhance the stability of the device operation. My work shows that the different states of nanoscale magnetic junction have the potential to be used as a building block for future spin-based data storage or logic computing technologies.

Chapter.5 Controllable transport of a skyrmion in a ferromagnetic narrow channel with voltage-controlled magnetic anisotropy

Magnetic skyrmions have potential applications in next-generation spintronics devices with ultralow energy consumption. In this work, the current-driven skyrmion motion in a narrow ferromagnetic nano-track with voltage-controlled magnetic anisotropy (VCMA) is studied numerically. By utilising the VCMA effect, the transport of skyrmion can be unidirectional in the nano-track, leading to a one-way information channel. The trajectory of the skyrmion can also be modulated by periodically located VCMA gates, which protects the skyrmion from destruction by touching the track edge. In addition, the location of the skyrmion can be controlled by adjusting the driving pulse length in the presence of the VCMA effect. My results provide guidelines for practical realization of the skyrmion-based information channel, diode, and skyrmion-based electronic devices such as racetrack memory.

5. 1 Introduction

Magnetic skyrmions are nanoscale particle-like topological configurations, which have been found in certain magnetic bulk materials, films and nanowire [39, 46, 48, 89-93]. The skyrmion is stabilized by delicate competitions among the ferromagnetic exchange coupling, perpendicular magnetic anisotropy (PMA) and Dzyaloshinskii–Moriya interaction (DMI) in magnetic systems [25, 31, 40, 94-97]. Magnetic skyrmions are expected to be used as information carriers in the next-generation spintronics devices due to their low-power consumption and small sizes [25, 27, 36, 98-106]. The skyrmion can be driven by the spin polarized current and spin-Hall torque and are

investigated widely[27, 102-104, 107]. The external effects on the velocity and trajectory of the skyrmion in nanodevice are also reported [108].

The skyrmion Hall effect (SkHE) is one of the most significant obstacles to the high-speed transmission of skyrmions in confined geometries. The SkHE has been theoretically predicted previously and has been observed experimentally [53, 54, 57]. The SkHE is caused by the Magnus force acting on the transporting skyrmion with a topological number of $Q = \pm 1$. The SkHE display a detrimental effect which makes the skyrmion deviate from the desired transmission path. One promising approach is to modulate the magnetic anisotropy in skyrmion racetrack memory and avoid skyrmion destruction at the edge of nano-track [108-110].

In this section, I report the dynamics of a skyrmion in a narrow ferromagnetic nano-track channel with voltage-controlled perpendicular magnetic anisotropy (VCMA), which can be used to build the skyrmion diode and ratchet memory [111, 112] and avoid from the SkHE. The pinning and depinning of the magnetic skyrmion in the nano-track through the VCMA gate are investigated. This work will be useful for the design and development of the skyrmion transport channel, which is a building block for any future skyrmion-based information devices.

5. 2 Modelling and simulation

The simulation model is an ultrathin ferromagnetic nano-track, 1000 nm × 80 nm × 0.4 nm, as shown in Figure 5.1(a). The model is discretized into tetragonal volume elements with the size of 2 nm × 2 nm × 0.4 nm. The micromagnetic simulations are performed with the Object Oriented Micromagnetic Framework (OOMMF) [36] [63]. The dynamics of magnetisation are described by Landau–Lifshitz–Gilbert LLG (LLG) equation, written as

$$\frac{dm}{dt} = -\gamma_0 m \times h_{eff} + \alpha\left(m \times \frac{dm}{dt}\right) - um \times (m \times p), \qquad (5.1)$$

where m is the reduced magnetisation $\frac{M}{M_S}$, M_S is the saturation magnetisation. γ_0 is the gyromagnetic ratio and α is the damping coefficient. h_{eff} is the effective field including the contributions of Heisenberg exchange, Dzyaloshinskii– Moriya interaction (DMI), magnetic anisotropy and demagnetisation field. The u can be defined as $\frac{\gamma_0 hjP}{2de\mu_0 M_S}$, h is the reduced Plank constant, j is the current density, $P = 0.08$ is the spin Hall angle, a is the atomic lattice constant, e is the electron charge, μ0 is the vacuum permeability constant, d is the thickness of the magnetic nano-track [113]. p is the direction of the spin polarization which is equal to $-\hat{y}$. The parameters for the micromagnetic simulation are adopted from [24]: the saturation magnetisation M_S = 580 kA m^{-1}, the damping coefficient $\alpha = 0.3$, the DMI constant D = 3 mJ m^{-2} , and the exchange constant A = 15 pJ m^{-1} . In the simulation, the profile of the voltage-controlled magnetic anisotropy (VCMA) in the nano-track are shown in Figures 5.1(b)–(d). For the simulation of the pinning/depinning states of the skyrmion, the PMA profile is shown in Figures 5.1 (b). VCMA linearly varies from K_{u0} to K_{uv} and material uniaxial anisotropy K_{u0} = 0.8 MJ m^{-3}. For the simulation of the motion of skyrmion, two types of VCMA profile are considered, period wedge-shape and sinusoidal functions, as shown in figures 1(c) and (d), respectively. The function for the period wedge-shape profile is given as:

$$K_u(x) = K_{u0} + \frac{Kuv - Ku0}{w}x, \tag{5.2}$$

$$K_u(x) = K_{u0} + \frac{K_{uv} - K_{u0}}{2}(1 + sin\ (2\pi x/w - \varphi)), \tag{5.3}$$

where w is the period length, φ is the phase, and x is the longitudinal coordinate. The period wedge-shape is given in the Equation 5.2 and the sinusoidal function is given in

the Equation 5.3. The linear anisotropy profile and the sinusoidal function profile are given in Figures 5.1(b) and (c).

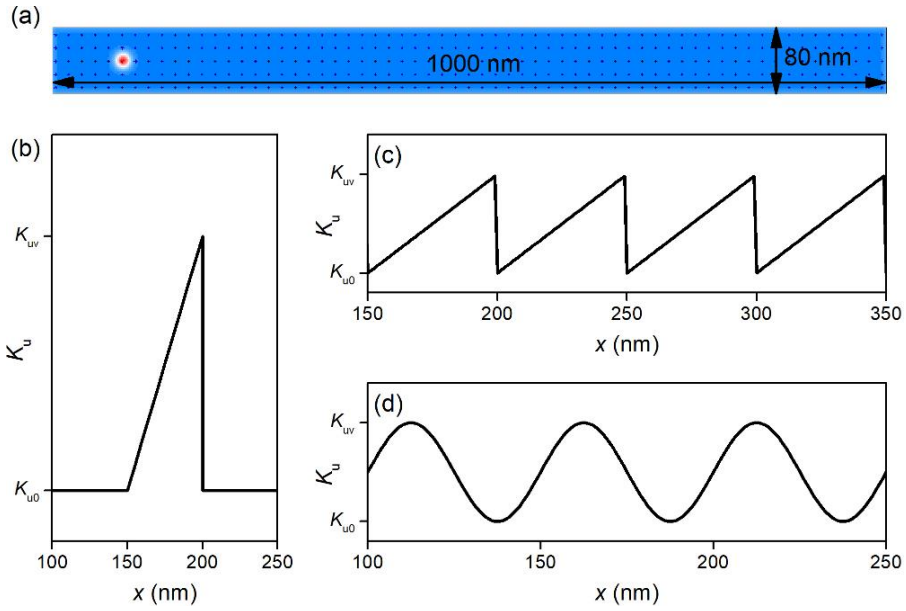

Figure 5.1(a) A Schematic of the magnetic nano-track where a magnetic skyrmion is initially placed. The out-of-plane magnetisation component is represented by the red (−z)-white (0)-blue (+z) color scale. (b) A linear anisotropy profile. (c) A periodical repetition of a linear anisotropy profile with a period w. (d) Sinusoidal function of x with a period *w*.

5. 3 The pinning/depinning states of isolate skyrmion in nano-track

Figure 5.2. shows the pinning/depinning states of isolate skyrmion driven by the spin current in a nano-track with the PMA profile shown in Figure 5.1. (b). Figure 5.2. (a) and (b) show the effect of the width and the current density on the pinning/ depinning states.

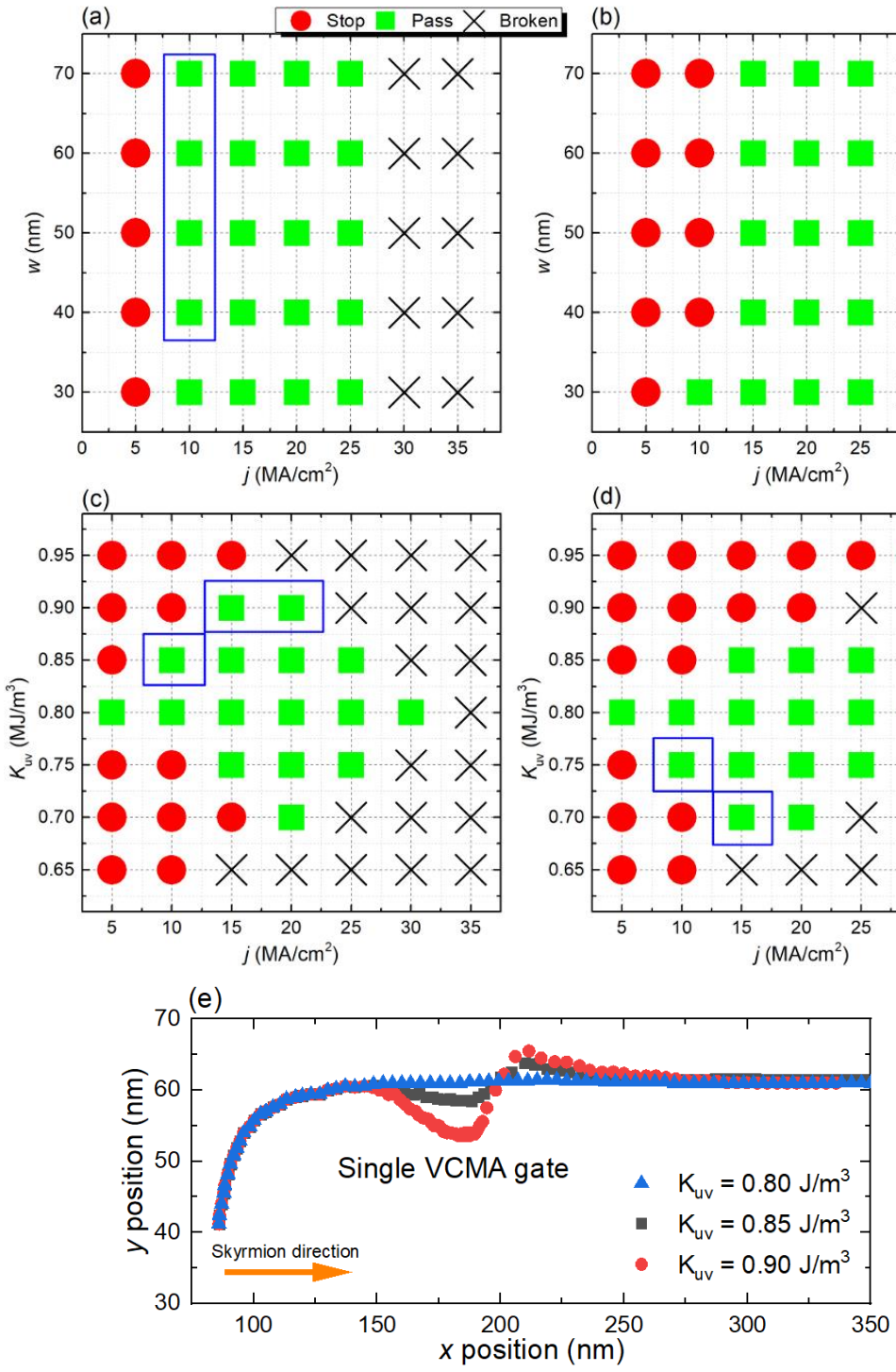

Figure 5.2 The pinning/depinning states of an isolate skyrmion driven by the current in a magnetic track. (a), (b) The pinning/depinning states of a skyrmion at various width w and driving current *j* along +*x* and −*x* axis for K_{uv} = 0.85 MJ m^{-3} , respectively. (c), (d) The pinning/depinning states of a skyrmion at various K_{uv} and *j* along +*x* and −*x* axis for the fixed w = 50 nm, respectively. (e) The trajectories of the skyrmion in the nano-track with *j* = 1.5

MA/cm^2 and K_{uv} from 0.80 MJ m^{-3} to 0.90 MJ m^{-3}. The solid circle means the skyrmion is not able to pass the well or barrier, the solid square means the skyrmion can pass the well or barrier and the cross means the skyrmion is destroyed.

Initially, the relaxed skyrmion is located at the left side of the VCMA region when the spin current is applied along $+x$ axis. The skyrmion is not able to pass the VCMA region when the current density is smaller than 10 MA cm^{-2} and pass the VCMA region when 25 MA cm^{-2} $< j <$ 30 MA cm^{-2} . The skyrmion will be destroyed when the current is larger than 30 MA cm^{-2} . When the spin current is applied along −x axis, the skyrmion is located at the right side of the VCMA region. Most states are the same to the corresponding results in Figure 5. 1(a), except for the case of j = 10 MA cm^{-2} . For j = 10 MA cm^{-2} and w > 30nm, the skyrmion can pass the VCMA region when the current is applied along +x axis while it cannot pass when the current is applied along −x axis. It means that the skyrmion can pass only in one direction, +x axis. The motion of skyrmion is unidirectional. The parameters corresponding to the unidirectional pass along +x axis are marked with blue box in Figure 5.2. (a). Figure 5.2. (c) and (d) show the effect of the VCMA and the current density on the pinning/depinning states. Our results show that the states are sensitive to the VCMA. The unidirectional behaviours also can be found. The parameters for the unidirectional pass along +x axis are marked with a blue box in Figure 5.2. (c) and these for the unidirectional pass along −x axis are marked with a blue box in Figure 5.2. (d). The unidirectional behaviours show that the voltage gate can be used to build skyrmion diode. In Figure.5.2(e), the trajectories of the skyrmion in the nano-track with j = 1.5 MA/cm^2 and K_{uv} from 0.80 MJ m^{-3} to 0.90 MJ m^{-3} has been demonstrated. When $K_{uv} > K_u$, the VCMA region will reduce the velocity of skyrmion which influences the skyrmion Hall effect. The discussion of skyrmion velocity will be given in Section 5.4.

5. 4 The deformation of skyrmion due to the variation of PMA

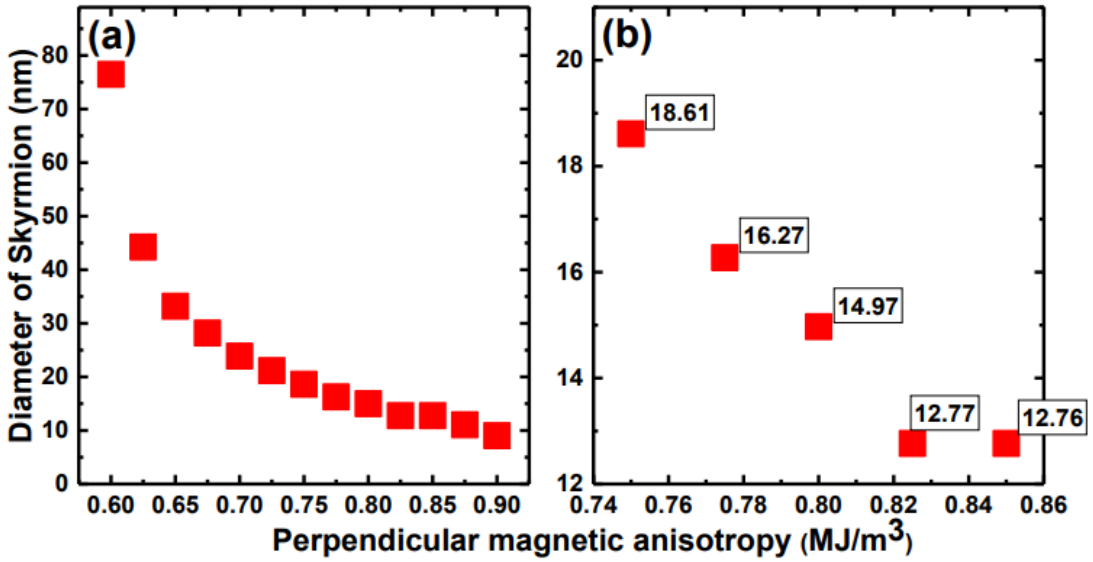

Figure 5.3 The relationship between the size of the skyrmion and the magnetic anisotropy constant. The model is an ultrathin ferromagnetic dot with diameter 100 nm and thickness 0.4 nm. The model is discretized into cuboidal volume elements with the size of 1 nm * 1 nm * 0.4 nm. (a) The PMA ranges from 0.60 MJ/m^3 to 0.90 MJ/m^3. (b) The PMA range from 0.75 MJ/m^3 to 0.85 MJ/m^3 which is used in simulation in the section.

In Figure 5.3., the diameter of the skyrmion is inversely proportional to the magnetic anisotropy constant. When the magnetic anisotropy is increasing from 0.60 MJ/m^3 to 0.70MJ/m^3, the diameter of the skyrmion decreases rapidly. When the magnetic anisotropy is larger than 0.70 MJ/m^3, the diameter of the skyrmion reduces more slowly. The PMA range is from 0.75 MJ/m^3 to 0.85 MJ/m^3. The exact skyrmion diameter reduces from 18.61 nm to 12.76 nm and when the PMA larger than 0.825 MJ/m^3 the skyrmion size only decrease a little.

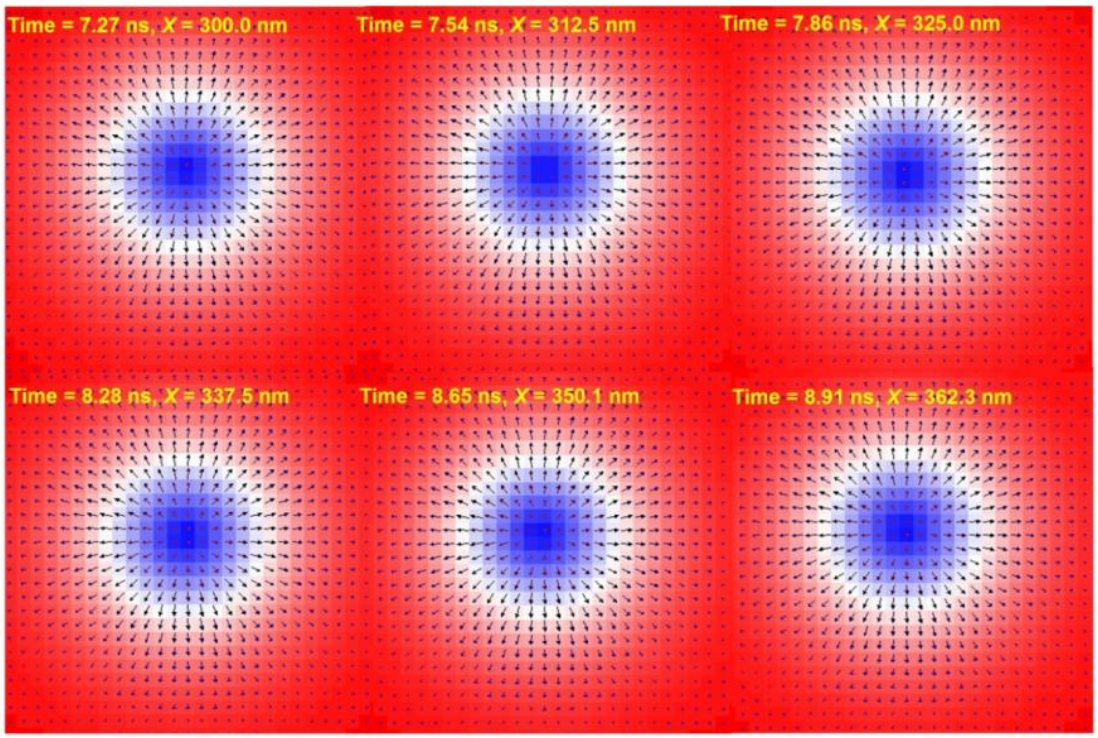

Figure 5.4 The top-view of the skyrmion motion in a nano-track with slope-shaped VCMA gate profile. The slope-shaped VCMA gate profile with a PMA changes from 0.80 MJ/m^3 to 0.85MJ/m^3 depends on the x axis position. The simulation time and the x axis position of the skyrmion motion in the nano-track are given.

The relationship between the size of skyrmion and the perpendicular magnetic anisotropy is given in Figure 5.4. which shows the diameter of the skyrmion will reduce slowly when the magnetic anisotropy increases from 0.80 MJ/m^3 to 0.85 MJ/m^3.(The different x postion cause a different anisotropy strength) In Figure. 5.3, the shape variation and size variation of the skyrmion is not very obviously.

5. 5 Skyrmion motion with the spatially dependence of VCMA gate

The skyrmion motion driven by the spin current in a magnetic nano-track with the spatially dependence of VCMA is simulated. In this section, the VCMA modulation skyrmion trajectory in a nanotrack has been studied. The VCMA is periodical repetition of a wedge-shape profile, as shown in Figure 5.5. (a) ($K_{uv} > K_{u0}$) and (b) ($K_{uv} < K_{u0}$). Initially, the relaxed skyrmion is located at x = 86 nm and y = 40 nm. The trajectories of the skyrmion driven by the spin current (j = 15 MA cm^{-2}) in the nano-track with various K_{uv} shown in Figure 5.5. (c). For K_{uv} = 0.800 MJ m^{-3} , a uniform perpendicular magnetic anisotropy in the nano-track, the skyrmion shows a transverse motion towards to the upper edge resulted by the transverse force due to skyrmion Hall effect (SkHE) firstly [53]. When the skyrmion motion in a nanotrack, the SkHE will give the skyrmion a y direction velocity which induced by the Magnus force. When the transverse force and edge-skyrmion repulsive force are balanced, the skyrmion moves linearly [96, 97, 102]. It can be seen that the skyrmion moves linearly at y = 60nm finally. For K_{uv} = 0.850 MJ m^{-3}, the skyrmion moves in a periodic trajectory with an equilibrium position at y = 60.6 nm. Similar behaviours of the skyrmion are found when K_{uv} = 0.750 MJ m^{-3}, 0.775 MJ m^{-3}, and 0.825 MJ m^{-3}. It can be found that the equilibrium position increases with increasing K_{uv}, which is shown in Figure 5.5. (e). Periodic trajectories and similar dependence of the equilibrium position on K_{uv} can be also found in the case of j = 20 MA cm^{-2}, as shown in Figure 5.5. (d). The equilibrium positions of the periodical wavy trajectories are larger compared to the case of j = 15 MA cm^{-2}.

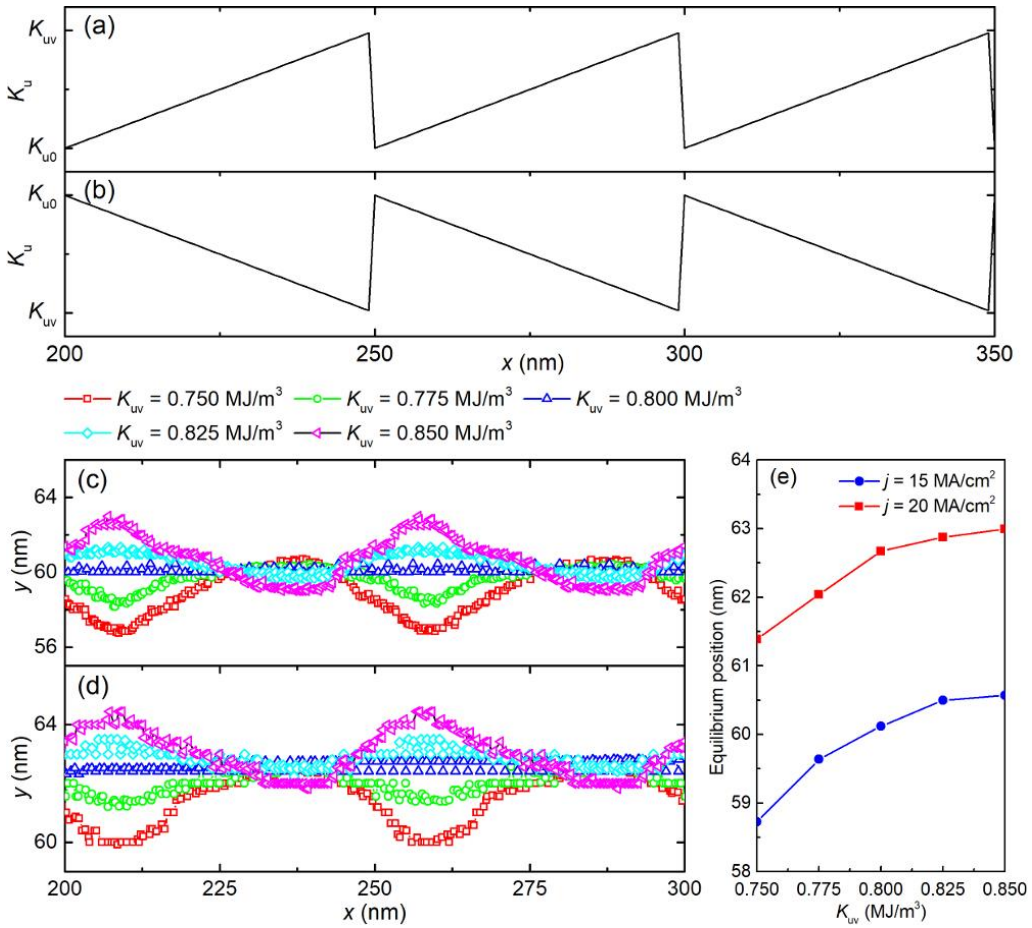

Figure 5.5(a) The wedge-shaped profile of Ku for $K_{uv} > K_{u0}$. (b) The wedge-shaped profile of K_u for $K_{uv} < K_{u0}$. (c) The trajectories of the skyrmion in the nano-track with various K_{uv} for j = 15 MA cm^{-2}. (d) The trajectories of the skyrmion in the nano-track with various K_{uv} for j = 20 MA cm^{-2}. (e) The equilibrium position of the skyrmion in the y-direction for (b) and (c). The spin current is applied along +x axis.

Figure 5. 6. shows the trajectories of the skyrmion in a nano-track with sinusoidal dependence of K_u on the position x. The profile of K_u is shown in Figure 5.5(a). K_{u0} is the minimum and K_{uv} is the maximum. It can be found in Figure 5.5(b) that the skyrmion moves in a sinusoidal trajectory when $K_{uv} \neq 0.8$ MJ m^{-3}. Opposed to the case of the wedge-shaped profile of K_u, the equilibrium positions in the y-direction for various K_{uv} are almost the same, y = 60 nm. When the current density increases to j = 20 MA cm^{-2}, similar results can be found. Furthermore, the effect of the phase has also been simulated and the results are shown in Figure 5. 6.

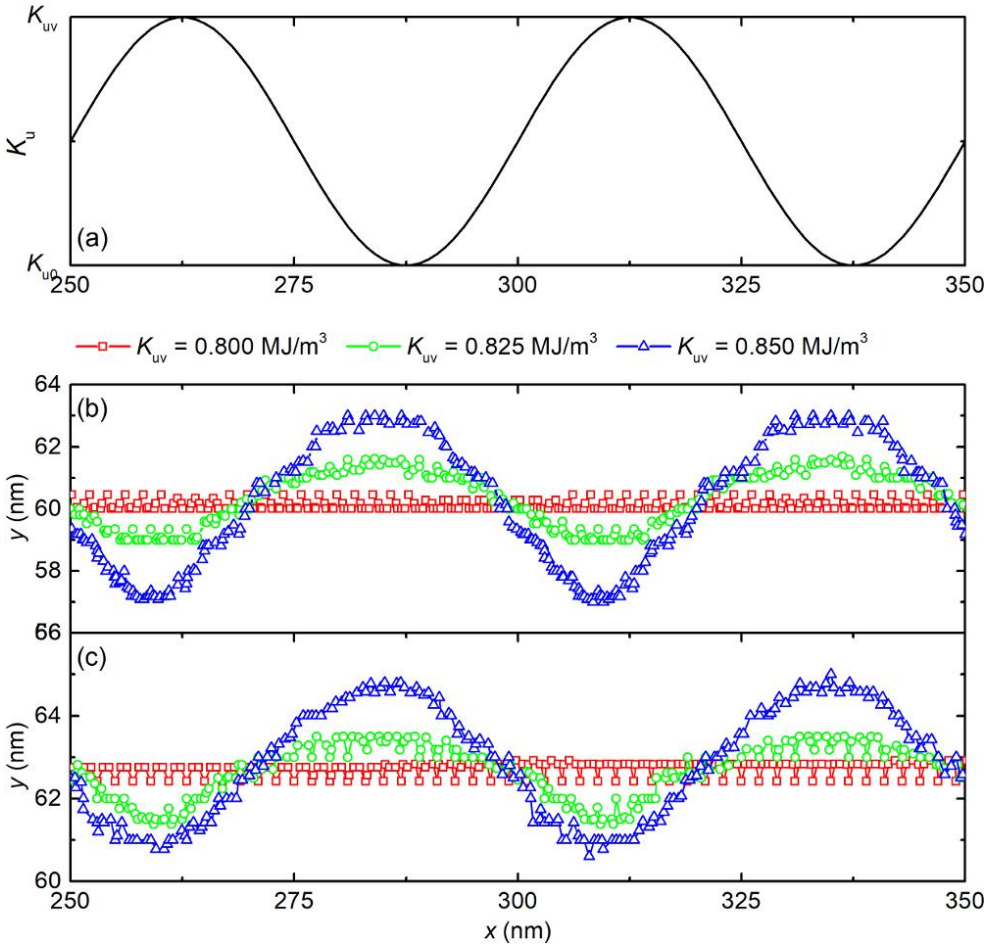

Figure 5.6 (a) The profile of K_u as a sinusoidal function of x. (b) The trajectories of the skyrmion in the nano-track with various K_{uv} for j = 15 MA cm^{-2}. (c) The trajectories of the skyrmion in the nano-track with various K_u for j = 20 MA cm^{-2}. The spin current is applied along +x axis.

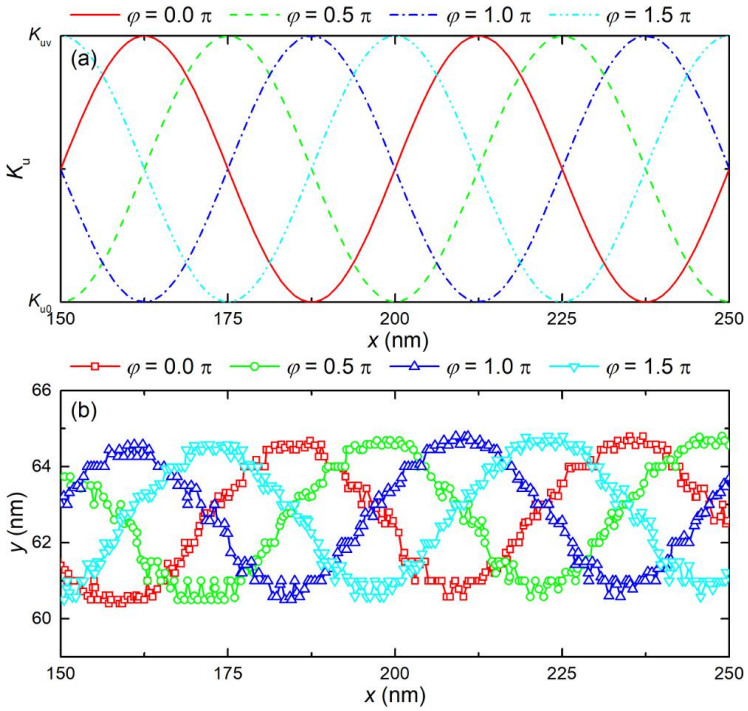

Figure 5.7 (a) The profile of K_u and (b) the corresponding trajectories of the skyrmion in the nano-track with ϕ = 0, 0.5π, 1.0π, 1.5π. The driving current density is 20 MA cm^{-2} applied along +x axis and K_{uv} = 0.850 MJ m^{-3}.

As shown in Figure 5.3., the variation of anisotropy constant will influence the size of skyrmion. The diameter of the skyrmion is inversely proportional to the anisotropy. When K_{uv} = 0.75 MJ m^{-3}, the diameter of skyrmion is 18.61 nm and decreases to 14.97 nm when K_{uv} increases to 0.80 MJ m^{-3}. The top-views of the skyrmion have been given in Figure 5.3. The skyrmion size as a function of position when the skyrmion moves in the nanowire with different shape profiles are given in Figure 5. 8.

In Figure 5. 8, the skyrmion size increases when the skyrmion moves in a nano-track with increasing PMA. Due to the Magnus force, when the skyrmion is driven by the vertical spin current, there is a transverse displacement, leading to the skyrmion moving along the upper edge of the nano-track [30]. Then, the skyrmion size decreases since both repulsion force and Magnus force increase. When the skyrmion moves in the nano-track with increasing PMA, the velocity decreases, leading to the Magnus force exerted

on the skyrmion decreases. The skyrmion is pushed toward the center of the nano-track. Both Magnus force and the repulsion decrease, which results in the skyrmion size increasing. In Figure 5. 5-7, the skyrmion has a transversal motion in the y-direction which is influenced by Magnus force and edge force.

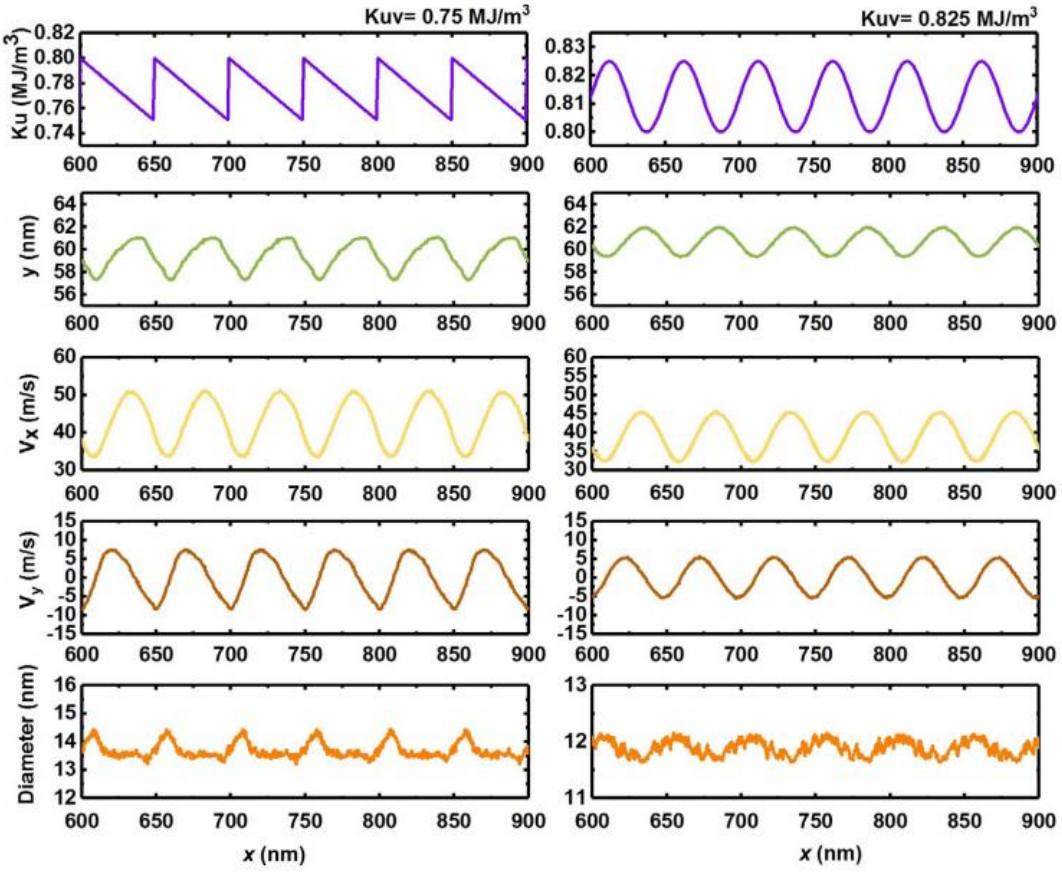

Figure 5.8 Movement of skyrmion in nano-track with slope profile and sinusoidal profile. The K_{uv} of the wedge-shaped profile is 0.75 MJ m^{-3} and for the sinusoidal profile is 0.825 MJ m^{-3}. The driving current density is j = 15 MA cm^{-2}. The K_{uv} profile, trajectory, skyrmion velocity in the x direction, skyrmion velocity in the y direction and diameter of the skyrmion are given in Figure

The Magnus force (SkHE) drives the skyrmion from the center of the nanowire to the edge and depressed by the force between the moments at the edge of the nano-track. The Magnus force in the y component is dependent on the velocity of the skyrmion in x-direction [114] and the velocity of skyrmion motion in x axis v_x and y axis v_y are

given in Figure 5.8. When the skyrmion moves to a place with a lower magnetic anisotropy, the velocity of skyrmion in x-direction increases and the Magnus force in y component increases. The skyrmion will be driven to the edge until the Magnus force and the edge force (comes from the demagnetization field) are in balance. When the skyrmion moves in a nanowire with increasing magnetic anisotropy, the velocity of skyrmion decreases and the skyrmion reduces to the center of the nanowire. This phenomenon shows the nanowire with VCMA gate can avoid the skyrmion destroy at the edge.

5. 6 Skyrmion motion driven by current pulse in nano-track with VCMA gate

The motion of the magnetic skyrmion in the nano-track with VCMA driven by the current pulse is also simulated. The initial position the skyrmion is x = 86 nm which is the middle of a voltage gate. Figure 5. 9. shows the motion of the skyrmion in the nano-track with a periodical wedge-shaped profile with K_{uv} = 0.750 MJ m^{-3} with the period length w = 50 nm. The current density of the pulse is 20 MA cm^{-2}. The pulse is applied at t = 0.5 ns. For one period of the current pulse, t_e is the time interval applying the current and tr is the relaxation time without applying current. t_r = 5 ns in the simulations. When t_e = 1 ns, the skyrmion cannot pass the voltage gate and moves in a circle trajectory as shown in Figure 5. 9. (a) and (b). For t_e = 2 ns, the trajectory of the skyrmion is shown in Figure 5. 9. (c). The time-dependence of the position in the x-direction and the current density are shown in Figure 5. 9. (d). At t = 14.5 ns, the skyrmion is located at x = 187 nm. After applying the pulse, x = 241 nm at t = 16.5 ns. Then the applied current is off. The skyrmion further relaxes to x = 236 nm before the next pulse. The displacement of skyrmion is 50 nm after a pulse is applied. For t_e = 3

ns, Figure 5. 9. (e) and (f), one current pulse results in a displacement of 100 nm.

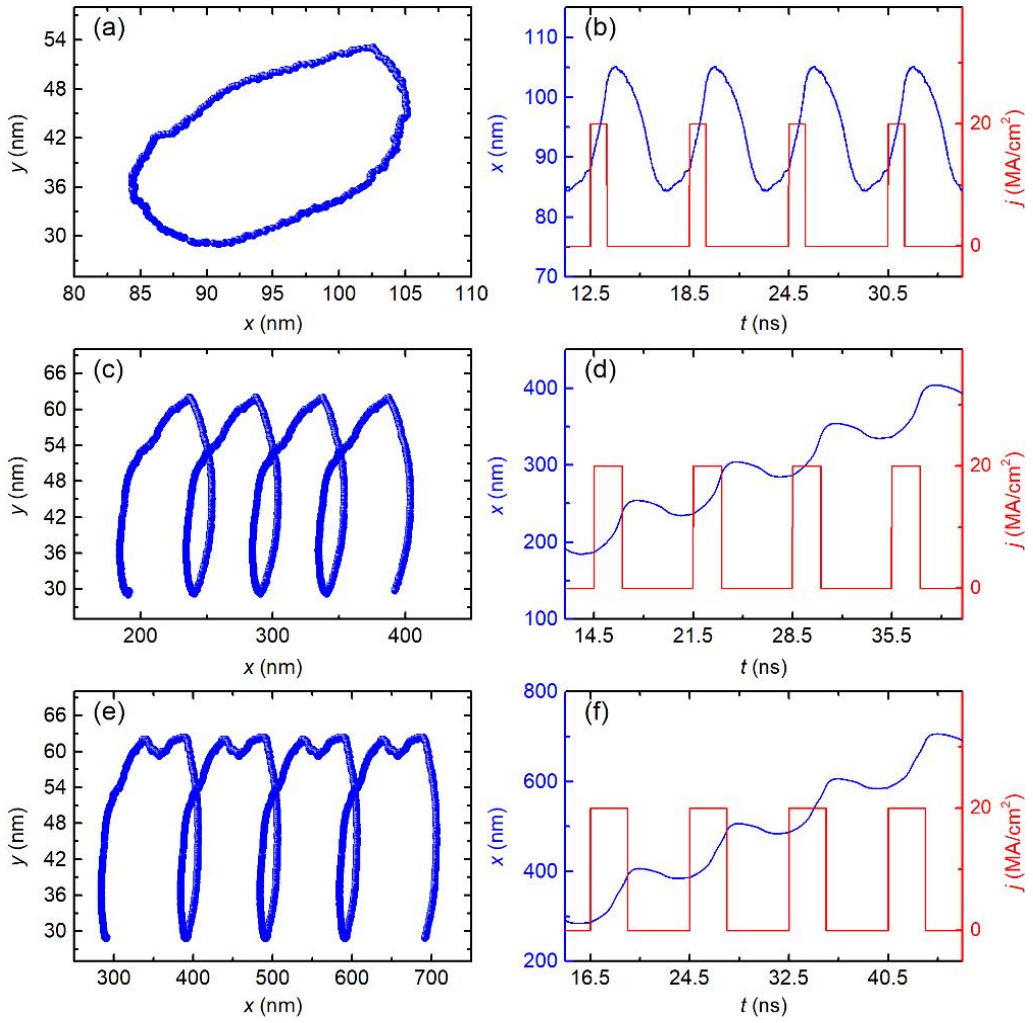

Figure 5.9 The skyrmion motion driven by the current pulse in the nano-track with the wedge-shaped K_u with K_{uv} = 0.75 MJ m^{-3}. The left panel shows the trajectories of the skyrmion. The right panel shows the x position of the skyrmion and the current density as functions of time t. For one period of the current pulse, t_e is the pulse time and tr is the relax time without applying current. t_r = 5 ns in the simulations. (a) and (b) t_e = 1 ns. (c) and (d) t_e = 2 ns. (c) and (d) t_e = 3 ns.

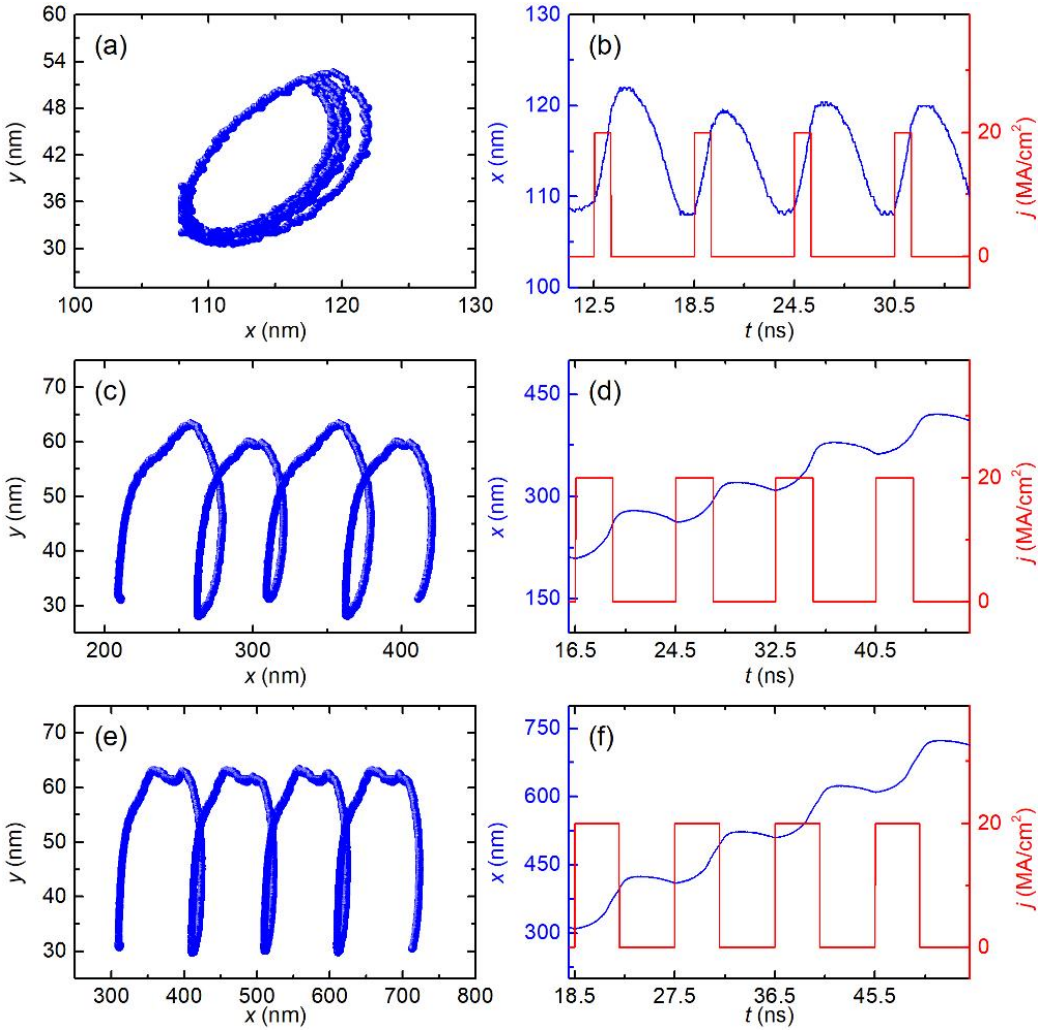

Figure 5.10 The skyrmion motion driven by the current pulse for the wedge-shaped K_u with K_{uv} = 0.85 MJ m^{-3}. The left panel shows the trajectories of the skyrmion. The right panel shows the x position of the skyrmion and the current as functions of time t. t_r = 5 ns in the simulations. (a) and (b) t_e = 1 ns. (c) and (d) t_e = 3 ns. (c) and (d) t_e = 4 ns.

Figure 5.10. shows the results for the case of wedge-shaped K_{uv} with K_{uv} = 0.850 MJ m^{-3} and the period length w = 50 nm. The current density of the pulse is 20 MA cm−2 and the pulse is applied at t = 0.5 ns with t_r = 5 ns. In Figure 5.10. (a) and (b), compared with the state with K_{uv} = 0.750 MJ m^{-3} , the skyrmion can more easily pass the voltage gate. This state also has been explained in Figure 5.2. (c). The skyrmion passes the first voltage gate and cannot pass the second voltage gate. Then the skyrmion moves in a circular trajectory. When the t_e = 2 ns and 3 ns, the states is similar as Figure 5.9. (c)–

(f). The skyrmion passes one or two voltage gates are shown in Figure 5.10. (c)–(f). In Figure 5.10. (c) and (d), for nanoscal$_e$ = 2 ns, the skyrmion is located at x = 212 nm when t = 16.5 ns. After applying the pulse, skyrmion moves to x = 277 nm. When the current is off, the skyrmion further relaxes to x = 263 nm before the next pulse. The displacement of skyrmion is 50nm after a pulse is applied. For t_e = 3 ns, as shown in Figure 5.10. (e) and (f), one current pulse leads to a displacement of 100 nm.

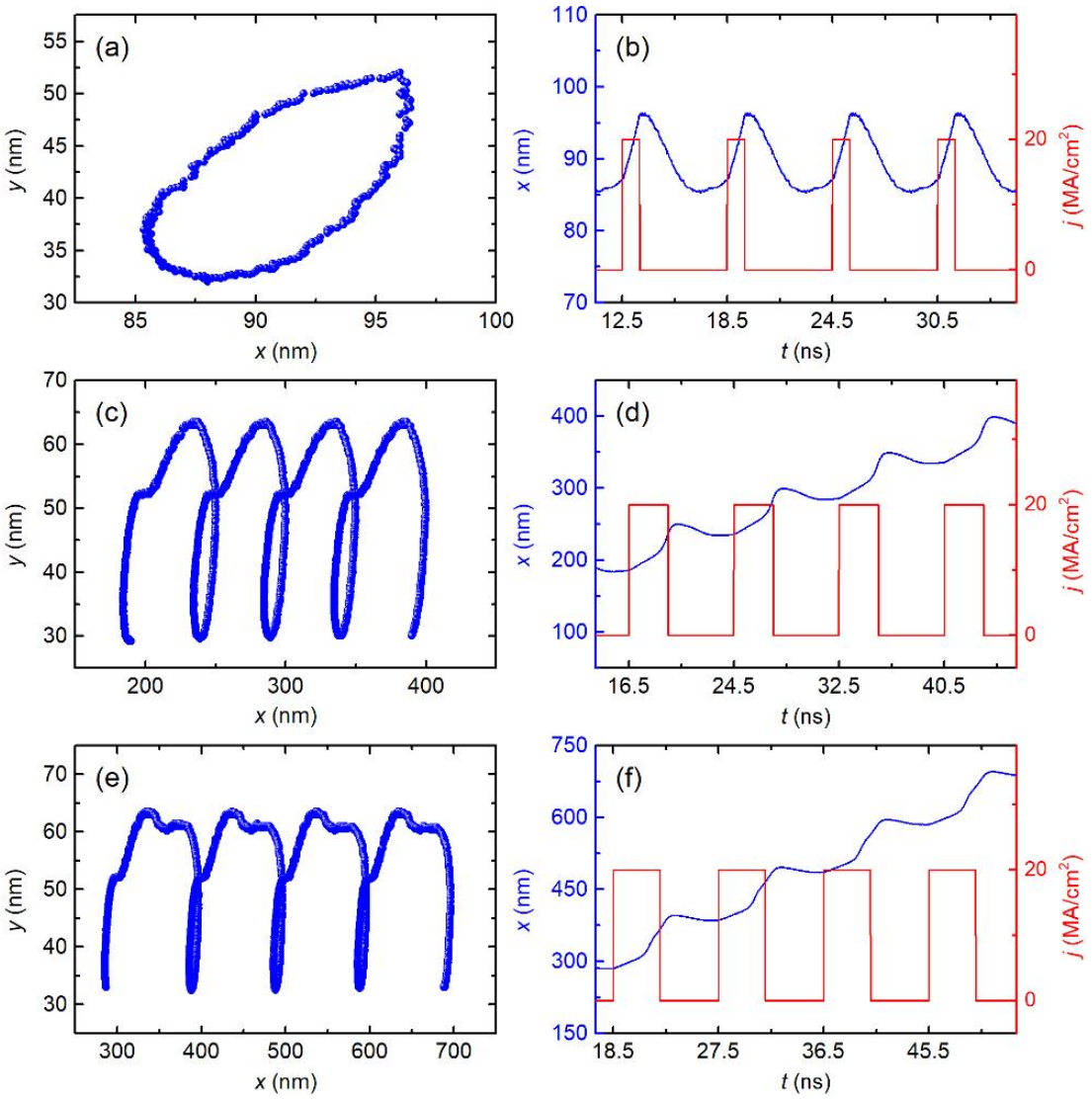

Figure 5.11 The skyrmion motion driven by the current pulse for the sinusoidal K_u with K_{uv} = 0.85 MJ m^{-3} and ϕ = 0. The left panel shows the trajectories of the skyrmion. The right panel shows the x position of the skyrmion and the current as functions of time. t_r = 5 nm in the simulations. (a) and (b) t_e = 1 ns. (c) and (d) t_e = 3 ns. (c) and (d) t_e = 4 ns.

Figure 5.11. shows the motion of the skyrmion in the nano-track with a sinusoidal function profile with K_{uv} = 0.850 MJ m^{-3} with the period length w = 50nm. The trajectories of skyrmion with t_e = 1 ns are shown in Figure 5.11. (a) and (b). The skyrmion cannot pass the voltage gate and moves in a circle which is like Figure 5.11. (a) and (b). For t_e = 2 ns, the trajectory of the skyrmion is shown in Figure 5.11. (c). The time dependence of the position in the x-direction and the current density are shown in figure 9(d). At t = 16.5 ns, the skyrmion is located at x = 186 nm. After applying the pulse, x = 236 nm at t = 18.5 ns. Then the applied current is off. The skyrmion further relaxes to x = 234 nm before the next pulse. The skyrmion moves with a pulse time t_e = 3 ns which is shown in Figure 5.11. (e) and (f) shows that one current pulse results in a displacement of 100nm. From Figure 5. 9 to 5 .11, it can be seen that the model with multiple voltage gates can be used to realize high-density racetrack memory device. The VCMA region can lock the skyrmion in each memory unit, and the current pulse can be driven the skyrmion from one memory unit to another memory unit.

5. 7 Conclusion

In this chapter, the skyrmion motion in a ferromagnetic nano-track with single or multiple VCMA gates is studied. This work shows that the trajectory and location of the skyrmion can be controlled by periodically located VCMA gates as well as the driving current pulse. The unidirectional motion of the skyrmion realized by the VCMA effect can be used to build the skyrmion-based one-way information channel and the skyrmion diode. My results are useful for the design and development of the skyrmion-based spintronics devices.

Chapter.6 Skyrmionium dynamics in a nano-track with voltage control anisotropy

The magnetic skyrmionium is a doughnut-like soliton, which has potential application in the next-generation spintronics devices. The skyrmionoum can be seen as a coalition of two magnetic skyrmions and can be driven by the smaller current density. In this work, I report the skyrmionium dynamics in a nano-track with voltage-controlled perpendicular magnetic anisotropy (VCMA). The pinning and depinning of the magnetic skyrmionium in the nano-track through the voltage gate are investigated. The skyrmionium displays diode effect when the nano-track with a slope-shape voltage gate. In addition, the skyrmion motion in nano-track driven by anisotropy gradient has been demonstrated and the result provides a useful guideline for building the voltage control skyrmionium based device.

6. 1 Introduction

Recently, the generation and dynamics of the magnetic skyrmions have been widely investigated [39, 40, 45, 46, 89]. This kind of nanoscale particle-like topological configuration can be found in certain magnetic bulks and films [115-118]. The skyrmion can be stabilized by the ferromagnetic exchange coupling, perpendicular magnetic anisotropy (PMA) and Dzyaloshinskii-Moriya interaction (DMI) in magnetic systems [31, 97]. One of the most prominent approaches of the magnetic skyrmion is used as information carriers in the nanoscale spintronics device [50, 103, 119]. The

skyrmion in the nanoscale devices can be driven by the spin polarized current, spin hall torque and spin waves [120-122]. The Skyrmion Hall Effect (SkHE) is a significant obstacle to the transmission of skyrmions in the nanoscale device. The SkHE was previously investigated theoretically and observed experimentally [53, 57]. The SkHE is caused by the Magnus force acting on the moving skyrmion with a topological number of $Q = \pm 1$ and may induce skyrmions to destroy at the edge of the device. The skyrmion Hall effect depends on the velocity of the skyrmion, which limits the velocity and stability of skyrmion in the device.

The promising approach to make the skyrmions avoid from the SkHE is to generate a magnetic topology structure with a $Q = 0$. The anti-ferromagnetic exchange bi-layer system with a $Q = 0$ and free from the SkHE has been reported [123]. In this system, the magnetic skyrmion in a different layer will have adverse Q. Between the layers, there is a robust antiferromagnetic coupling which makes the skyrmions in different layers couple with each other. The SkHE for the bi-layer skyrmion can be avoided because of the direction of SkHE in each layer is reversed and the Q for these two skyrmions is effectively 0.

On the other hand, a magnetic skyrmionium is also a $Q = 0$ topology structure which can be seen as the combination of two skyrmions with reverse Q value [124-126]. Magnetic skyrmionium has a doughnut shape structure which is stabilized by the DMI in the system. The magnetic skyrmionium can be generated by the ultrafast laser and can stable for over a few years which has been overserved experimentally which has been given in Figure 6.1 [126]. The skyrmionium has a smaller threshold current than a skyrmion and is free from the SkHE. The dynamics of skyrmionium in thin film and nanoscale device have been studied theoretically and observed by experiment which shows the potential function of the skyrmionium in next-generation spintronics device [127-129].

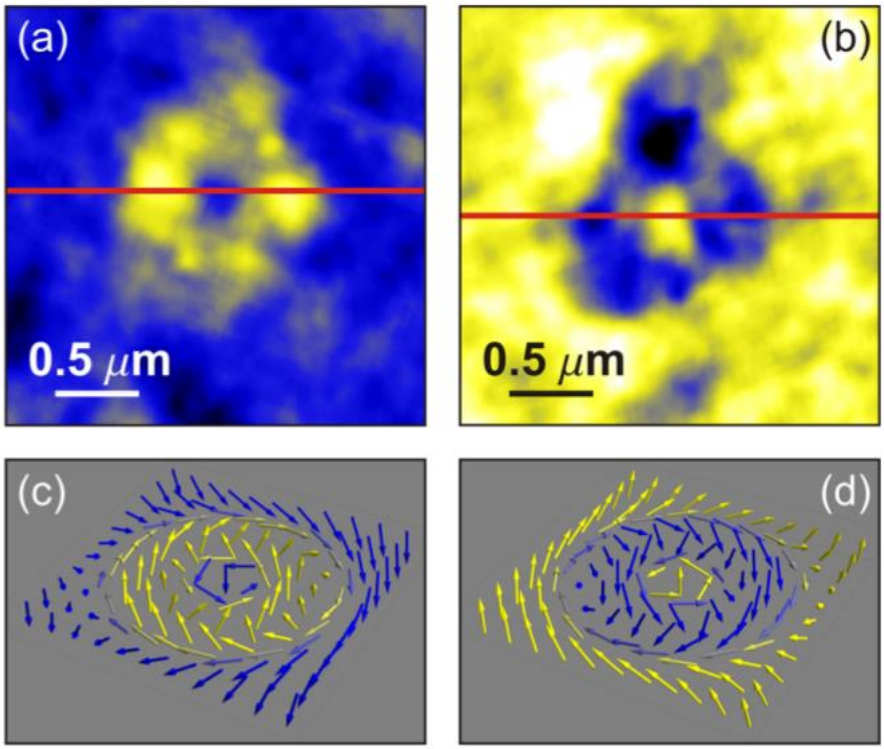

Figure 6.1 (a), (b) Near-field Faraday rotation maps showing "doughnut"-shaped magnetic domains after single laser pulse irradiation in film areas showing opposite out-of-plane magnetisations. (c),(d) Skyrmionium spin textures. Ref. [126]

In this chapter, I study the dynamics of skyrmionium in a nano-track with voltage control perpendicular magnetic anisotropy (VCMA) gate. The VCMA gate will enhance/decrease the magnetic anisotropy in part of the device. The voltage gate can be used to build the skyrmion/skyrmionium diode and ratchet memory which has been report recently [50, 98, 130]. In addition, I also studied the magnetic skyrmionium driven by the anisotropy energy gradient without a polarized current. The anisotropy gradient induces motion of the magnetic skyrmionium can make it avoid from the joule heat, which can enhance the stability and lifetime of magnetic skyrmionium. The results in this chapter will be useful for designing the high speed skyrmionium transport channel and skyrmionium diode.

6. 2 Modelling and simulation

The simulation model is an ultrathin ferromagnetic nano-track, 1000 nm×180 nm×0.4 nm, as shown in Figure 6. 2(a). The model is discretized into tetragonal volume elements with the size of 2 nm × 2 nm × 0.4 nm. The micromagnetic simulations are performed with the Object Oriented Micromagnetic Framework (OOMMF) [63]. The dynamics of magnetisation are described by Landau-Lifshitz -Gilbert LLG (LLG) equation.

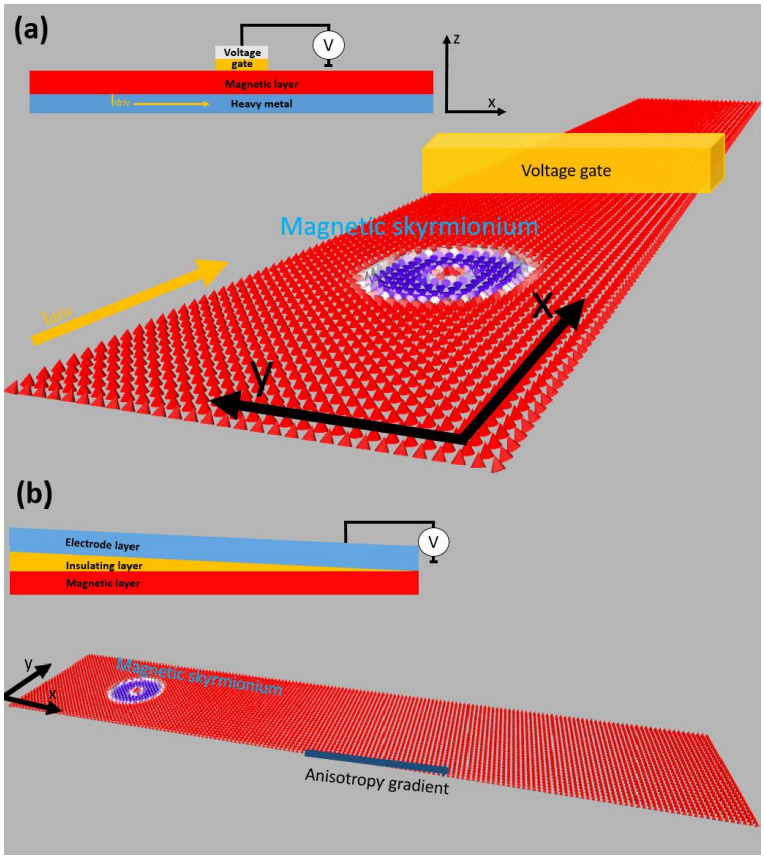

Figure 6.2 (a) Schematic configurations for the skyrmionium based device where a skyrmionium is initially placed. The out-of-plane magnetisation component is represented by the red(-*z*)-white(0)- blue(+*z*) color scale. (b) The skyrmionium driven by anisotropy energy gradient $F_{Gradient}$ without polarized current

The parameters for the micromagnetic simulation are adopted from Ref. [24]: the saturation magnetisation MS = 580 kA/m, the damping coefficient α = 0.3, the DMI constant D = 3.5 mJ/m^2, and the exchange constant A = 15 pJ/m. Comparing with the magnetic skyrmion, the magnetic skyrmionium require a higher DMI to keep the topological structure stable.

In the simulation, the profiles of voltage gate is given in Figure 6. 2(a), the K_{uv} varying according to the x axis. For the simulation of the pinning/depinning site the system can be modelled as a single wedge shape voltage gate in the middle of the nanowire. The varying magnetic anisotropy (K_{uv}) can be calculated by the longitudinal coordinate x and the uniform anisotropy Ku. The K_{uv} of the wedge profile can be formulated as

$$K_{uv} = K_u + (K_{uv} - K_u)x/w, \tag{3.3}$$

where w is the width of the voltage gate. The profiles of voltage gradient induce skyrmionium motion is given in Figure 6. 2 (b). The varying magnetic anisotropy (K_{uv}) change along the coordinate x and the whole system is without the polarized current. The anisotropy gradient is dependent on the K_{uv} which will affect the velocity and direction of the magnetic skyrmionium. For the initial state of the nano-track, the skyrmionium will be initiated on the left/right of the nano-track, and driven by the current or anisotropy gradient.

6. 3 The pinning/depinning states of isolate skyrmionium in nano-track

The pinning/depinning states of the skyrmionium in a nanowire with a single wedge shape voltage gate are shown in Figure 6 .3. The effect of the width and current density has been given in Figure 6. 3. (a) and (b). The relaxed skyrmionium has been located at the left side of the nano-track in the initial state in Figure 6 .3. (a).

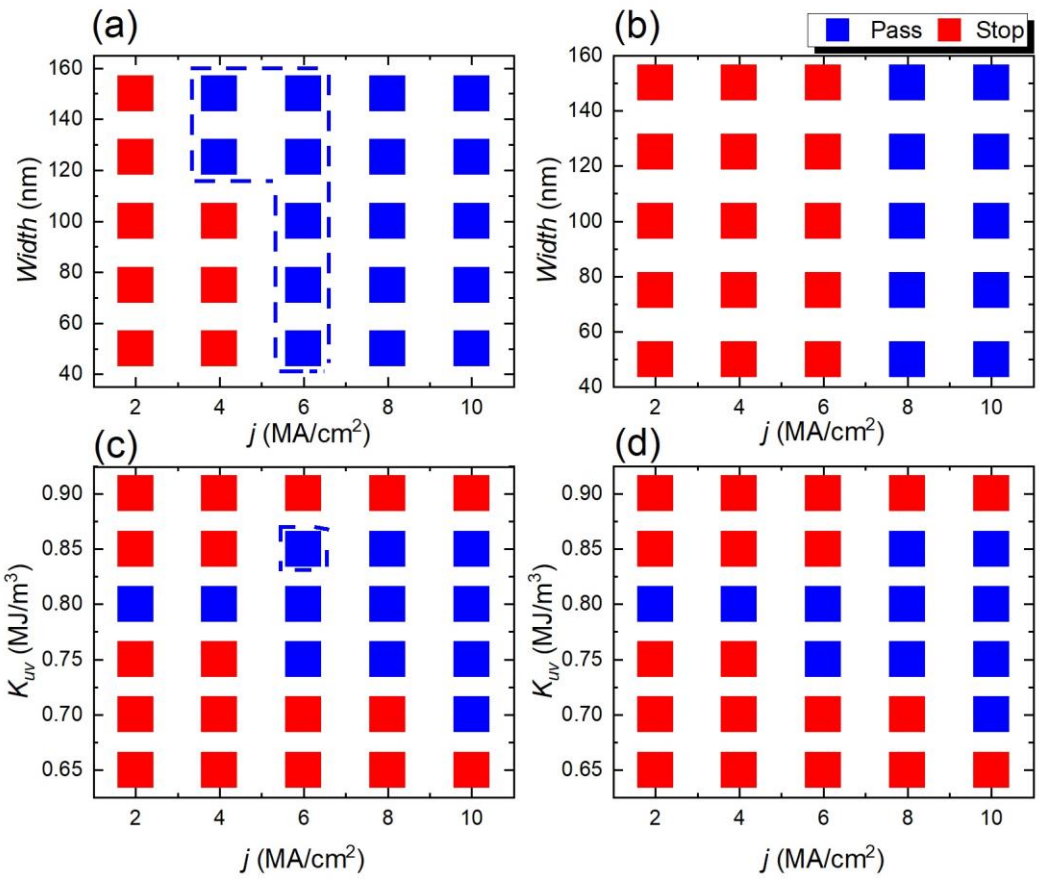

Figure 6.3 The pinning/depinning states of an isolate skyrmionium driven by current in a ferromagnetic nano-track with a single wedge voltage gate. Schematic configurations for the nanowire is given in Figure 6. 2(a). (a)(b)The pinning/depinning states of a skyrmionium with various width w from 40 nm to 160 nm and various driving current *j* from 2 MA/cm^2 to 10 MA/cm^2. The current *j* along the + *x* in the (a) and along - *x*-axis in the (b) for Kuv = 0.85 MJ

m^{-3}, respectively. (c)(d) The pinning/depinning states of a skyrmionium with various K_{uv} from 0.65 MJ m^{-3} to 0.90 MJ m^{-3} and various driving current j from 2 MA/cm^2 to 10 MA/cm^2. The current j along the + x in the (c) and along - x-axis in the (d). The width of the voltage gate is 100 nm in both (c) and (d). The solid red squares mean the skyrmionium is pinned by the voltage gate and the solid blue squares mean the skyrmionium can pass the voltage gate.

After applying the spin current along the +x direction, the skyrmionium moves towards the VCMA region. The width of the VCMA gate varies from 40 nm to 160 nm, which will change the slope of the VCMA gate. The K_{uv} of the VCMA gate varies from 0.65 MJ/m^3 to 0.90 MJ/m^3. According to the results in Figure 6. 3. (a), the VCMA region with a width w < 120 nm will pin the skyrmionium when spin current j < 6 MA/cm^2. When the width w increase to a size larger than 120 nm, the skyrmionium can pass the VCMA region which shows that the pinning/depinning state can be affected by the shape of the VCMA gradient. In Figure 6. 3(b), the skyrmionium is located at the right side of the VCMA region with a driving current along the -x-axis. When the current j < 8 MA/cm^2, the skyrmioniums are pinned at the VCMA region. The results in the blue dashed box show that the skyrmionium can display uni-directional behaviour along the +x-axis. In Figure 6. 3(c) and (d), the effect of the width and current density has been investigated. According to the results, the pinning/depinning state is sensitive to the VCMA. The parameters for the uni-direction pass along +x have been marked in a blue dashed box.

The x-component velocity of the skyrmionium motion in the nano-track with single voltage gate has been given in Figure 6.4 (a)(b). According to Figure 6.3(a), the skyrmionium go through a VCMA region with a K_{gap} = K_{uv} - K_u, the velocity of the skyrmiomium will increase/decrease when K_{gap} > 0 or < 0. In addition, when the $|K_{gap}|$ ≥ 0.10 MJ/m^{-3}, the skyrmionium is pinned at the VCMA because the current density is not large enough to drive it to pass the VCMA region. From Figure 6.3 (c), with the same current density j the larger K_{gap} will easier pin the skyrmion in the VCMA region. The phenomenon is demonstrated by the relationship between the current density and x-component velocity of skyrmionium in Figure 6.4(b). When the current density is not large enough to pass the VCMA region, the velocity of skyrmionium will reduce to 0

and pinned at VCMA the region. For the case with a current density larger than the threshold value, the velocity will increase after the skyrmiomium pass the VCMA region and then reduce to 0 at the edge of the nanotrack. The results demonstrate that the pinning/depinning states can be modulated by K_{gap} and width of VCMA region.

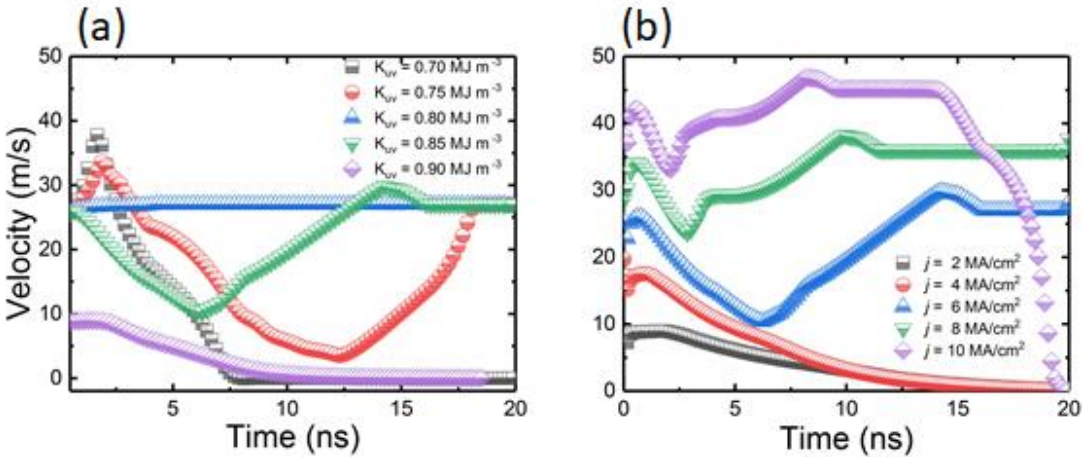

Figure 6.4 (a) The *x*-component velocity of skyrmionium motion in a nano-track induced by polarized current j = 6 MA/cm^2 and with a single voltage gate K_{uv} varying from 0.70 MJ m^{-3} to 0.90 MJ m^{-3}. (b) The *x*-component velocity of skyrmionium motion in a nano-track induced by polarized current density varying from j = 2 MA/cm^2 to 10 MA/cm^2 with a single voltage gate as 0.85 MJ m^{-3}.

6. 4 Anisotropy gradient induced skyrmionium motion in nano-track

That skyrmions can be driven by an anisotropy gradient has been reported recently [130, 131]. The skyrmion will move toward the area with a lower magnetic anisotropy. The high speed motion of magnetic skyrmion driven by polarized current is limited by the joule heating. On the other hand, the joule heating increases the device temperature

which will affect the stability of magnetic skyrmion/skyrmionium. Here, the velocity of the skyrmion/skyrmionium driven by an anisotropy gradient has been given in Figure 6.5(a).

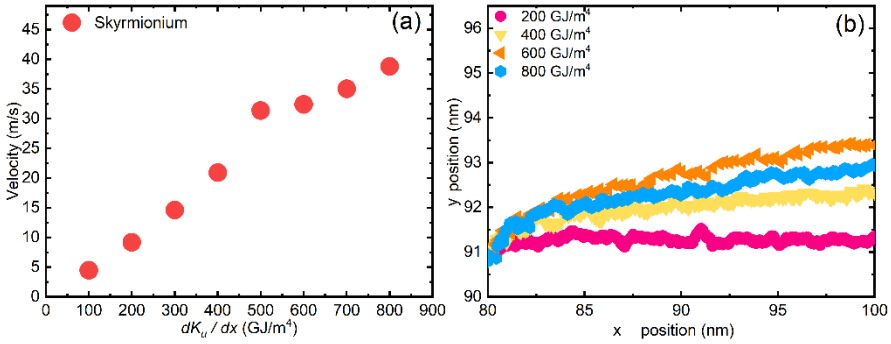

Figure 6.5 The velocity and trajectory of the magnetic skyrmionium motion driven by anisotropy energy gradient. (a) The velocity of skyrmionium driven by different anisotropy energy gradient. (b) Skyrmionium trajectories in nanowires driven by different anisotropy energy gradient, indicating that the skyrmionium trajectory is dependent on size of anisotropy energy gradient.

The anisotropy gradient in the system is varied from 100 GJ/m^4 to 900 GJ/m^4 and the velocity of the magnetic skyrmionium is directly proportion to the dK_u/dx. The trajectories of the magnetic skyrmionium induced by the anisotropy gradient has been given in Figure 6. 5(b). When the anisotropy gradient is applied to the system, the anisotropy will cause a radius changing of magnetic skyrmionium which is consistent with the theoretical expression of skyrmion radius. [132]

$$R_{sk} \approx \frac{\Delta Rsk}{\sqrt{2(1-D/D_c)}} \tag{6.2}$$

The radius and shape of the magnetic skyrmionium will affect the trajectories of the skyrmionium. Where the $\Delta = \sqrt{A/K}$ and $D_c = 4\sqrt{A/K}/\pi$. Also, the micromagnetic simulation results are sensitive to the size of the damping constant α. A lower α will

cause a higher speed. In Figure 6. 5(b), the y position of the skyrmionium will be influenced by the magnetic anisotropy of the x location. When the anisotropy deceases, the size of the skyrmionium will increase and shift away from the center of the nano-track.

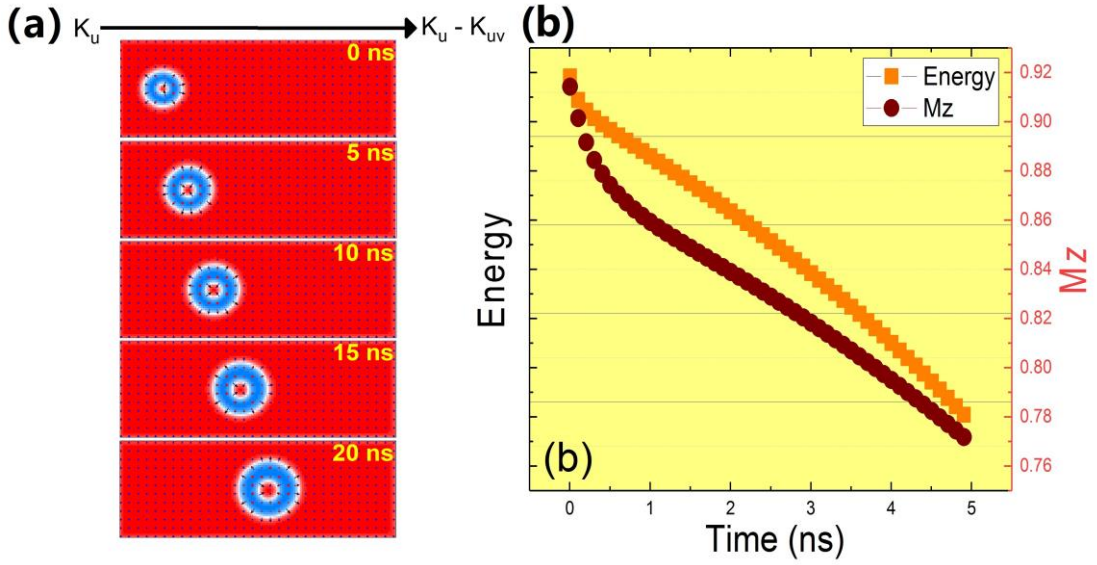

Figure 6.6 (a) The snapshot of magnetic skyrmionium motion in a nanotrack driven by an anisotropy gradient. The anisotropy gradient is 400 GJ/m^4((K_{max}-K_{min})/(device length)). The anisotropy energy decrease from left to right. (b) The total energy and magnetization in z direction M_z of the whole system. During the skyrmion motion, both the total energy and M_z decrease.

The dynamics of magnetic skyrmionium motion in a nanotrack induced by anisotropy gradient is given in Figure. 6. 6 (a). With an anisotropy gradient = 400 GJ/m^4, the skyrmionium motion along the x axis from the higher anisotropy to lower anisotropy. During the skyrmionium motion, the shape of the skyrmionium changing by the anisotropy gradient. When the anisotropy decrease, the size of skyrmionium increase. This phenomenon can also found in Figure. 6. 6 (b). When the skyrmionium motion in the nanotrack, the M_z decrease because of the size of the Q = -1 skyrmion has increase. The size of the skyrmionium is sensitive to the stability of the skyrmionium. The larger size will cause the skyrmionium easier reach the edge of the nanotrack. The width of the nanotrack and the range of the anisotropy gradient is important for the voltage driven skyrmionium based device.

6. 5 Conclusion

In this work, I proposed a magnetic skyrmionium motion in a nano-track with voltage gate and gradient. My simulation result shows that the trajectory and location of the skyrmionium can be controlled by periodically located voltage gate. The unidirectional motion of the skyrmionium realized by the VCMA effect can be used to build the skyrmion-based one- way information channel and the skyrmionium diode. In addition, I discuss the anisotropy gradient driven skyrmionium motion in a nano-track which can enhance the stability of the skyrmionium by avoiding the Joule heating. The skyrmionium can have the same velocity as the skyrmion and avoids the skyrmion Hall effect. The results are useful for the design and development of the skyrmionium based logical and memory device.

Chapter.7 Skyrmion dynamics under high thermal effect in IrCoPt multi-layer

For any application, skyrmion structures need to be stable at the working temperature (e.g. 300K-500K). The thermal stability of magnetic skyrmion in thin film is an important topic which can provide useful guidelines for the future skyrmion based spintronics devices. In this chapter, I have studied the spin texture behaviour under high thermal effect (300 K -500 K). The thermal-induced phase transition to a skyrmion state in IrCoPt has been demonstrated by the atomistic simulations parametrised from ab-initio calculations which include long-range exchange interactions. The simulation results give a clear vision of the thermal induced behaviour in a chiral magnetic thin film.

7. 1 Introduction

The Magnetic skyrmion, is a kind of topologically nontrivial magnetisation configuration which can be found in ferromagnetic material with Dzyaloshinskii-Moriya interaction (DMI) [31, 45, 89, 93]. The DMI relies on the spin orbit coupling which usually is provided by the heavy metal layer in the system.[97] Magnetic skyrmions have potential to be used in building novel skyrmion based information channel and logical devices [27, 103, 104]. Comparing with a magnetic domain wall, the magnetic skyrmion has a much lower critical current and smaller size. The magnetic skyrmion in the nanoscale device can be driven by spin polarized current, magnon force and temperature gradient [51, 55, 98, 121]. During the displacement of magnetic

skyrmion motion driven by current or gradient in the nanoscale device, the Magnus force on the skyrmion will cause an effect which will induce the skyrmion motion toward the edge. The effect has been called as Skyrmion Hall effect (SkHE).[53]

The thermal effect has usually been considered as detrimental to magnetic skyrmions. The behaviour of Magnetic skyrmions under strong thermal effect is a significant research topic which can provide guidelines to the room temperature skyrmion based device. The magnetic skyrmion generated by temperature pulse has been observed by theory calculation and experiment.[133, 134] In this chapter, I used atomistic simulation to study the skyrmion dynamics under high thermal effect (from 300 K to 500 K). The simulation result has demonstrated the phase transition between the skyrmion, stripe domain and ferromagnetic state.

7. 2 Atomistic modelling and Stochastic LLG equation

Atomistic spin models cover the gap between two distinct approaches, namely micromagnetics and ab-initio models of the electronic structure. The advantage of the atomistic model over micromagnetics is that it naturally deals with atomic ordering and variation of local properties seen in real materials, such as interfaces, defects, roughness etc. The discrete formulation also allows the simulation of high temperatures above and beyond the Curie temperature, where the usual continuum micromagnetic approach breaks down. Such effects are often central to current problems in magnetism such as materials for spin electronics, heat assisted magnetic recording or ultrafast laser processes. Similarly for ab-initio calculations, mapping onto an effective spin model allows to apply the full quantum mechanical calculation of essential properties to much larger systems and the consideration of dynamic effects on much longer timescales. The atomistic simulations have been performed using the software package Vampire 5.0 which is designed by computation magnetism group in York.

The simulation model considers finite temperature, by the introduction of the stochastic field $\vec{\xi}_i(t)$ into the effective field in the LLG equation. By this process, the spin system is coupled with a heat bath. Within this approach, the stochastic field term is introduced as a white noise term. [135-137] In order to make the simulation more accurately, the time correlation between the thermal induced fluctuations should shorter than the spin motion.[135] To obey the fluctuation-dissipation theory and to obtain the correct equilibrium distributions, the accuracy of the results is assured by a timestep as $5*10^{-16}$. The stochastic field is treated as white noise in the system.

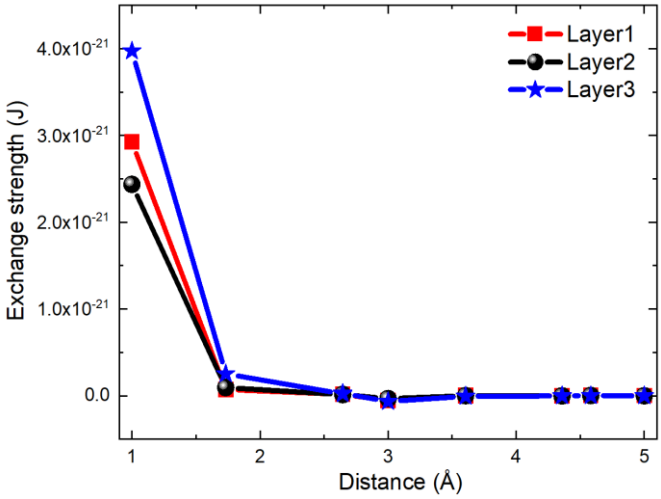

Figure 7.1 The material system is $[Co3Ir3Co3Pt3]_n$. The parameter for the middle stack of the 3 Cobalt has been used in the simulation. The middle layer has been defined as three different Cobalt layer. The layer1 is the Cobalt atom interfaced with the Iridium atom, the layer2 is the Cobalt atom between two Cobalt layer and the layer3 is the Cobalt atom interfaced with the Platinum. The exchange strength per link for different layer cobalt atom in the material system is given in figure

The parameters used for simulation are from the ab-initio calculation provided by Prof. László Szunyogh. The material system is $[Co3Ir3Co3Pt3]_n$, in which the symmetry breaking of Platinum and Iridium in the system provides a DMI to the Cobalt layers. In the modelling, I only considered the middle 3-monolayer Cobalt layer in the system, because each 3-monolayer Cobalt layer only has a weak exchange interaction

with other 3-monolayer Cobalt layer. The middle layer has been defined as three different atomic layers of Cobalt. The layer1 is the Cobalt atom interfaced with the Iridium atom, the layer2 is the Cobalt atom between two Cobalt layer and the layer3 is the Cobalt atom interfaced with the Platinum. From Figure 7.1 the exchange strength is increase from the layer1 to layer3 because of the stronger spin orbit coupling in the Platinum interface.

The spin moment and anisotropy of the middle 3 Cobalt layers are given as below. The ab-initio (From the beginning) data present a strong two-ion anisotropy, that gives an in-plane contribution to the anisotropy that cancels the out-of-plane uniaxial anisotropy. The anisotropy energy has been two times enhanced in order to get a perpendicular system. Additionally, this will provide a decrease in the size of the skyrmion lattice. All of these parameters are calculated ab-initio and are 0K values.

	K_u (J/atom)	Atom spin moment (μ_B)
Cobalt Layer 1	$3.5328 * 10^{-23}$	1.6717
Cobalt Layer 2	$5.5898 * 10^{-23}$	1.7612
Cobalt Layer 3	$11.5332 * 10^{-23}$	1.7829

7. 3 Curie temperature of the system

The Curie temperature T_c of the system can be calculated by the *Vampire* software package, and it is to be expected that the T_c value will be affect by the DMI in the material. The DMI in the material will stable the magnetic structure in the system which will make the simulation output T_c much lower than the real T_c of the system. When the thermal field applied to the system, there will have stripe domain generated in the system which will reduce the mean magnetisation length of the system. In this section, I have simulated the system with/without DMI. The result for the simulations are given

in Figure 7. 2. The model size of the Currier temperature simulation is 10 nm * 10 nm * 0.25 nm and with periodic boundaries condition in x direction and y-direction.

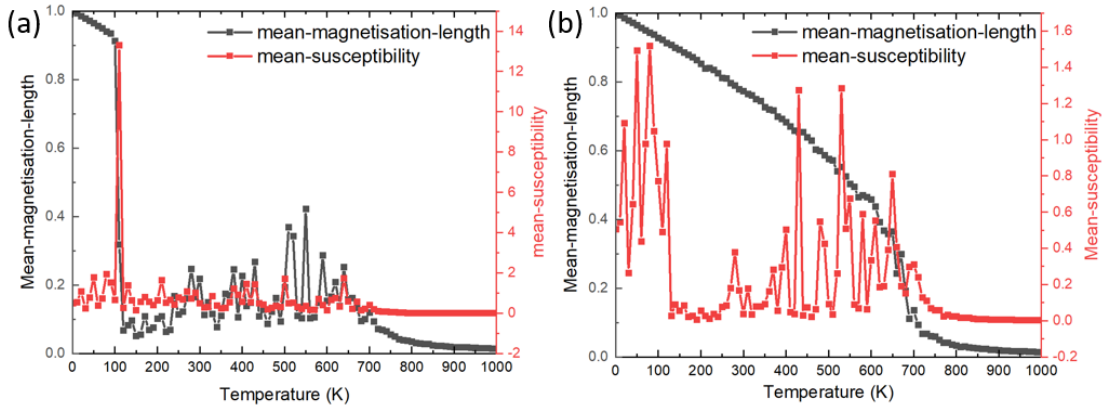

Figure 7.2 The mean-magnetisation-length and mean-susceptibility of the system. (a) The simulation include DMI. (b) The system without DMI.

According to Figure 7. 2(a), the apparent T_c of the system is affected by the DMI. When the temperature is above 100K, there are spin textures generated by the thermal field in the system which reduces the mean-magnetisation-length (mean magnetisation of the whole system) in the system. The mean-susceptibility for the whole system shows a peak value when the temperature around 100 K which also mean the system generate some spin texture. The DMI in the system stabilises the spin texture which induces the mean-magnetisation-length collapse to near zero. As a result, Fig 7.2(a) does not illustrate the disappearance of magnetic order at 100K. Then for the simulation in Figure 7. 2(b), the system excludes the DMI shows the real temperature-magnetisation curve (without the DMI) of the system. The T_c for this system is around 700 K, consistent with the exchange strength in the system. The collapse of the magnetisation in Figure 7. 2 (a) is a result of a transition to a magnetic texture with a low magnetisation rather than a phase transition: locally the magnetisation remains large, the thermal induced system transition to a different magnetic state (From ferromagnetic state to stripe domain state) is discussed in section 7.4.2. The result in Figure 7. 2 (a)-(b) give us useful information of the thermal property of this material.

7. 4 Spin configuration after field cooling

The magnetic skyrmion can be generated by a temperature pulse as has been studied recently theoretically and experimentally. [126, 134, 138] When an un-polarzed laser pulse heats the sample to *Tc*, the whole system will transition to a demagnetized state. Then as the whole system temperature reduces, the domain/skyrmion structure will be nucleated in the system. In the atomistic simulation, I consider the system cooling from the demagnetized state with a cooling time of 2 ns. The initial system temperature is 700 K and then reduce to 0 K in 2 ns. The simulation results for the 2 ns cooling process without external field and with a field of 1 Tesla (In order to get a reasonable skyrmion size) are given in Figure 7. 2 - Figure 7. 3. The system size is 20 nm * 20 nm and the thickness is 3 layer Cobalt atoms (0.25 nm) and with periodic boundaries condition in x-direction and y-direction.

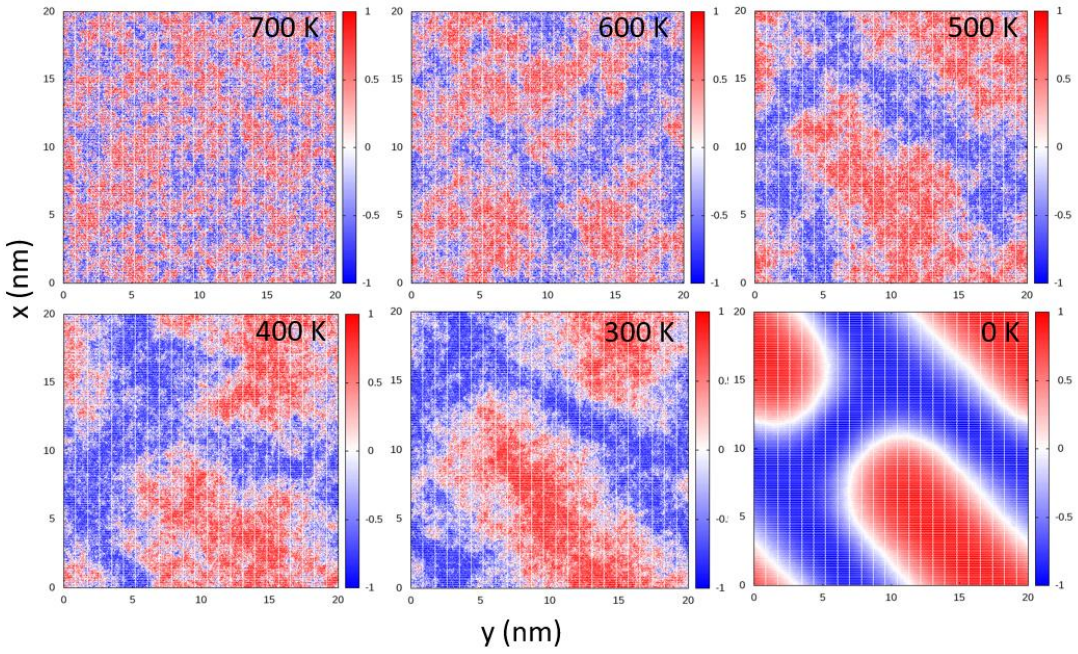

Figure 7.3 The spin configuration of the system under different temperature condition without external field. The system size is 20 nm * 20 nm * 0.25 nm with periodic boundaries condition in x direction and y direction, and the colour palette is determined by the M_z (red for +1, white for 0 and blue for -1)

According to the simulation results in Figure 7.3, the spin configurations at different temperature are shown. When the temperature equals 700K, the system is in demagnetized, and the spin configuration is random due to the strong thermal field. Then when the temperature cools from 700 K to 300 K, there is some stripe domain nucleation in the system and diffusion due to the thermal effect. From Figure 7. 3 the spin texture in system displays a stripe domain phase when the system cools from T_c. The stripe domain displays perfect DMI induced in-plane edge when the system temperature is reduced to zero.

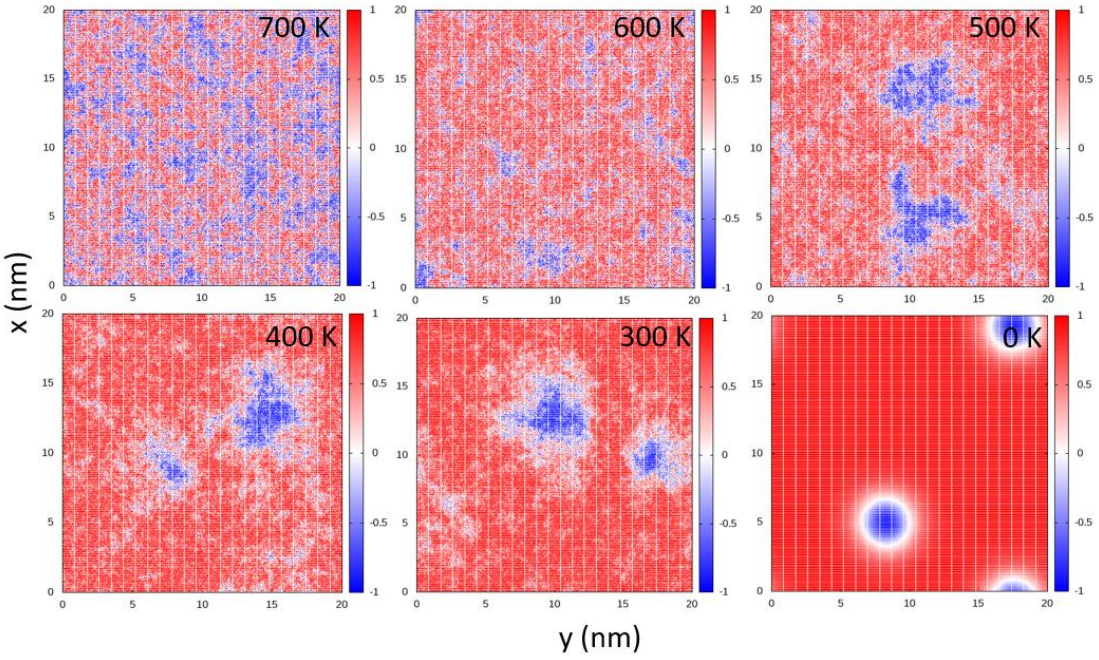

Figure 7.4 The spin configuration of the system under different temperature condition with out-of-plane external field equal 1T. The system size is 20 nm * 20 nm * 0.25 nm with periodic boundaries condition in x-direction and y-direction, and the colour palette is determined by the M_z (red for +1, white for 0 and blue for -1)

I now consider the case of large externally applied field. Figure 7.4 shows the spin configuration under different temperature with 1T out-of-plane external field. When the temperature equals 700K, the system is in demagnetised and the spin configuration is disordered. Then when the temperature cools from 700 K to 600 K, there is the

development of a magnetic texture and at a temperature of 500 K, there are two deformed skyrmions generated in the system. As the temperature is lowered the skyrmion phase becomes well established. Clearly, field cooling is effective in generating skyrmion structures.

7. 5 Material behaviour under high thermal effect

7.5.1 Initial state for the simulation

There are three magnetic phases in the CoPt multilayer system: the ferromagnetic phase, the stripe domain phase and the skyrmion lattice phase which has also been found in other systems.[45] The simulation for the skyrmion at elevated temperatures also shows the thermally induced phase transition between these three phases. The initial spin configurations are given in Figure 7.5. The system size is 30 nm * 30 nm * 0.25 nm, with periodic boundaries condition in x-direction and y-direction.

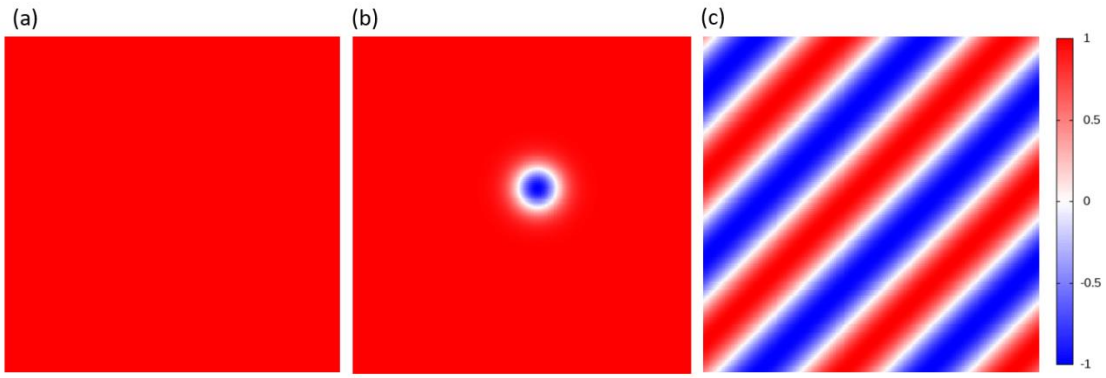

Figure 7.5 The initial spin configuration which has the different phase of the atomistic simulation with temperature as 0 K, the system size is 30 nm * 30 nm with periodic boundaries condition in x-direction and y-direction. The spin configuration is set before the simulation. (a) Ferromagnetic phase (b) Skyrmion phase (c) Stripe domain phase. The colour palette is determined by the M_z (red for +1, white for 0 and blue for -1)

The ferromagnetic phase and perfect stripe domain phase has already been relaxed without external field and thermal field. For the skyrmion phase, the spin in the system is relaxed with an external field of 1 T. The skyrmion will change to a suitable size for the atomsitic simulation, because of the competition between DMI and external field.

7.5.2 The ferromagnetic phase under different temperature condition

According to the simulation result in Figure 7. 2(a), when the temperature is higher than 100 K, the mean-magnetisation-length will drop to near 0, which means the system has changed to a different magnetic state. The simulation result of the time evolution of the ferromagnetic state under 150 K (low temperature) condition without external field is given in Figure 7. 6. The system size of the simulation is 30 nm * 30 nm * 0.25 nm with periodic boundaries condition in x-direction and y-direction.

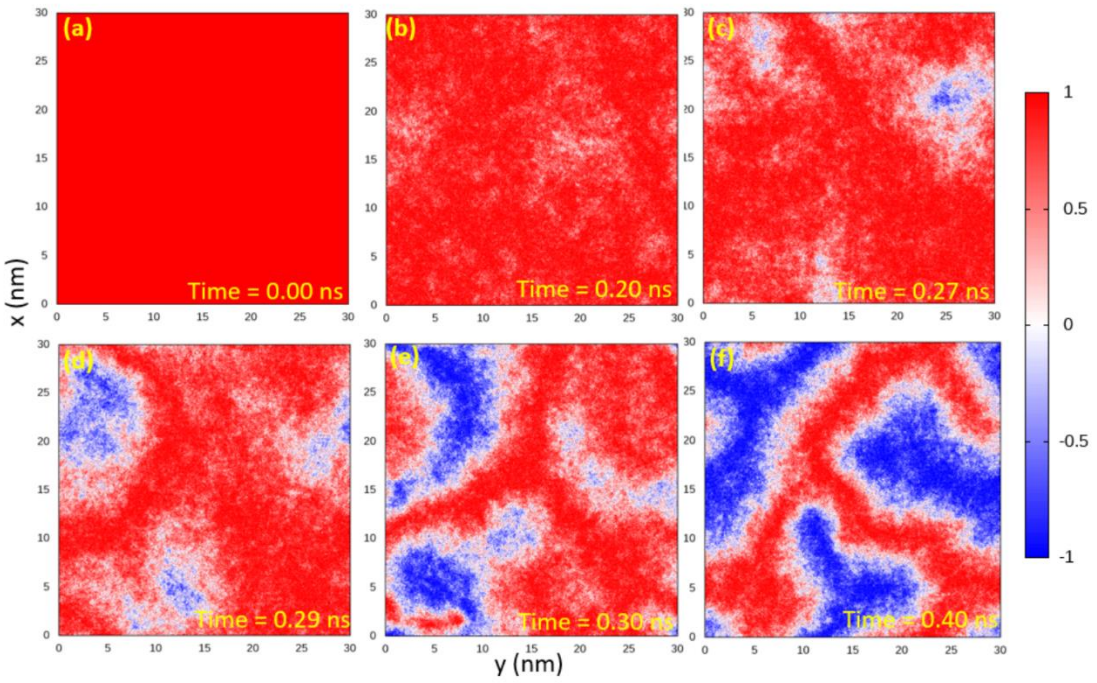

Figure 7.6 Spin configuration of the ferromagnetic phase under temperature = 150 K condition without thermal field. The system size of the simulation is 30 nm * 30 nm * 0.25 nm with periodic boundaries condition in x direction and y direction. The colour palette is determined by the M_z (red for +1, white for 0 and blue for -1) (a) The initial state (b) Time =

0.1 ns (c) Time = 0.2 ns (d) Time = 0.27 ns (e) Time = 0.29 ns (f) Time = 0.4 ns

According to Figure 7.2 (a), the ferromagnetic phase is stable at low temperatures. When the system temperature is greater than 100 K, the mean-magnetisation-length collapses to 0 which means there are some spin texture generated in the system. From Figure 7.6 (a) – (b), I can see the thermally induced fluctuations in the system. Then in Figure 7 .6 (c) – (e), the reversed spins has been stabilized by the DM interaction in the system and there are some spin structures generated. Finally, in Figure 7. 6 (f), the spin structure changes to a stripe domain structure. The relationship between the simulation time and mean-magnetisation-length is given in Figure 7. 7, which shows when the thermally induced spin structure nucleate in the system and the mean-magnetisation decreases toward 0. The result shows that the transition from ferromagnetic state to stripe domain state only requires very low thermal activation. Also, the stripe domain state in the system with DM interaction can be seen as an energy minimum state.

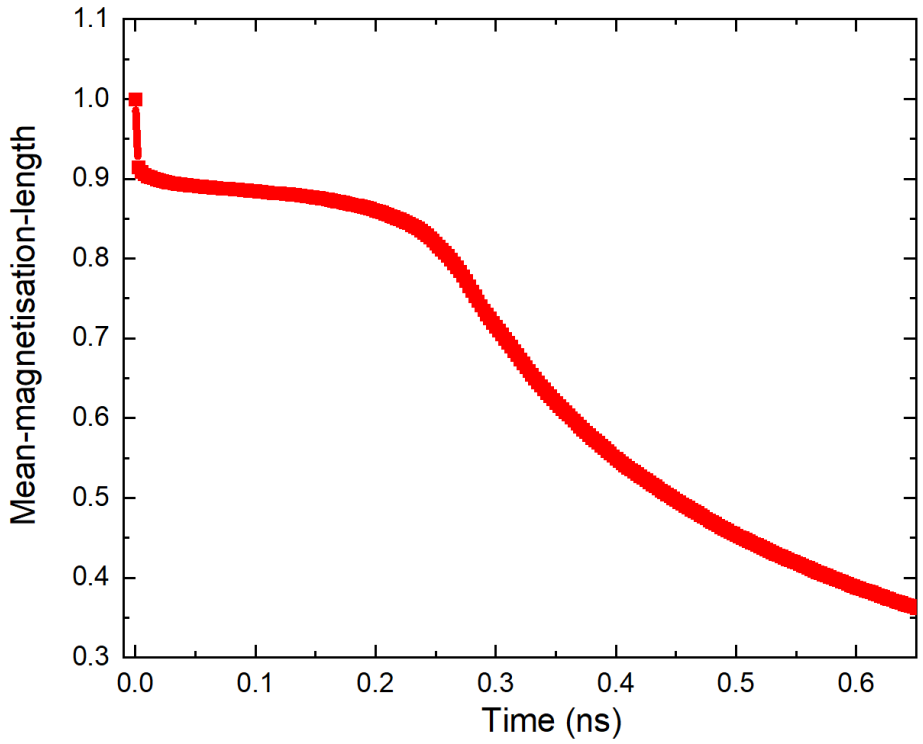

Figure 7.7 The time dependent mean-magnetisation-time under 150 K thermal condition.

The ferromagnetic phase under high thermal condition (300 K to 500 K) also been simulated in this section. The simulation time has been set as 10 ns which is long enough will give a clear version of the phase transition in the system.

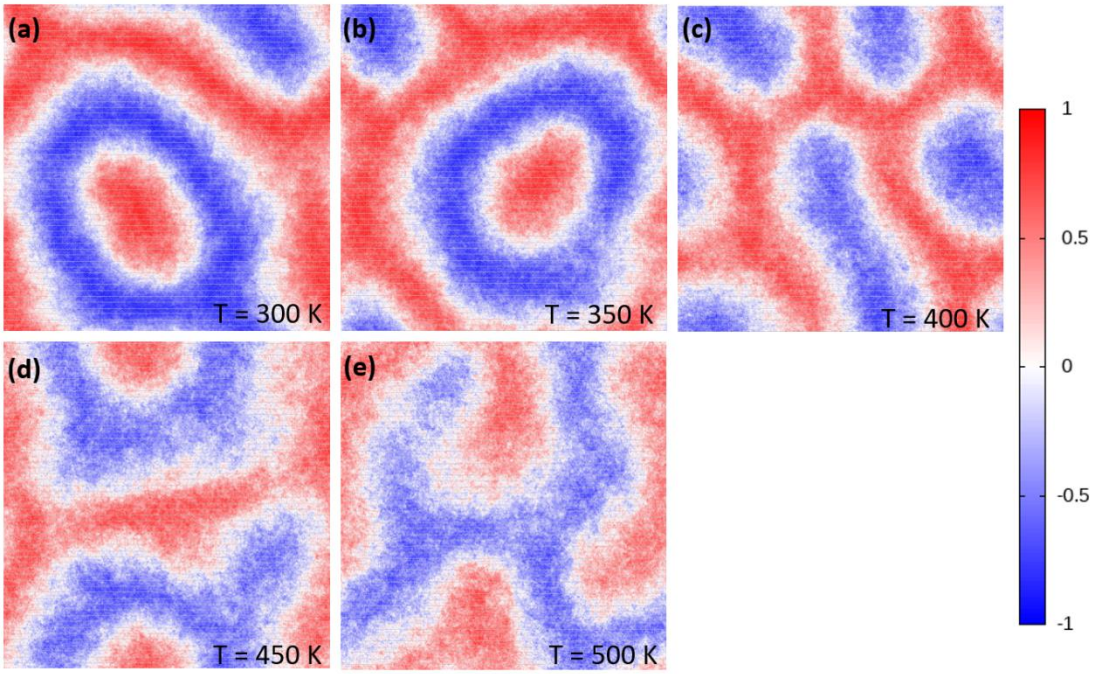

Figure 7.8 The spin configuration for the ferromagnetic phase under different temperature condition after 10 ns. The system size of the simulation is 30 nm * 30 nm * 0.25 nm with periodic boundaries condition in x-direction and y-direction. The colour palette is determined by the M_z (red for +1, white for 0 and blue for -1) The result is average from 10 spin configurations in the same time range, in order to avoid the stronger thermal noise. The temperature in each figure is (a) 300K (b) 350K (c) 400 K (d) 450 K (e) 500K and without external field.

The spin configurations in Figure 7. 8(a)-(d) show spin configurations for the ferromagnetic state under different temperatures condition after 10 ns. It can be seen that the ferromagnetic state has transitioned to the stripe domain and skyrmion bubble phases. The spin textures are generated by the thermal activation and stabilized by the DM interaction. Especially, in Figure 7.8 (b), a skyrmionium has been generated by the thermal effect, and in Figure 7. 8(e), the spin configurations display a stripe domain state without any skyrmion bubbles in the system.

The spin configuration of the skyrmionium generated by thermal activation is given below in Figure 7 .9. The skyrmionium can be seen as a combination of two skyrmions with opposite skyrmion number stabilized by the DM interaction. The skyrmionium created by a laser pulse has been reported and demonstrated by experiment.[126]

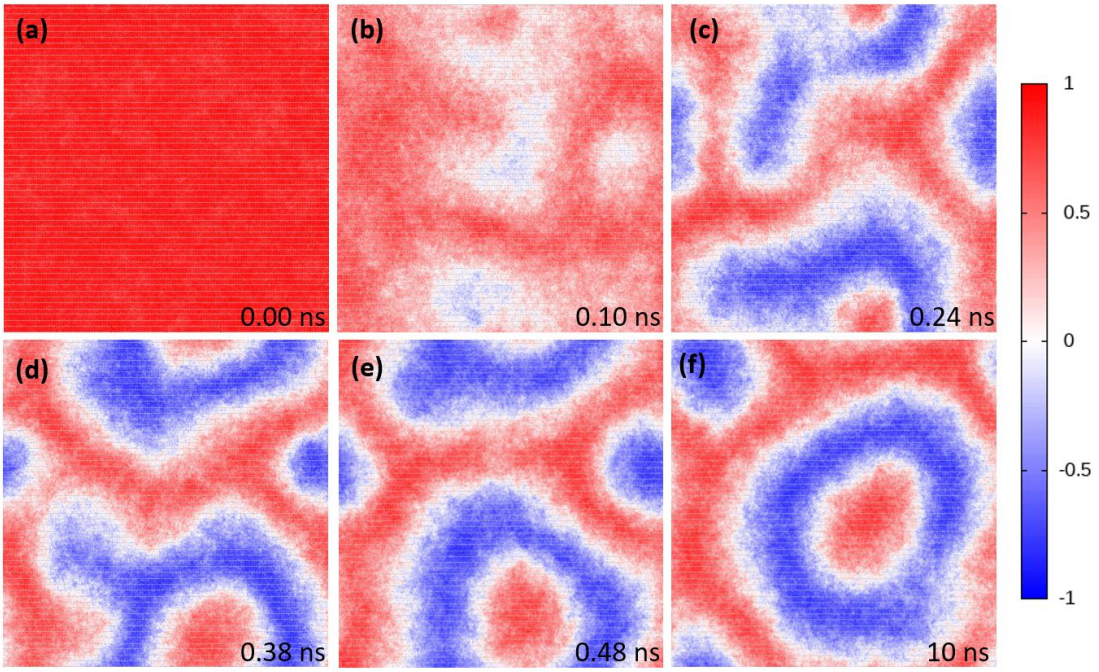

Figure 7.9 Magnetic skyrminium generated in the system though thermal effect with temperature as 350 K. The system size of the simulation is 30 nm * 30 nm * 0.25 nm with periodic boundaries condition in x-direction and y-direction. The colour palette is determined by the M_z (red for +1, white for 0 and blue for -1) The result is average from 10 spin configurations in the same time range, in order to avoid the stronger thermal noise.

In Figure 7.9 (a)-(b), the spin configurations show the thermally induced spin fluctuation in the system. There are some spin texture generated by thermal effect in the system. Because the simulation model is defect free, the shape of spin texture is only dependent on the random thermal effects. When the spin texture is generated in the system it is one of: stripe domain, skyrmion bubble and skyrmionium. Unlike the field cooling process in Figure 7.3, the transition from the ferromagnetic to stripe

domain state is very fast and can happen only at low temperature. Then in Figure 7.9 (c) – (e), is shown the spin texture fluctuations in the system where it can be seen that the spin texture is dynamically deformed by the random thermal fields. A skyrmion bubble and a skyrmionium are nucleated in the system and diffuse due to the thermal effects. From Figure 7. 9(f), it can be seen that the skyrmion and skyrmionium are stable for more than 10 ns at 350 K. The result shows that the random spin texture can be generated by thermal field from the ferromagnetic state, and the stripe domain skyrmion bubble hybrid phase can be stable in the high-temperature condition without an external field in 10 ns.

7.5.3 The stripe domain state under different temperature condition

The perfect stripe domain phase under high thermal condition (300 K to 500 K) is investigated in this section. The simulation time has been set as 10 ns which is long enough to give a clear diagram of the phase transition in the system. The initial state for the spin configuration is given in Figure 7. 5(c). The stripe domain state can be stable without external field and at 0K. The 10 ns simulation for the stripe domain state for different temperatures is given in Figure 7. 10. According to Figure 7.10 (a) – (c), the thermal effect distorts the shape of the stripe domain. In Figure 7. 10 (e)-(f), the stripe domain has been destroyed by the thermal effect. When the temperature is below the critical temperature for destruction of the stripe domain, the stripe domains diffuse due to the thermal effects to an extent which is temperature dependent. When the temperature increase above a critical temperature, the stripe domain changes to the stripe domain with a bent shape. The spin configurations for the stripe domain destroyed by the thermal effect are given in Figure 7. 11 – Figure 7. 12.

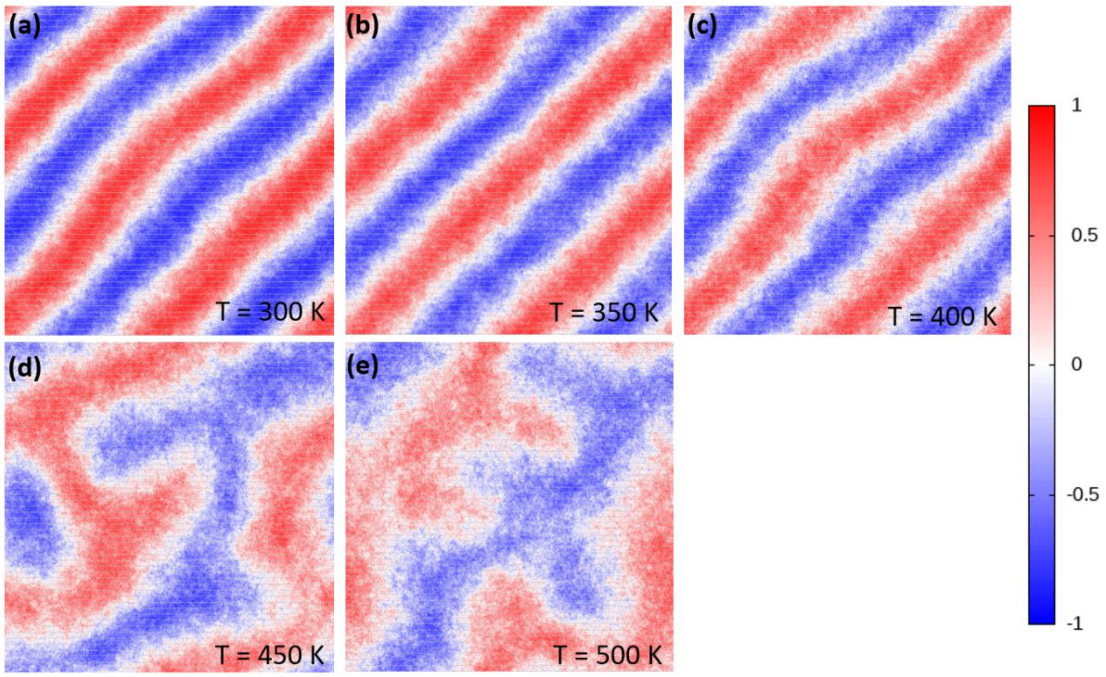

Figure 7.10 The spin configuration for the stripe domain phase under different temperature condition after 10 ns. The system size of the simulation is 30 nm * 30 nm * 0.25 nm with periodic boundaries condition in x-direction and y-direction. The colour palette is determined by the M_z (red for +1, white for 0 and blue for -1). The result is the average from 10 spin configurations in the same time range, in order to avoid the stronger thermal noise. The temperature in each figure is (a) 300K (b) 350K (c) 400 K (d) 450 K (e) 500K and without external field.

According to the spin configuration in Figure 7.11 (a) - (c), the thermal induced stripe domain diffusion is occurring. The stripe domain is deformed due to the thermal effect and becomes less stable. In Figure 7.11 (c) - (f), the stripe domain has broken at the middle and the size of the stripe domain reduce to a smaller length. Also the structure becomes closed which is consistent with the skyrmion number of -1. It shows that, under the thermal effect the stripe domain is not stable and the structure will change to a more stable structure.

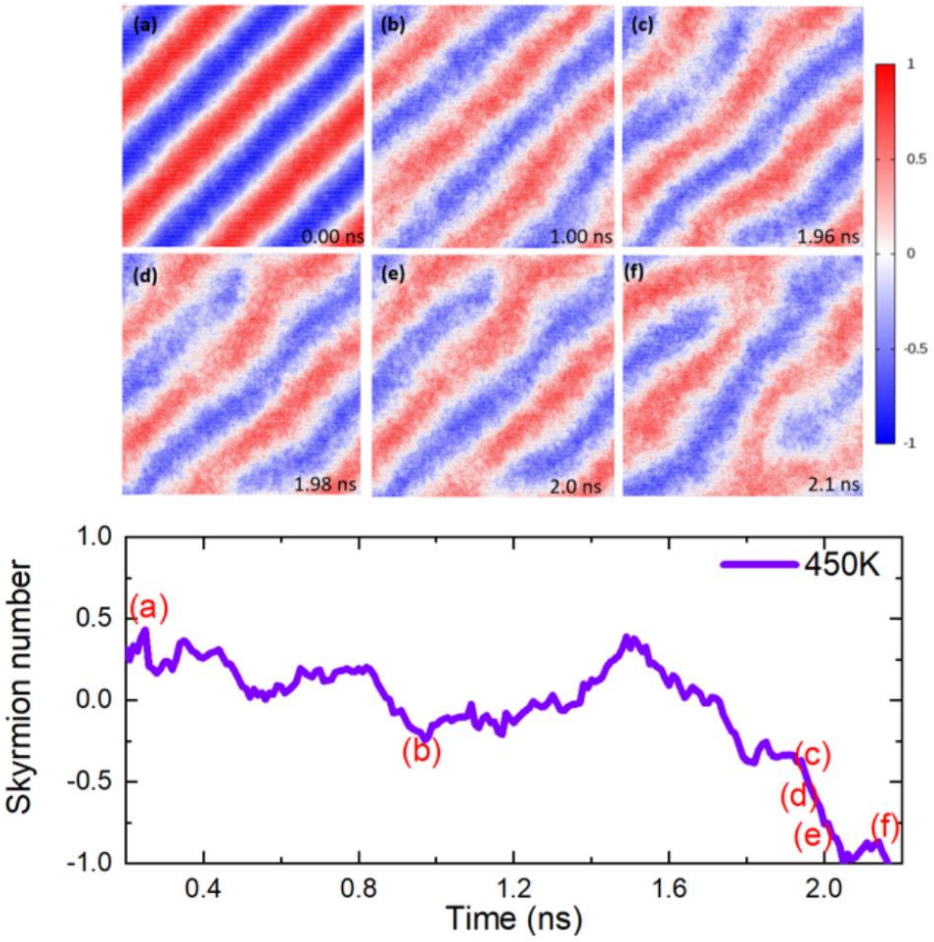

Figure 7.11 The spin configuration for the stripe domain broke under 450 K thermal condition. The system size of the simulation is 30 nm * 30 nm * 0.25 nm with periodic boundary condition in x-direction and y-direction. The colour palette is determined by the M_z (red for +1, white for 0 and blue for -1). The result is the average from 10 spin configurations in the same time range, in order to avoid the stronger thermal noise. The skyrmion number of (a) - (f) after averaged is given below the (a)-(f)

The further evolution of the spin configuration of the stripe domain is given in Figure 12 (a) - (f). From Figure 12 (a) – (e), the stripe domain state has transitioned toa skyrmion/stripe domain hybrid phase. According to the transition from ferromagnetic to the skyrmion stripe domain/hybrid state which has been discussed in the previous section, the skyrmion/stripe domain can be seen as the minimum energy state of the system at high temperature without an external field.

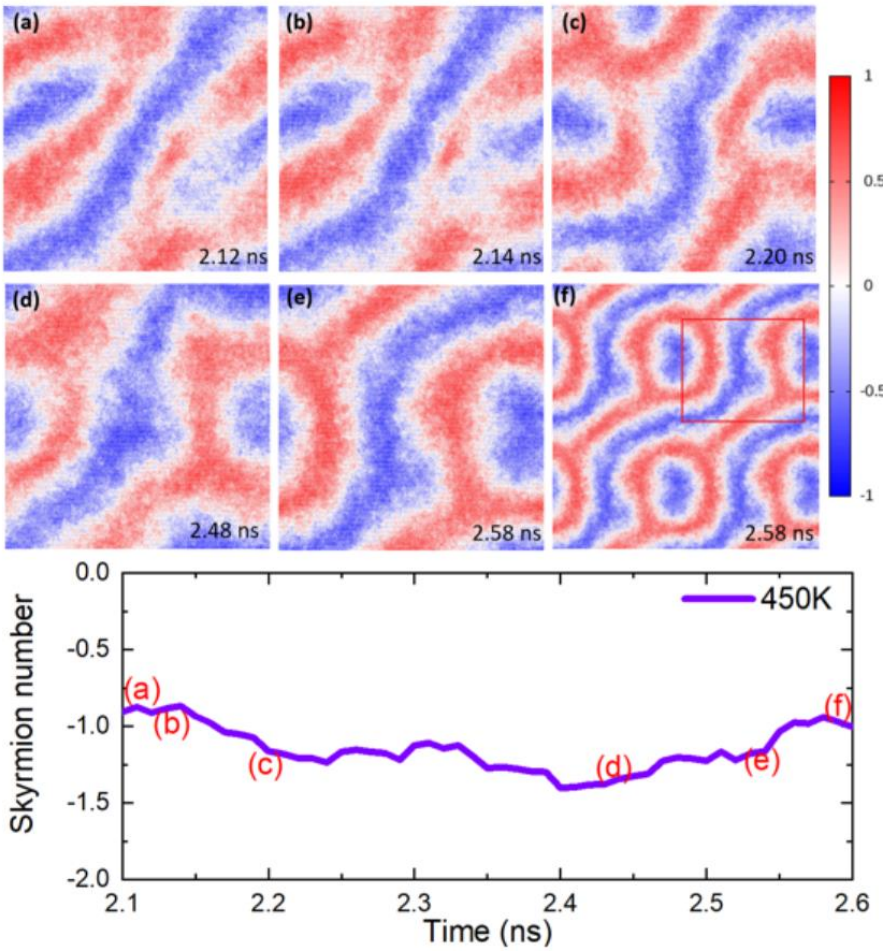

Figure 7.12 The spin configuration for the stripe domain broken under 450 K thermal condition. The system size of the simulation is 30 nm * 30 nm * 0.25 nm with periodic boundary condition in x-direction and y-direction. The colour palette is determined by the M_z (red for +1, white for 0 and blue for -1) The result is average from 10 spin configurations in the same time range, in order to avoid the stronger thermal noise. (a)-(e) The spin confirmation in different simulation time. (f) The merged figure which shows the whole spin texture structure. The spin configuration in the 30 nm * 30 nm system has been marked in the figure. The skyrmion number of (a) - (f) after averaged is given below the (a)-(f)

7.5.4 The skyrmion state as a function of temperature: skyrmion creation at elevated temperature

The skyrmion state as a function of temperature (300 K to 500 K) is investigated in this section. The simulation time has been set as 10 ns which is long enough to give a clear version of any transitions in the system. The initial state for the spin configuration

is given in Figure 7. 5(b). The skyrmion lattice state is stable with external field equal to 1 T and without thermal effect. The 10 ns simulation for the skyrmion lattice phase for different temperatures is shown in Figure 7. 13.

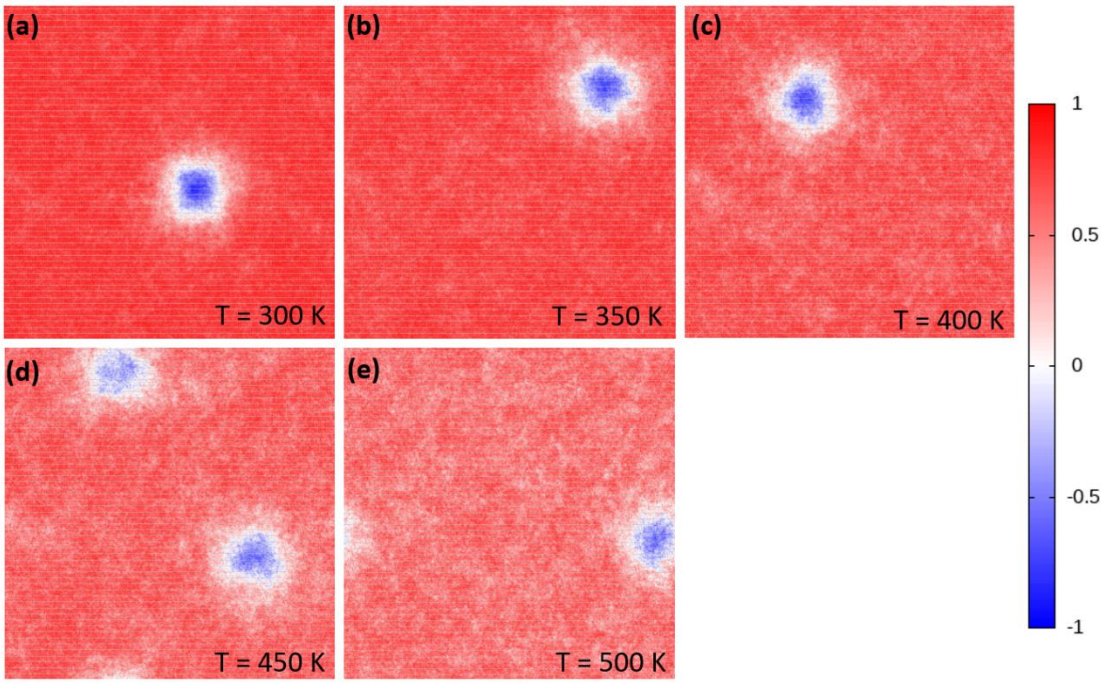

Figure 7.13 The spin configuration for the skyrmion lattice state under different temperature condition after 10 ns. The system size of the simulation is 30 nm * 30 nm * 0.25 nm with periodic boundary condition in x-direction and y-direction. The colour palette is determined by the M_z (red for +1, white for 0 and blue for -1) The result is average from 10 spin configurations in the same time range, in order to avoid the stronger thermal noise. The temperature in each figure is (a) 300K (b) 350K (c) 400 K (d) 450 K (e) 500K

From the simulation results in Figure 7. 13 (a) - (c), the skyrmion is topologically stable and diffusive in the system due to the thermal effect. In the final state for the skyrmion under 450 K thermal condition, the image shows two skyrmions in the system which means that at temperature greater than around 400 K, spontaneous thermal creation of skyrmions appears. The calculated time dependence of the skyrmion number for temperatures from 450 K to 500 K is shown in Figure 7.14. The skyrmion number for the initial skyrmion state is -1. The observed time dependence of the skyrmion

number is indicative of the creation and annihilation of skyrmions at elevated temperatures. The data show large variations over temperature because of the small system size, although a trend towards larger skyrmion numbers and more rapid creation and annihilation can be seen. However, this an interesting observation, which needs further investigation with larger sample sizes

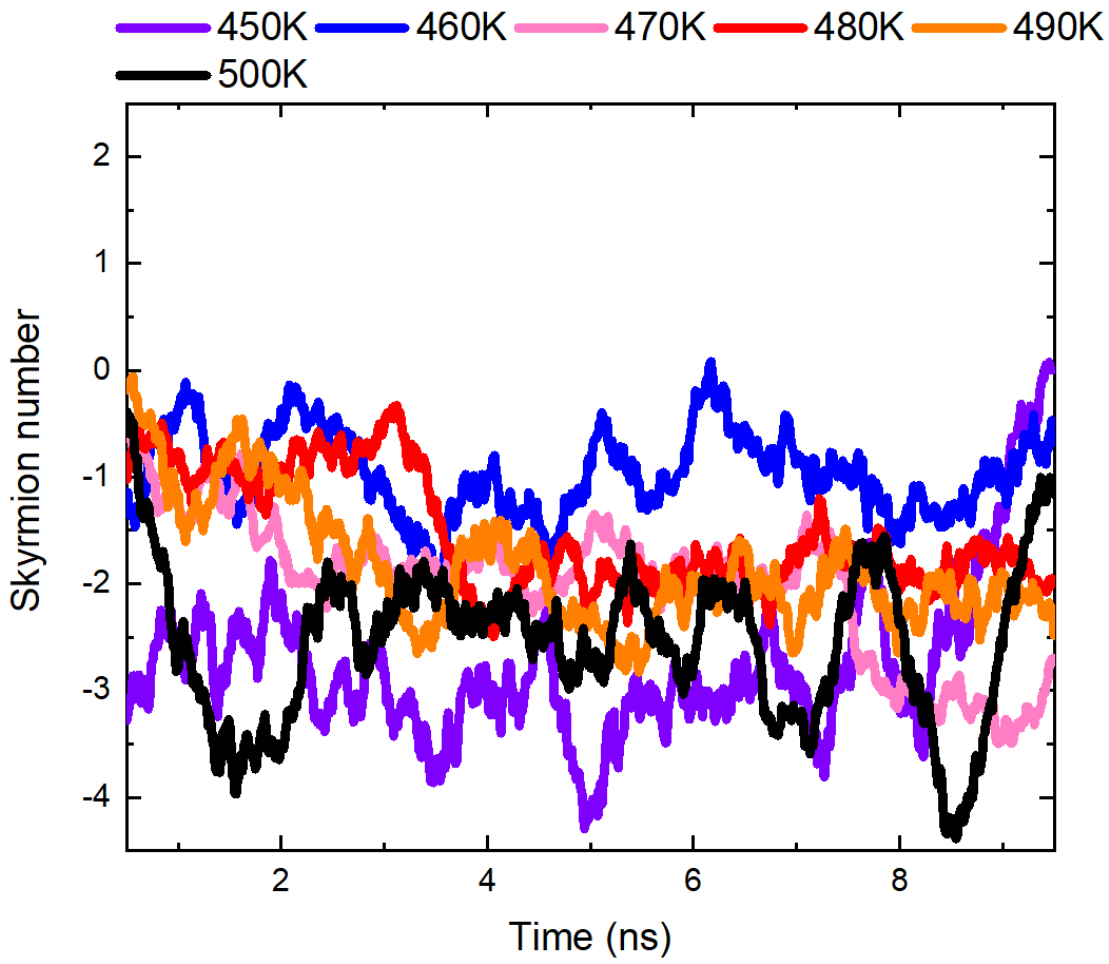

Figure 7.14 Skyrmion number *Q* for the system under different temperature condition. The system size of the simulation is 30 nm * 30 nm * 0.25 nm with periodic boundary condition in x-direction and y-direction.

Particularly, for the 500 K case, the skyrmion number Q is changing especially rapidly. Generation and destruction of skyrmions over time are shown. In Figure 7. 15 (0.6ns to 0.8ns) and Figure 7. 16 (2.1ns to 2.4ns).

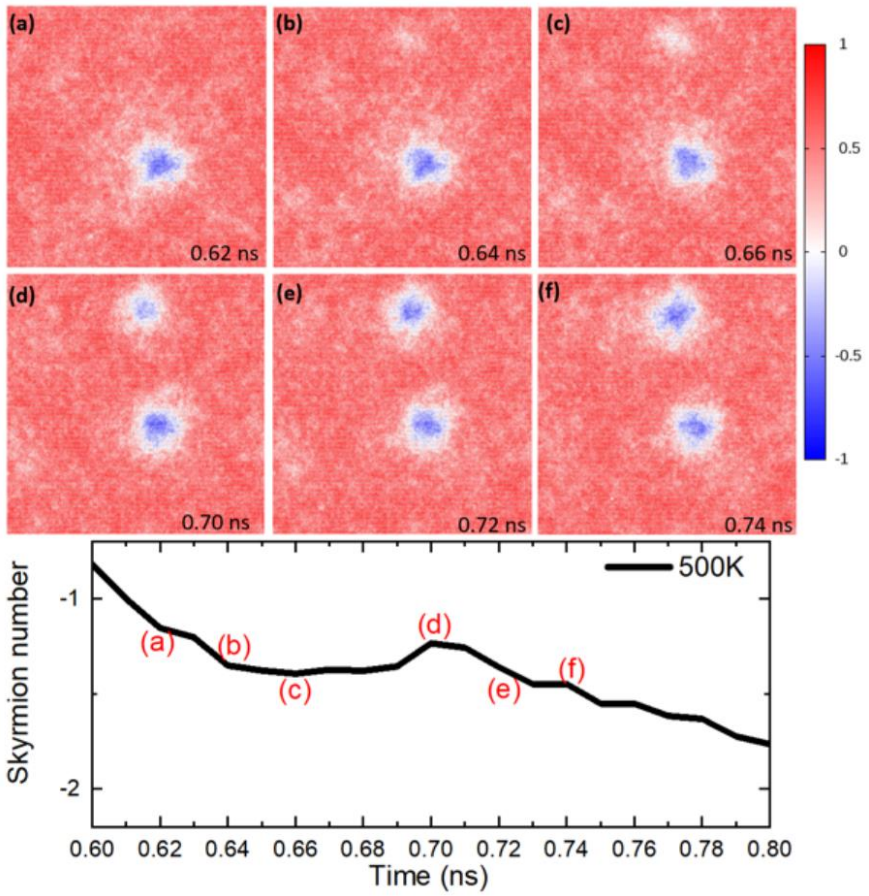

Figure 7.15 The spin configuration for skyrmion nucleated in the system by 500 K thermal condition. The system size of the simulation is 30 nm * 30 nm * 0.25 nm with periodic boundary condition in x-direction and y-direction with external field as 1 T. The colour palette is determined by the M_z (red for +1, white for 0 and blue for -1) The result is average from 10 spin configurations in the same time range, in order to avoid the stronger thermal noise. The skyrmion number of (a) - (f) after averaged is given below the (a)-(f)

According to the spin configuration in Figure 7. 15, the spin fluctuates in the system and flip spins generate the core of the spin texture which is stabilised by the DMI. The DMI in the system protects the spin texture from the thermal effects and external field, and the spins are twisted around the core. From Figure 7. 15 (a) – (e), a second skyrmion first generated by the thermal field grows to the same size as the original skyrmion. The size of the skyrmion is dependent on the exchange interaction, DMI and magnetic anisotropy, which are temperature dependent [139].

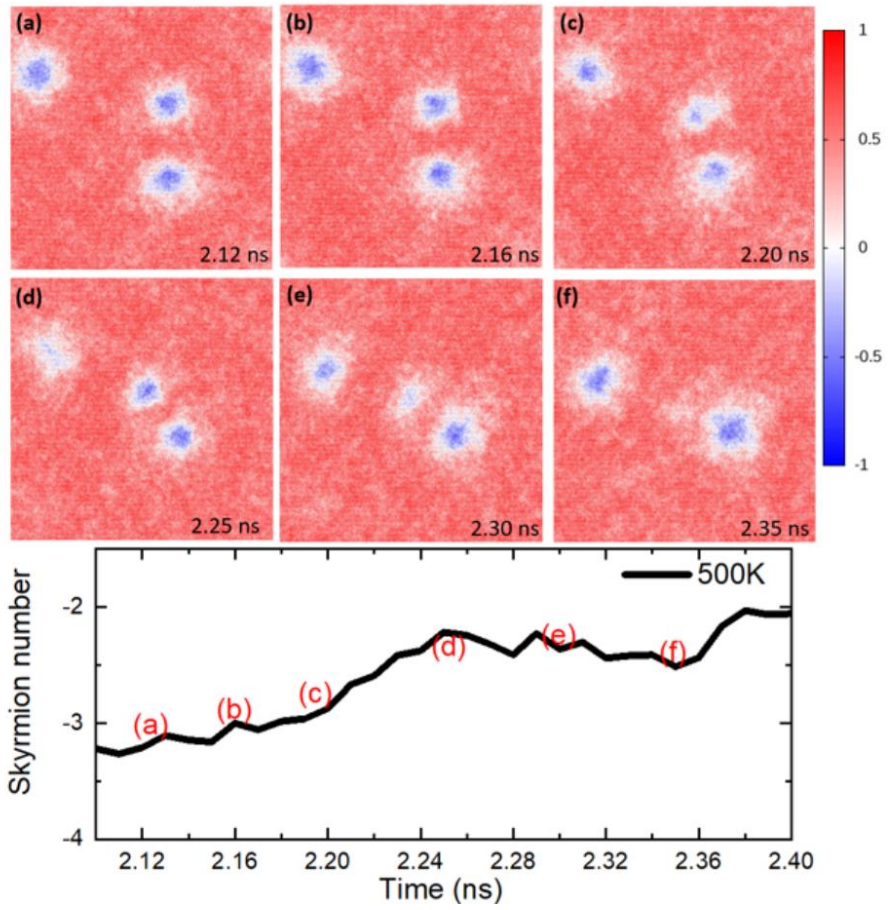

Figure 7.16 The spin configuration for skyrmion destroyed by 500 K thermal condition. The system size of the simulation is 30 nm * 30 nm * 0.25 nm with periodic boundary condition in x-direction and y-direction. The colour palette is determined by the M_z (red for +1, white for 0 and blue for -1) The result is average from 10 spin configurations in the same time range, in order to avoid the stronger thermal noise. The skyrmion number of (a) - (f) after averaged is given below the (a)-(f)

Evidence for the annihilation of a magnetic skyrmion is given in Figure 7. 16. At this stage in the time evolution of the skyrmion state, a third skyrmion has been thermally created. Under the thermal effect, magnetic skyrmions exhibit a breathing mode, with diameters increasing and decreasing due to the thermal activation. The fluctuations lead to deformation of the skyrmion which can destroy its topological protection. As evidence, from Figure 7. 16 (a) - (e), the size of one particular skyrmion begins to decrease and then the skyrmion disappears from the system. From the simulation results in Figure 7.15 - Figure 7.16, the thermal creation and annihilation of magnetic

skyrmions is clear. Furthermore, the lifetime and the number of magnetic skyrmions increases with increasing temperature. This is a statistical thermodynamic process and subject to fluctuations, but these initial results point to creation and annihilation of skyrmions at elevated temperatures.

7.5.6 Thermally induced transitions

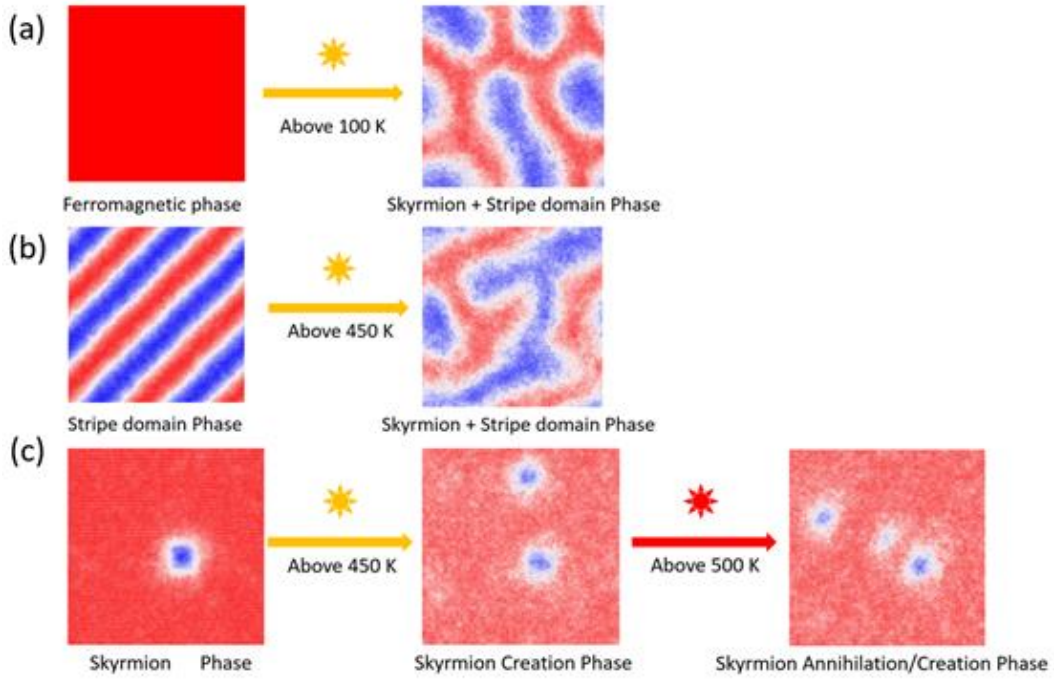

Figure 7.17 The transition between the three states in the IrCoPt system.(For the 10 ns simulation) (a) The phase between the Ferromagnetic phase and Skyrmion+Stripe domain state. (b) The transition between the Stripe and Skyrmion+Stripe domain state. (c) The transition between the Skyrmion state and Skyrmion Creation/Annihilation state.

The transition between different states in the IrCoPt system has been demonstrated by the simulation results. According to Figure 7. 17(a), for an initial ferromagnetic state, for temperatures greater than 100 K, the system transitions to stripe domains. On further temperature increase the system will transition to the Skyrmion/Stripe domain hybrid

state. In Figure 7. 17 (b), for the stripe domain state, with the temperature above 450 K, the stripe domain will be destroyed by the thermal field and change to the Skyrmion/Stripe domain hybrid phase which is similar to the case of the ferromagnetic initial state. For the skyrmion state, for temperatures greater than 450 K, there will appear thermally created skyrmions in the system. If the temperature continues to increase a beyond 500 K, the skyrmion may be destroyed by the thermal field and transition to a Skyrmion creation/annihilation state.

From the simulation results, I also found that if the temperature increase, the mean skyrmion lifetime in the system will reduce and the possibility for the thermal creation/annihilation of skyrmions will increase.

7. 6 Conclusion

In this chapter, I have studied the magnetic states of the IrCoPt system. The model is based on parameters from the ab-initio calculation and includes the full range of exchange interaction of the system. The simulation result has demonstrated transitions between different states of the system under different temperatures. When the system is in zero external field, the system will display a Skyrmion/stripe domain hybrid state at elevated temperature. For a system with an external field, the skyrmion can be thermally created/destroyed. The transitions in the chiral material system are important for the advanced skyrmion based spintronics device, for example, the skyrmions randomly generated by the thermal effect could be used to generate the random numbers in a computing device.

Chapter.8 Summary and future work

8. 1 Summary

The magnetic domain/skyrmion based devices have potential usage in future digital computing devices. The magnetic/skyrmion based devices display high performance and low power which are highly demanded by the industry. My work in this thesis is focused on the domain wall/skyrmion dynamics in nanoscale devices or thin films induced by an external field. The micromagnetic simulation and atomistic simulation methods have been used in this work. The domain wall engineering in the Permalloy junction and skyrmion/skyrmionium dynamics in narrow-track under VCMA effect are studied by the micromagnetic simulation. Skyrmion dynamics under high thermal effect is studied by the atomistic simulation.

In chapter 4, I have carried out a full micromagnetic study on the magnetisation configuration and the magnetic switching process in a nanoscale Permalloy junction. The relationship between the magnetic switching fields and the thickness of the nanoscale junction has been investigated. While different types of domain walls can be formed in the initially relaxed states depending on the specific thicknesses, the junction acts as a single CSB where the spins are aligned in parallel during the magnetisation process. The magnetisation direction can be controlled and switched coherently by applying an external magnetic field. Both the initial magnetisation field and the coercivity are found to depend on the thickness, and the large coercivity could enhance the stability of the device operation. My work shows that the nanoscale magnetic junction has the potential to be used as a building block for future spin-based data storage or logic computing technologies.

In chapter 5, the skyrmion motion in a ferromagnetic nano-track with single or multiple VCMA gates is studied. This work shows that the trajectory and location of the skyrmion can be controlled by periodically located VCMA gates as well as the driving current pulse. The unidirectional motion of the skyrmion realized by the VCMA effect can be used to build the skyrmion-based one-way information channel and the skyrmion diode. My results are useful for the design and development of the skyrmion-based spintronics devices.

In chapter 6, I investigated a magnetic skyrmionium motion in a nano-track with voltage gate and gradient. My simulation result shows that the trajectory and location of the skyrmionium can be controlled by periodically located voltage gates. The unidirectional motion of the skyrmionium realised by the VCMA effect can be used to build the skyrmion-based one-way information channel and the skyrmionium diode. In addition, I discuss the anisotropy gradient driven skyrmionium motion in a nano-track which can enhance the stability of the skyrmionium by avoiding the Joule heating. The skyrmionium can have the same velocity as the skyrmion and is free from the skyrmion Hall effect. The results are useful for design and development of the skyrmionium based logic and memory device.

In chapter 7, I have studied the phase transition in the IrCoPt system. The model is based on parameters from the ab-initio calculations and includes the full exchange interaction of the system. The simulation result has demonstrated the transitions between the magnetic states of the system under different temperatures. For a system without an external field, the system will display a skyrmion/stripe domain hybrid state at elevated temperatures. For a system subject to an external field, the skyrmion can be thermally created and destroyed. The magnetic transitions in the chiral material system are important for the advanced skyrmion based spintronics device, for example, the random skyrmions generated by the thermal effect can be used to generate the random number in the computing device.

8. 2 Future work

For further research purposes, it is suggested that the following ideas could be considered. I will continue my research after the PhD study.

Single layer STT-nano-oscillator

I will continue study the domain wall dynamics in the cross-shape device, the field free domain wall oscillating in the Permalloy junction induced by spin polarized current is a very interesting topic. The 45 degree domain wall in the cross structure in pinning by the shape of the device which discusses in chapter.4. Due to the shape anisotropy of the device, the 45 degree domain wall can be seen as a minimum energy state of the system. When there is a polarized current injected to the device, the domain wall will oscillate if the current is near the critical current. This phenomenon can be used to design the single layer nano-oscillator. Compared with other nano-oscillator, the single layer has a simple structure which is easy to fabricate and the domain structure can reduce to 45 degree when the current has stopped being injected to the device. Comparing with other domain wall oscillator the single layer domain wall oscillator has a simplier structure and high stability. The domain wall in the device will be pinned by the cross structure and easily reduce to the initial state (45 degree domain).

Skyrmion/skyrmionium dynamics induced by ultrafast laser

The topological structure skyrmion/skyrmionium can be created by temperature pulses and has already been studied. But the dynamics of magnetic chiral structure induced by ultrafast laser, is still a very interesting topic. The ultrafast laser with different fluences and laser pulse width will induce interesting phenomenon in the system. The ultrafast laser pulse can be used to generate/modulate skyrmion/skyrmion

in the device in behaviour a convenient way. But the skyrmion behaviour, under ultrafast laser influence, still needs to be studied. Also, the material defects and interface roughness will influence the skyrmion creation induced by ultrafast lasers. The mechanism of skyrmion/skyrmionium dynamics under a temperature pulse can provide useful guidelines for the future laser access skyrmion/skyrmionium based device.

Simulation of the material defect in the MRAM device structure which comes from the fabrication process.

The fabrication process of the MRAM device will induce material defects in the CoFeB MTJ. The material defect in the interface/bulk of the CoFeB MTJ will affect the magnetic properties of the device, which will generate some magnetic domain and pinning point. The modelling of the material defect in CoFeB MTJ under different thermal condition will give very important information for the designing and fabricating of the STT-MRAM device. The atomistic model can simulate the atomic scale material defect and also can calculate the critical current, Currie temperature and thermal stability of the MRAM device under different material defect condition. On the other hand, in the atomistic simulation the model can include the material defect in the interface or bulk which can be used to study how the material defect in different part of the MRAM device affected the whole system. The saturation magnetization and anisotropy in the atomistic model will be changed when the temperature increase, which makes the simulation result more accurate. The work will study the material defect effect in the interface layer of the CoFeB MTJ. The research output will help us to understand the material defect effect in the MRAM structure which is induced by the fabrication process, and improve the quality of the MRAM product. Furthermore, the result can create a guideline for designing high performance MRAM devices.

List of Abbreviations

Giant magnetoresistance	GMR
Magnetoresistive random access memory	MRAM
Tunnelling magnetic resistance	TMR
Magnetic Tunnel Junction	MTJ
Spin transfer torque magnetoresistive random access memory	STT-MRAM
Voltage-controlled magnetic anisotropy	VCMA
Perpendicular magnetic anisotropy	PMA
Dzyaloshinskii–Moriya interaction	DMI
Satuation magnetisation	M_S
Neel temperature	TN
Curie temperature	Tc
Skyrmion Hall Effect	SkHE
Object Oriented Micromagnetic Framework	OOMMF
Landau–Lifshitz–Gilbert	LLG
Density functional theory	DFT
Coherent spin block	CSB

References

[1] B. D. Cullity and C. D. Graham, *Introduction to magnetic materials*. John Wiley & Sons, 2011.

[2] S. Bhatti, R. Sbiaa, A. Hirohata, H. Ohno, S. Fukami, and S. N. Piramanayagam, "Spintronics based random access memory: a review," *Materials Today,* vol. 20, no. 9, pp. 530-548, 2017.

[3] M. N. Baibich *et al.*, "Giant magnetoresistance of (001) Fe/(001) Cr magnetic superlattices," vol. 61, no. 21, p. 2472, 1988.

[4] G. Binasch, P. Grünberg, F. Saurenbach, and W. J. P. r. B. Zinn, "Enhanced magnetoresistance in layered magnetic structures with antiferromagnetic interlayer exchange," vol. 39, no. 7, p. 4828, 1989.

[5] S. Wolf *et al.*, "Spintronics: a spin-based electronics vision for the future," vol. 294, no. 5546, pp. 1488-1495, 2001.

[6] I. Žutić, J. Fabian, and S. D. J. R. o. m. p. Sarma, "Spintronics: Fundamentals and applications," vol. 76, no. 2, p. 323, 2004.

[7] E. H. Nicollian, J. R. Brews, and E. H. Nicollian, *MOS (metal oxide semiconductor) physics and technology*. Wiley New York et al., 1982.

[8] A. H. Morrish, "The physical principles of magnetism," *The Physical Principles of Magnetism, by Allan H. Morrish, pp. 696. ISBN 0-7803-6029-X. Wiley-VCH, January 2001.,* p. 696, 2001.

[9] D. Apalkov *et al.*, "Spin-transfer torque magnetic random access memory (STT-MRAM)," *ACM Journal on Emerging Technologies in Computing Systems (JETC),* vol. 9, no. 2, p. 13, 2013.

[10] N. N. Mojumder, S. K. Gupta, S. H. Choday, D. E. Nikonov, and K. Roy, "A three-terminal dual-pillar STT-MRAM for high-performance robust memory applications," *IEEE transactions on electron devices,* vol. 58, no. 5, pp. 1508-1516, 2011.

[11] Z. Li, C. De Groot, and J. H. Moodera, "Gallium oxide as an insulating barrier for spin-dependent tunneling junctions," *Applied Physics Letters,* vol. 77, no. 22, pp. 3630-3632, 2000.

[12] J. S. Moodera, T. H. Kim, C. Tanaka, and C. H. De Groot, "Spin-polarized tunnelling, magnetoresistance and interfacial effects in ferromagnetic junctions," *Philosophical Magazine B,* vol. 80, no. 2, pp. 195-206, 2000.

[13] L. Berger, "Emission of spin waves by a magnetic multilayer traversed by a current," *Physical Review B,* vol. 54, no. 13, p. 9353, 1996.

[14] J. C. Slonczewski, "Current-driven excitation of magnetic multilayers," *Journal of Magnetism and Magnetic Materials,* vol. 159, no. 1-2, pp. L1-L7, 1996.

[15] E. Myers, D. Ralph, J. Katine, R. Louie, and R. Buhrman, "Current-induced switching of domains in magnetic multilayer devices," *Science,* vol. 285, no. 5429, pp. 867-870, 1999.

[16] J. Katine, F. Albert, R. Buhrman, E. Myers, and D. Ralph, "Current-driven magnetization reversal and spin-wave excitations in Co/Cu/Co pillars," *Physical review letters,* vol. 84, no. 14, p. 3149, 2000.

[17] R. D. McMichael and M. J. Donahue, "Head to head domain wall structures in thin magnetic strips," *IEEE Transactions on Magnetics,* vol. 33, no. 5, pp. 4167-4169, 1997.

[18] D. A. Allwood, G. Xiong, C. Faulkner, D. Atkinson, D. Petit, and R. Cowburn, "Magnetic domain-wall logic," *Science,* vol. 309, no. 5741, pp. 1688-1692, 2005.

[19] T. Ono, H. Miyajima, K. Shigeto, K. Mibu, N. Hosoito, and T. Shinjo, "Propagation of a magnetic domain wall in a submicrometer magnetic wire," *Science,* vol. 284, no. 5413, pp. 468-

470, 1999.

[20] G. Tatara and H. Kohno, "Theory of current-driven domain wall motion: Spin transfer versus momentum transfer," *Physical review letters,* vol. 92, no. 8, p. 086601, 2004.

[21] A. Yamaguchi, T. Ono, S. Nasu, K. Miyake, K. Mibu, and T. Shinjo, "Real-space observation of current-driven domain wall motion in submicron magnetic wires," *Physical review letters,* vol. 92, no. 7, p. 077205, 2004.

[22] S. S. Parkin, M. Hayashi, and L. Thomas, "Magnetic domain-wall racetrack memory," *Science,* vol. 320, no. 5873, pp. 190-194, 2008.

[23] A. Soumyanarayanan *et al.*, "Tunable room-temperature magnetic skyrmions in Ir/Fe/Co/Pt multilayers," *Nature materials,* vol. 16, no. 9, p. 898, 2017.

[24] R. Wiesendanger, "Nanoscale magnetic skyrmions in metallic films and multilayers: a new twist for spintronics," *Nature Reviews Materials,* vol. 1, no. 7, p. 16044, 2016.

[25] W. Kang, Y. Huang, X. Zhang, Y. Zhou, and W. Zhao, "Skyrmion-electronics: An overview and outlook," *Proceedings of the IEEE,* vol. 104, no. 10, pp. 2040-2061, 2016.

[26] S. Luo *et al.*, "Reconfigurable skyrmion logic gates," *Nano letters,* vol. 18, no. 2, pp. 1180-1184, 2018.

[27] X. Zhang, M. Ezawa, and Y. Zhou, "Magnetic skyrmion logic gates: conversion, duplication and merging of skyrmions," *Scientific reports,* vol. 5, p. 9400, 2015.

[28] D. Jiles, *Introduction to magnetism and magnetic materials*. CRC press, 2015.

[29] S. Chikazumi and C. D. Graham, *Physics of Ferromagnetism 2e* (no. 94). Oxford University Press on Demand, 2009.

[30] W. H. Meiklejohn and C. P. Bean, "New magnetic anisotropy," *Physical Review,* vol. 105, no. 3, p. 904, 1957.

[31] A. Fert, V. Cros, and J. Sampaio, "Skyrmions on the track," *Nature nanotechnology,* vol. 8, no. 3, p. 152, 2013.

[32] Y. Xu *et al.*, "Magnetoresistance of a domain wall at a submicron junction," *Physical Review B,* vol. 61, no. 22, p. R14901, 2000.

[33] C. Kittel, "Physical theory of ferromagnetic domains," *Reviews of modern Physics,* vol. 21, no. 4, p. 541, 1949.

[34] M. J. Donahue and D. G. Porter, "Analysis of switching in uniformly magnetized bodies," *IEEE transactions on magnetics,* vol. 38, no. 5, pp. 2468-2470, 2002.

[35] T. Ono and Y. Nakatani, "Magnetic domain wall oscillator," *Applied physics express,* vol. 1, no. 6, p. 061301, 2008.

[36] J. Wang *et al.*, "Magnetic domain wall engineering in a nanoscale permalloy junction," *Applied Physics Letters,* vol. 111, no. 7, p. 072401, 2017.

[37] A. Bogdanov and U. Rößler, "Chiral symmetry breaking in magnetic thin films and multilayers," *Physical review letters,* vol. 87, no. 3, p. 037203, 2001.

[38] U. K. Roessler, A. Bogdanov, and C. Pfleiderer, "Spontaneous skyrmion ground states in magnetic metals," *Nature,* vol. 442, no. 7104, p. 797, 2006.

[39] S. Mühlbauer *et al.*, "Skyrmion lattice in a chiral magnet," *Science,* vol. 323, no. 5916, pp. 915-919, 2009.

[40] N. Nagaosa and Y. Tokura, "Topological properties and dynamics of magnetic skyrmions," *Nature nanotechnology,* vol. 8, no. 12, p. 899, 2013.

[41] N. Romming *et al.*, "Writing and deleting single magnetic skyrmions," *Science,* vol. 341, no.

6146, pp. 636-639, 2013.

[42] T. H. R. Skyrme, "A non-linear field theory," in *Selected Papers, With Commentary, Of Tony Hilton Royle Skyrme*: World Scientific, 1994, pp. 195-206.

[43] A. Bogdanov and A. Hubert, "Thermodynamically stable magnetic vortex states in magnetic crystals," *Journal of magnetism and magnetic materials,* vol. 138, no. 3, pp. 255-269, 1994.

[44] X. Zhang *et al.*, "A decade of skyrmionics: Writing, deleting, reading and processing magnetic skyrmions roward spintronic applications," *arXiv preprint arXiv:1906.04718,* 2019.

[45] X. Yu *et al.*, "Real-space observation of a two-dimensional skyrmion crystal," *Nature,* vol. 465, no. 7300, p. 901, 2010.

[46] S. Heinze *et al.*, "Spontaneous atomic-scale magnetic skyrmion lattice in two dimensions," *Nature Physics,* vol. 7, no. 9, p. 713, 2011.

[47] N. Romming, A. Kubetzka, C. Hanneken, K. von Bergmann, and R. Wiesendanger, "Field-dependent size and shape of single magnetic skyrmions," *Physical review letters,* vol. 114, no. 17, p. 177203, 2015.

[48] S. Seki, X. Yu, S. Ishiwata, and Y. Tokura, "Observation of skyrmions in a multiferroic material," *Science,* vol. 336, no. 6078, pp. 198-201, 2012.

[49] Y. Nahas, S. Prokhorenko, L. Louis, Z. Gui, I. Kornev, and L. Bellaiche, "Discovery of stable skyrmionic state in ferroelectric nanocomposites," *Nature communications,* vol. 6, p. 8542, 2015.

[50] J. Wang *et al.*, "Controllable transport of a skyrmion in a ferromagnetic narrow channel with voltage-controlled magnetic anisotropy," *Journal of Physics D: Applied Physics,* vol. 51, no. 20, p. 205002, 2018.

[51] X. Zhang, M. Ezawa, D. Xiao, G. Zhao, Y. Liu, and Y. Zhou, "All-magnetic control of skyrmions in nanowires by a spin wave," *Nanotechnology,* vol. 26, no. 22, p. 225701, 2015.

[52] E. Hall, "On a New Action of the JIa19flet onz Electric Currents," *American Journal of Mathematics,* vol. 2, no. 3, pp. 287-292, 1879.

[53] W. Jiang *et al.*, "Direct observation of the skyrmion Hall effect," *Nature Physics,* vol. 13, no. 2, p. 162, 2017.

[54] J. Iwasaki, M. Mochizuki, and N. Nagaosa, "Universal current-velocity relation of skyrmion motion in chiral magnets," *Nature communications,* vol. 4, p. 1463, 2013.

[55] L. Kong and J. Zang, "Dynamics of an insulating skyrmion under a temperature gradient," *Physical review letters,* vol. 111, no. 6, p. 067203, 2013.

[56] S.-Z. Lin, C. Reichhardt, C. D. Batista, and A. Saxena, "Driven skyrmions and dynamical transitions in chiral magnets," *Physical review letters,* vol. 110, no. 20, p. 207202, 2013.

[57] J. Zang, M. Mostovoy, J. H. Han, and N. Nagaosa, "Dynamics of skyrmion crystals in metallic thin films," *Physical review letters,* vol. 107, no. 13, p. 136804, 2011.

[58] K. Litzius *et al.*, "Skyrmion Hall effect revealed by direct time-resolved X-ray microscopy," *Nature Physics,* vol. 13, no. 2, p. 170, 2017.

[59] I. Purnama, W. L. Gan, D. W. Wong, and W. S. Lew, "Guided current-induced skyrmion motion in 1D potential well," *Scientific reports,* vol. 5, p. 10620, 2015.

[60] G. Yin, Y. Li, L. Kong, R. K. Lake, C.-L. Chien, and J. Zang, "Topological charge analysis of ultrafast single skyrmion creation," *Physical Review B,* vol. 93, no. 17, p. 174403, 2016.

[61] B. Berg and M. Lüscher, "Definition and statistical distributions of a topological number in the lattice O (3) σ-model," *Nuclear Physics B,* vol. 190, no. 2, pp. 412-424, 1981.

[62] A. Van Oosterom and J. Strackee, "The solid angle of a plane triangle," *IEEE transactions on Biomedical Engineering,* no. 2, pp. 125-126, 1983.

[63] M. J. Donahue, "OOMMF user's guide, version 1.0," 1999.

[64] A. Vansteenkiste, J. Leliaert, M. Dvornik, M. Helsen, F. Garcia-Sanchez, and B. Van Waeyenberge, "The design and verification of MuMax3," *AIP advances,* vol. 4, no. 10, p. 107133, 2014.

[65] A. Markov, "Modeling of emerging resistive switching based memory cells," 2014.

[66] S. Zhang, P. Levy, and A. Fert, "Mechanisms of spin-polarized current-driven magnetization switching," *Physical review letters,* vol. 88, no. 23, p. 236601, 2002.

[67] M. D. Stiles and A. Zangwill, "Anatomy of spin-transfer torque," *Physical Review B,* vol. 66, no. 1, p. 014407, 2002.

[68] I. Dzyaloshinsky, "A thermodynamic theory of "weak" ferromagnetism of antiferromagnetics," *Journal of Physics and Chemistry of Solids,* vol. 4, no. 4, pp. 241-255, 1958.

[69] T. Moriya, "Anisotropic superexchange interaction and weak ferromagnetism," *Physical Review,* vol. 120, no. 1, p. 91, 1960.

[70] J. Åkerman, "Toward a universal memory," *Science,* vol. 308, no. 5721, pp. 508-510, 2005.

[71] E. Chen *et al.*, "Advances and future prospects of spin-transfer torque random access memory," *IEEE Transactions on Magnetics,* vol. 46, no. 6, pp. 1873-1878, 2010.

[72] J.-G. Zhu, "Magnetoresistive random access memory: The path to competitiveness and scalability," *Proceedings of the IEEE,* vol. 96, no. 11, pp. 1786-1798, 2008.

[73] T. Pramanik, U. Roy, L. F. Register, and S. K. Banerjee, "Proposal of a Multistate Memory Using Voltage Controlled Magnetic Anisotropy of a Cross-Shaped Ferromagnet," *IEEE Transactions on Nanotechnology,* vol. 14, no. 5, pp. 883-888, 2015.

[74] J. J. Nahas *et al.*, "A 180 Kbit embeddable MRAM memory module," *IEEE Journal of Solid-State Circuits,* vol. 43, no. 8, pp. 1826-1834, 2008.

[75] S. Tehrani, J. Slaughter, E. Chen, M. Durlam, J. Shi, and M. DeHerren, "Progress and outlook for MRAM technology," *IEEE Transactions on Magnetics,* vol. 35, no. 5, pp. 2814-2819, 1999.

[76] M. Krounbi *et al.*, "(Keynote) Status and Challenges in Spin-Transfer Torque MRAM Technology," *ECS Transactions,* vol. 69, no. 3, pp. 119-126, 2015.

[77] S. Li, A. Samad, W. Lew, Y. Xu, and J. Bland, "Magnetic domain reversal in ultrathin Co (001) films probed by giant magnetoresistance measurements," *Physical Review B,* vol. 61, no. 10, p. 6871, 2000.

[78] J. A. Currivan, Y. Jang, M. D. Mascaro, M. A. Baldo, and C. A. Ross, "Low energy magnetic domain wall logic in short, narrow, ferromagnetic wires," *IEEE Magnetics Letters,* vol. 3, pp. 3000104-3000104, 2012.

[79] S. Tehrani *et al.*, "Recent developments in magnetic tunnel junction MRAM," *IEEE Transactions on magnetics,* vol. 36, no. 5, pp. 2752-2757, 2000.

[80] A. Goncharov *et al.*, "Anisotropy of magnetization reversal and magnetoresistance in square arrays of permalloy nano-rings," *IEEE transactions on magnetics,* vol. 42, no. 10, pp. 2948-2950, 2006.

[81] W. J. Gallagher and S. S. Parkin, "Development of the magnetic tunnel junction MRAM at IBM: From first junctions to a 16-Mb MRAM demonstrator chip," *IBM Journal of Research and Development,* vol. 50, no. 1, pp. 5-23, 2006.

[82] Y. Xu *et al.*, "Domain wall trapping probed by magnetoresistance and magnetic force

microscopy in submicron ferromagnetic wire structures," *Journal of applied physics,* vol. 85, no. 8, pp. 6178-6180, 1999.

[83] G. D. Chaves-O'Flynn, G. Wolf, D. Pinna, and A. D. Kent, "Micromagnetic study of spin transfer switching with a spin polarization tilted out of the free layer plane," *Journal of Applied Physics,* vol. 117, no. 17, p. 17D705, 2015.

[84] U. Roy, H. Seinige, F. Ferdousi, J. Mantey, M. Tsoi, and S. K. Banerjee, "Spin-transfer-torque switching in spin valve structures with perpendicular, canted, and in-plane magnetic anisotropies," *Journal of Applied Physics,* vol. 111, no. 7, p. 07C913, 2012.

[85] U. Roy, T. Pramanik, M. Tsoi, L. F. Register, and S. K. Banerjee, "Micromagnetic study of spin-transfer-torque switching of a ferromagnetic cross towards multi-state spin-transfer-torque based random access memory," *Journal of Applied Physics,* vol. 113, no. 22, p. 223904, 2013.

[86] T. Pramanik, U. Roy, M. Tsoi, L. F. Register, and S. K. Banerjee, "Micromagnetic simulations of spin-wave normal modes and the spin-transfer-torque driven magnetization dynamics of a ferromagnetic cross," *Journal of Applied Physics,* vol. 115, no. 17, p. 17D123, 2014.

[87] J. Z. Sun, "Spin-current interaction with a monodomain magnetic body: A model study," *Physical Review B,* vol. 62, no. 1, p. 570, 2000.

[88] Y. Zhou, J. Åkerman, and J. Z. Sun, "Micromagnetic study of switching boundary of a spin torque nanodevice," *Applied Physics Letters,* vol. 98, no. 10, p. 102501, 2011.

[89] C. Pfleiderer *et al.*, "Skyrmion lattices in metallic and semiconducting B20 transition metal compounds," *Journal of Physics: Condensed Matter,* vol. 22, no. 16, p. 164207, 2010.

[90] W. Münzer *et al.*, "Skyrmion lattice in the doped semiconductor Fe 1− x Co x Si," *Physical Review B,* vol. 81, no. 4, p. 041203, 2010.

[91] X. Yu *et al.*, "Near room-temperature formation of a skyrmion crystal in thin-films of the helimagnet FeGe," *Nature materials,* vol. 10, no. 2, p. 106, 2011.

[92] G. Chen, A. Mascaraque, A. T. N'Diaye, and A. K. Schmid, "Room temperature skyrmion ground state stabilized through interlayer exchange coupling," *Applied Physics Letters,* vol. 106, no. 24, p. 242404, 2015.

[93] S. Do Yi, S. Onoda, N. Nagaosa, and J. H. Han, "Skyrmions and anomalous Hall effect in a Dzyaloshinskii-Moriya spiral magnet," *Physical Review B,* vol. 80, no. 5, p. 054416, 2009.

[94] X. Yu *et al.*, "Biskyrmion states and their current-driven motion in a layered manganite," *Nature communications,* vol. 5, p. 3198, 2014.

[95] H. Du *et al.*, "Highly stable skyrmion state in helimagnetic MnSi nanowires," *Nano letters,* vol. 14, no. 4, pp. 2026-2032, 2014.

[96] H. Du *et al.*, "Edge-mediated skyrmion chain and its collective dynamics in a confined geometry," *Nature communications,* vol. 6, p. 8504, 2015.

[97] W. Jiang *et al.*, "Blowing magnetic skyrmion bubbles," *Science,* vol. 349, no. 6245, pp. 283-286, 2015.

[98] W. Kang *et al.*, "Voltage controlled magnetic skyrmion motion for racetrack memory," *Scientific reports,* vol. 6, p. 23164, 2016.

[99] W. Kang *et al.*, "Complementary skyrmion racetrack memory with voltage manipulation," *IEEE Electron Device Letters,* vol. 37, no. 7, pp. 924-927, 2016.

[100] W. Kang, Y. Ran, Y. Zhang, W. Lv, and W. Zhao, "Modeling and exploration of the voltage-controlled magnetic anisotropy effect for the next-generation low-power and high-speed MRAM applications," *IEEE Transactions on Nanotechnology,* vol. 16, no. 3, pp. 387-395, 2017.

[101] S. Li, W. Kang, Y. Huang, X. Zhang, Y. Zhou, and W. Zhao, "Magnetic skyrmion-based artificial neuron device," *Nanotechnology,* vol. 28, no. 31, p. 31LT01, 2017.

[102] Y. Nii *et al.*, "Uniaxial stress control of skyrmion phase," *Nature communications,* vol. 6, p. 8539, 2015.

[103] X. Zhang, Y. Zhou, M. Ezawa, G. Zhao, and W. Zhao, "Magnetic skyrmion transistor: skyrmion motion in a voltage-gated nano-track," *Scientific reports,* vol. 5, p. 11369, 2015.

[104] X. Zhang *et al.*, "Skyrmion-skyrmion and skyrmion-edge repulsions in skyrmion-based racetrack memory," *Scientific reports,* vol. 5, p. 7643, 2015.

[105] Y. Liu *et al.*, "Chopping skyrmions from magnetic chiral domains with uniaxial stress in magnetic nanowire," *Applied Physics Letters,* vol. 111, no. 2, p. 022406, 2017.

[106] Y. Nakatani, M. Hayashi, S. Kanai, S. Fukami, and H. Ohno, "Electric field control of Skyrmions in magnetic nanodisks," *Applied Physics Letters,* vol. 108, no. 15, p. 152403, 2016.

[107] R. Tomasello, E. Martinez, R. Zivieri, L. Torres, M. Carpentieri, and G. Finocchio, "A strategy for the design of skyrmion racetrack memories," *Scientific reports,* vol. 4, p. 6784, 2014.

[108] H. Kakizakai *et al.*, "Influence of sloped electric field on magnetic-field-induced domain wall creep in a perpendicularly magnetized Co wire," *Japanese Journal of Applied Physics,* vol. 56, no. 5, p. 050305, 2017.

[109] K. Yamada, S. Murayama, and Y. Nakatani, "Magnetic domain wall motion in Co/Ni nanowires induced by a sloped electric field," *Applied Physics Letters,* vol. 108, no. 20, p. 202405, 2016.

[110] X. Wang, W. Gan, J. Martinez, F. Tan, M. Jalil, and W. Lew, "Efficient skyrmion transport mediated by a voltage controlled magnetic anisotropy gradient," *Nanoscale,* vol. 10, no. 2, pp. 733-740, 2018.

[111] J. Franken, H. Swagten, and B. Koopmans, "Shift registers based on magnetic domain wall ratchets with perpendicular anisotropy," *Nature nanotechnology,* vol. 7, no. 8, p. 499, 2012.

[112] L. Sánchez-Tejerina, Ó. Alejos, E. Martínez, and V. Raposo, "Analysis of the current-driven domain wall motion in a ratchet ferromagnetic strip," *arXiv preprint arXiv:1705.00905,* 2017.

[113] S. Woo *et al.*, "Spin-orbit torque-driven skyrmion dynamics revealed by time-resolved X-ray microscopy," *Nature communications,* vol. 8, p. 15573, 2017.

[114] Y. Zhang *et al.*, "Magnetic skyrmions without the skyrmion Hall effect in a magnetic nano-track with perpendicular anisotropy," *Nanoscale,* vol. 9, no. 29, pp. 10212-10218, 2017.

[115] M. He *et al.*, "Realization of zero-field skyrmions with high-density via electromagnetic manipulation in Pt/Co/Ta multilayers," *Applied Physics Letters,* vol. 111, no. 20, p. 202403, 2017.

[116] A. Kovács *et al.*, "Mapping the magnetization fine structure of a lattice of Bloch-type skyrmions in an FeGe thin film," *Applied Physics Letters,* vol. 111, no. 19, p. 192410, 2017.

[117] G. Yu *et al.*, "Room-temperature creation and spin–orbit torque manipulation of skyrmions in thin films with engineered asymmetry," *Nano letters,* vol. 16, no. 3, pp. 1981-1988, 2016.

[118] B. Dupé, M. Hoffmann, C. Paillard, and S. Heinze, "Tailoring magnetic skyrmions in ultra-thin transition metal films," *Nature communications,* vol. 5, p. 4030, 2014.

[119] X. Chen *et al.*, "Skyrmion dynamics in width-varying nano-tracks and implications for skyrmionic applications," *Applied Physics Letters,* vol. 111, no. 20, p. 202406, 2017.

[120] Q. Liu *et al.*, "Modulated spin orbit torque in a Pt/Co/Pt/YIG multilayer by nonequilibrium proximity effect," *Applied Physics Letters,* vol. 112, no. 2, p. 022402, 2018.

[121] J. Iwasaki, M. Mochizuki, and N. Nagaosa, "Current-induced skyrmion dynamics in constricted

geometries," *Nature nanotechnology,* vol. 8, no. 10, p. 742, 2013.

[122] A. Hrabec *et al.*, "Current-induced skyrmion generation and dynamics in symmetric bilayers," *Nature communications,* vol. 8, p. 15765, 2017.

[123] X. Zhang, Y. Zhou, and M. Ezawa, "Magnetic bilayer-skyrmions without skyrmion Hall effect," *Nature communications,* vol. 7, p. 10293, 2016.

[124] S. Komineas and N. Papanicolaou, "Skyrmion dynamics in chiral ferromagnets under spin-transfer torque," *Physical Review B,* vol. 92, no. 17, p. 174405, 2015.

[125] X. Zhang *et al.*, "Control and manipulation of a magnetic skyrmionium in nanostructures," *Physical Review B,* vol. 94, no. 9, p. 094420, 2016.

[126] M. Finazzi *et al.*, "Laser-induced magnetic nanostructures with tunable topological properties," *Physical review letters,* vol. 110, no. 17, p. 177205, 2013.

[127] S. Li *et al.*, "Dynamics of a magnetic skyrmionium driven by spin waves," *Applied Physics Letters,* vol. 112, no. 14, p. 142404, 2018.

[128] M. Shen, Y. Zhang, J. Ou-Yang, X. Yang, and L. You, "Motion of a skyrmionium driven by spin wave," *Applied Physics Letters,* vol. 112, no. 6, p. 062403, 2018.

[129] R. Loreto *et al.*, "Creation, transport and detection of imprinted magnetic solitons stabilized by spin-polarized current," *Journal of Magnetism and Magnetic Materials,* vol. 455, pp. 25-31, 2018.

[130] H. Xia, C. Song, C. Jin, J. Wang, J. Wang, and Q. Liu, "Skyrmion motion driven by the gradient of voltage-controlled magnetic anisotropy," *Journal of Magnetism and Magnetic Materials,* vol. 458, pp. 57-61, 2018.

[131] Y. Liu *et al.*, "Voltage-driven high-speed skyrmion motion in a skyrmion-shift device," *Physical Review Applied,* vol. 11, no. 1, p. 014004, 2019.

[132] S. Rohart and A. Thiaville, "Skyrmion confinement in ultrathin film nanostructures in the presence of Dzyaloshinskii-Moriya interaction," *Physical Review B,* vol. 88, no. 18, p. 184422, 2013.

[133] W. Koshibae and N. Nagaosa, "Creation of skyrmions and antiskyrmions by local heating," *Nature communications,* vol. 5, p. 5148, 2014.

[134] G. Berruto *et al.*, "Laser-induced skyrmion writing and erasing in an ultrafast cryo-lorentz transmission electron microscope," *Physical review letters,* vol. 120, no. 11, p. 117201, 2018.

[135] W. F. Brown Jr, "Thermal fluctuations of a single-domain particle," *Physical Review,* vol. 130, no. 5, p. 1677, 1963.

[136] A. Lyberatos, D. V. Berkov, and R. W. Chantrell, "A method for the numerical simulation of the thermal magnetization fluctuations in micromagnetics," *Journal of Physics: Condensed Matter,* vol. 5, no. 47, p. 8911, 1993.

[137] O. Chubykalo, R. Smirnov-Rueda, J. Gonzalez, M. Wongsam, R. W. Chantrell, and U. Nowak, "Brownian dynamics approach to interacting magnetic moments," *Journal of magnetism and magnetic materials,* vol. 266, no. 1-2, pp. 28-35, 2003.

[138] S.-G. Je *et al.*, "Creation of magnetic Skyrmion bubble lattices by ultrafast laser in ultrathin films," *Nano letters,* vol. 18, no. 11, pp. 7362-7371, 2018.

[139] R. Tomasello *et al.*, "Origin of temperature and field dependence of magnetic skyrmion size in ultrathin nanodots," *Physical Review B,* vol. 97, no. 6, p. 060402, 2018.